2018

Behavior of reinforced concrete walls with circular openings

Yinglong Zhang
Iowa State University

Recommended Citation

Zhang, Yinglong, "Behavior of reinforced concrete walls with circular openings" (2018). *Graduate Theses and Dissertations*. 16702.
https://lib.dr.iastate.edu/etd/16702

Behavior of reinforced concrete walls with circular openings

by

Yinglong Zhang

A thesis submitted to the graduate faculty

in partial fulfillment of the requirements for the degree of

MASTER OF SCIENCE

Major: Civil Engineering (Structural Engineering)

Program of Study Committee:
An Chen, Major Professor
Simon Laflamme
Kejin Wang

Iowa State University

Ames, Iowa

2018

TABLE OF CONTENTS

Page

LIST OF FIGURES

LIST OF TABLES

ACKNOWLEDGMENTS

The completion of this thesis would not have been possible without the help and guidance of my advisor, professors, lab instructors, and fellow graduate students with whom I have worked with over the past two years.

First, I would like to thank Dr. An Chen for giving me the opportunity to conduct this study by providing me with all the required support and guidance to achieve my goals. I would also like to express my appreciation for his motivation and encouragement throughout other aspects of my life.

I would like to thank Dr. Simon Laflamme and Dr. Kejin Wang for serving on my POS committee. Their guidance and support throughout the course of this research are valuable for my graduate study.

I would like to extend my gratitude to Douglas Wood, Owen Steffens and Zhao Cheng for their guidance and help in developing the experimental plan.

I would also like to thank Hao Wu and David Morandeira for their help in developing the finite element models and other aspects of this research.

In addition, I would also like to thank my friends and colleagues: Elizabeth Miller, Connor Schaeffer, Ahmed Alateeq, Mohammed Bazroun, Jin Yan, Mostafa Yossef, Rizwan Karim, Satish Jain and many more.

Furthermore, I want to thank my family. Special thanks to my parents for believing in me, supporting me to study in the United States, and encouraging me to be a better person.

Finally, I want to thank the National Science Foundation agency. This material is based in part upon work supported by the National Science Foundation under Grant No.

CMMI-1562992. Any opinions, findings, and conclusions or recommendations expressed in this material are those of the authors and do not necessarily reflect the views of the National Science Foundation.

ABSTRACT

Reinforced concrete wall is one of the major components in a building system. It is subjected to different types of loads, such as gravity, wind, seismic load, etc. This thesis is part of a research project on water-filled reinforced concrete wall panels for energy efficiency and multi-hazards mitigation. The concept of this wall panel is that it contains various openings allowing water to circulate. Hot and cold water can be used in winter and summer, respectively, to achieve energy efficiency. More importantly, water in the openings can form a multi-column Tuned Liquid Wall Damper (TLWD) system, which provide a damping effect to mitigate multi-hazards. However, the openings inside the wall panel will reduce its strength. Therefore, there is a need to study the effect of the openings on the performance of the wall panels, which is the objective of thesis. In this thesis, a multi-objective method, which considers the strengths and damping effect of the wall panel, is used to optimize the TLWD system with respect to the number and sizes of the opening. Next, four-point bending tests on wall panels corresponding to the optimized configuration is conducted. A Finite Element (FE) model is then developed to study the panels under the bending load, and correlated with testing results. The FE model is further used to conduct a parametric study with different openings on the performance of wall panels under out-of-plane bending, axial loading and push-over conditions. The effect of different parameters are discussed. Finally, ACI design equations are used to calculate the strengths of the wall panels. Based on comparisons with the results from the FE parametric study, recommendations are provided on how to improve the design methods of the wall panels with openings.

CHAPTER 1. INTRODUCTION

1.1 Background

Reinforced concrete wall is a common structural element used in building systems. With the rapid growth in the number of slender high-rise buildings over the past few decades, their wind vibration and seismic risk have attracted researchers' attention. Many damping devices have been installed inside tall buildings to mitigate these effects. Recently, the idea of a new liquid damper device called Tuned Liquid Wall Damper (TLWD) has been proposed. This special damper consists of multiple columns connected at the bottom of the wall, and has a high efficiency in reducing vibration throughout the wall (Wu et al. 2017). This thesis aims to study the effect on the strength reduction due to different configurations of circular openings to fit TLWDs in. Listed below is an introduction to several topics explored with this research.

1.1.1 High Rise Building

The number of high-rise buildings has been increasing around the world. They can be used to display wealth and power, religious beliefs, traditions, and have pushed the boundaries of engineering (Rist and Svensson 2016). There are many advantages of high-rise buildings, such as more effective use of land area and closer relationship among people in specialized communities for more efficient intercommunication (Reese and Picardi 1968). However, there are many structural issues associated with high-rise buildings. High-strength steel, lighter cladding, and modern construction techniques have allowed tall buildings that have lower natural frequencies (Steffen 2016). When subjected to dynamic loads such as wind and earthquake events, buildings with low structural damping values are susceptible to vibration due to their slenderness, and could cause disturbance to the occupants (Kwok et al. 2009).

Additionally, high-rise buildings will have more lateral displacement in the presence of wind or earthquake loads, which can lead to higher induced moments and shear forces. Due to these effects, the safety of tall building structures and the comfort of the occupants under dynamic loads remains a significant engineering concern (Chai and Feng 1997).

In order to suppress the structural response of tall buildings, an effective damper is necessary to be used within the building, one option being inside the walls. Recently, a new idea of a multi-column Tuned Liquid Wall Damper (TLWD) system has been proposed by Wu et al. (2017). The TLWD consists of multiple vertical columns containing liquid, and has proven to be effective in providing damping functionality. Typically, the number and size of vertical liquid columns of a TLWD system can be adjusted dependent on building type and designer expectations. TLWDs can be built inside reinforced concrete walls, the columns placed before casting of concrete (Wu et al., 2017). While the vertical columns can assist in damping, they will also be associated with a reduction in strength in the reinforced concrete wall, due to the “hole” from the vertical column. This research aims to explore the strengths associated with reinforced concrete containing different circular opening cases. A design method for walls with circular openings will also be developed.

1.1.2 Reinforced Concrete Walls

Reinforced concrete walls are important components of buildings’ structural systems, because they behave as an efficient bracing system, and providing lateral load resistance and drift control. Concrete is the material that strong in compression and weak in tension; therefore, cracks easily develop once the tensile stress exceeds the tensile strength of the concrete. Reinforced steel bars, which have similar thermal expansion properties as concrete but have high tensile strength and ductility, are bonded to concrete to provide sufficient strengths for design. With these two components, reinforced concrete systems maintain equilibrium, even after concrete cracks from tensile forces (Lefas et al. 1990; Wight 2016).

Among different types of reinforced concrete walls, bearing wall and shear walls are the two most common categories that are used in buildings. Bearing walls primarily resist vertical gravity loads acting on top of the wall, while shear walls are designed for resisting lateral loads, such as wind and earthquake loads. The figures of these two types of walls are shown in Figures 1-1(a) and (b), respectively. Reinforced concrete load bearing walls are being increasingly used in building systems, and is typically design for resisting axial loads. The height-to-thickness ratio is one of the most fact in investigating the strength of bearing walls as the buckling failures will likely to occur for slender walls (Pillai and Parthasarathy 1977; Wight 2016). In addition, shear walls are commonly used in some earthquake-prone countries as lateral-load resisting systems, and their performance in resisting seismic forces has found to be successful. On the other hand, the ductility and the deformation capacity of shear walls can be significantly impacted by the axial load ratio and the wall configurations. Typically, a large deformation can cause a shear wall suffers from tension cracks developing in tension areas while crushing occurring in the localized compression zones, therefore, the capacity of shear walls need to be sufficiently designed (Athanasopoulou 2010; Hidalgo et al. 2002; Zhang et al. 2016).

Despite these excellence performance of shear walls and bearing walls in building structures, for many reasons, the walls need to have openings such as to adapt to comply with current living standards and to install different types of devices inside. Previous experimental investigations have shown that the existence of openings in the reinforcement walls, especially for large openings, will affect its ultimate load capacity, cause disturbance in the load paths, and creates stress concentration around the openings. Therefore, it is essential to investigate the strength reduction of the wall with openings and to upgrade the wall accordingly. (Demeter et al. 2012; Popescu 2015; Mohammed et al. 2013)

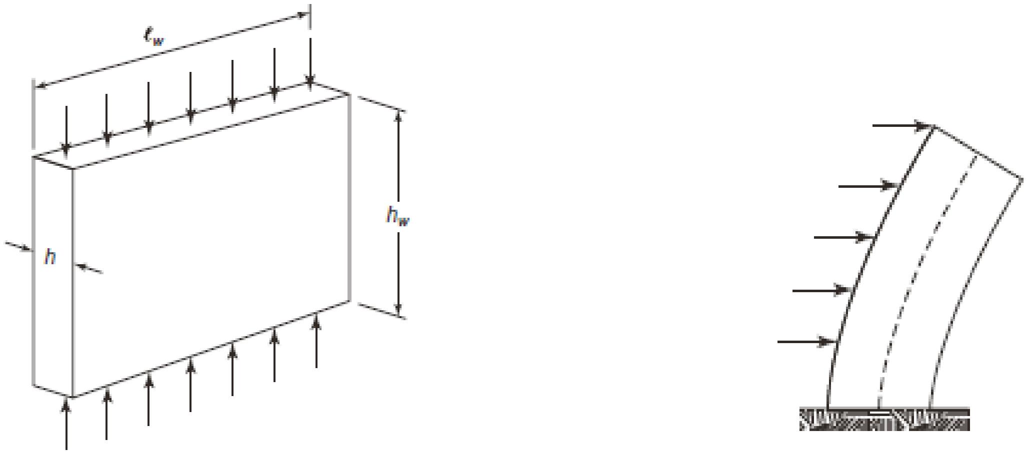

(a) (b)

Figure 1-1. (a) Bearing wall; (b) Shear wall (Wight 2016)

1.1.3 Multi-objective Optimization

Conducting a multi-objective optimization is appropriate when a decision needs to be made that involves more than one objective that need to be optimized at the same time. A single objective optimization is less complicated than a multi-objective one, as it only requires an optimal solution from a sole objective function. However, in the real world, optimization problems often need to take multiple conflicting objectives into account; therefore, considering two or more optimization objectives simultaneously is essential for obtaining more reasonable results. Because of the lack of suitable solution techniques for multi-objective optimization, the primary focus of such optimization problems is to categorize different objectives into one single objective, or in other words, to convert from local tasks to one global task (Chankong and Haimes 1983; Caramia and Dell'Olmo 2008; Burke and Kendal 2014).

Burke and Kendal give an example that can be used to demonstrate the difference between a single objective and multi-objective decision-making problem (Burke and Kendal 2014; Davalos and Qiao 1996). The example explains that when buying the car, if the price is the only objective in making a decision, the optimal choice would be buying the cheapest car, an easy and intuitive decision. This decision would be identified as having a single objective. However, if a car with higher price will have a better performance, then another objective is considered in this decision-making problem, making the decision multi-objective. Rather than doing two independent single-objective optimization problems, there exist many solutions with different car prices and performances between the two objectives of price and performance. An example of the interaction of these two objectives can be shown in Figure 1-2. As shown in the graph, a better choice in terms of one objective may come from the sacrifice of the other objective. Therefore, one would need to consider the trade-off between price and performance of the car, taking both objectives into account to find the best solution from a wide range of choices. (Burke and Kendal 2014; Davalos and Qiao 1996).

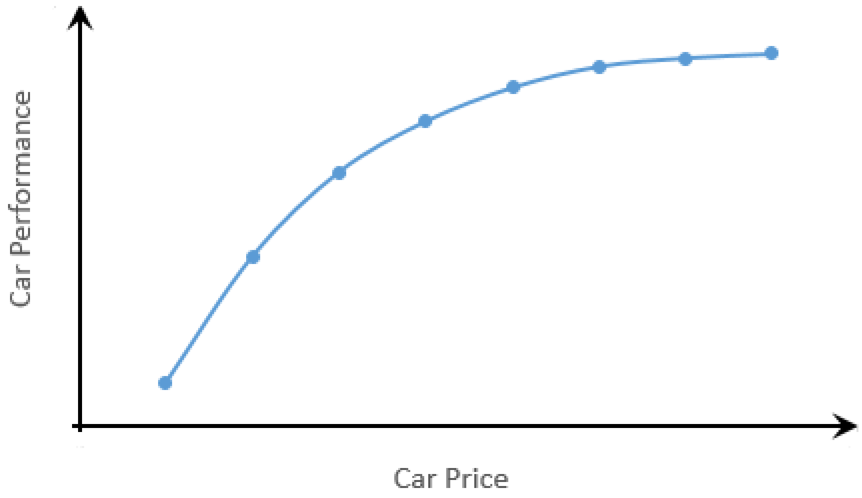

Figure 1-2. Multiple Solutions for a Car-buying Decision-making Problem with Two Objectives

Multi-objective optimization methods have a tremendous practical importance since they suite most real-life decision-making problems. This thesis illustrates and presents a multi-objective optimization technique for the optimum design of a multi-column TLWD system with respect to the TLWD's column size and number. The two main objectives of the system are strength and damping effectiveness. The TLWD will be installed inside a wall with specified set dimension, so the strength of the wall is dependent on the configurations of TLWDs. The wall will be subjected to both lateral and axial loads, so moment of inertia, shear capacity, moment capacity, and bearing capacity are the parameters that will categorize the strength of the wall. The damping effectiveness of the wall will be determined by the column size and number; as these increase, the damping of the system will also increase. However, as the column size increases and more columns are added to increase the efficiency of the TLWD, the volume of empty space in the wall will be larger, and the strength of the wall will decrease simultaneously. These two optimization objectives are conflict with each other, therefore, the multi-objective optimization is necessary to be applied. This thesis aims to obtain the optimal solution among different possible combinations of column sizes and number.

1.1.4 Finite Element Model of Reinforced Concrete Members

The understanding of structural behaviors has improved a lot over the last quarter century, however, the accuracy of theory-based analysis still has much room for improvement. In the modern world, not only safety issues, but also energy and material saving related problems are the important aspects to be considered in engineering design. In order to obtain more accurate results to meet these goals, finite element modeling has been widely used, especially in reinforced concrete structure analysis, when nonlinear behavior needs to be taken into account. Finite element analyses on reinforced concrete members can show the developing process of structure deformation, and identify where cracks will grow, and where members will fail (Tyau 2009; Friswell and Mottershead 1996; Zhang et al. 1994; Zhang and Yang 2007).

In this study, a finite element model was developed using the commercial software ABAQUS, which lets the user create a numerical model and submit it to different loading conditions. The progress of the analyses can be monitored, and the results of the analyses can be viewed in a post-processing mode (Gebreyohaness et al. 2012). One of the most significant advantages of using finite element modeling in predicting the nonlinear behavior of concrete under loading is using the concrete damage plasticity (CDP) model, which is based on a crack model that uses fracture energy for describing the stress-strain relation in reinforced concrete. The CDP model defines the behavior of concrete under multiple loading conditions based on defined uni-axial properties and other material behaviors such as dilation angle, eccentricity, ratio of biaxial strength to uniaxial strength and so on (Tyau 2009; Genikomsou 2016;

Gebreyohaness et al. 2012). The CDP model has been developed and modified by many researchers to generate different stress-strain relationships of reinforced concrete. In this study, two different models are utilized. Hognestad's model is used for concrete compressive modeling and Wahalathantri et al.'s model is used for concrete tensile modeling. Details in getting the yield stress and plastic strain relation are presented in chapter 4.2.2.2. Utilizing the nonlinear finite element analysis for reinforced concrete structures, the possible failure modes, and structural strengths can be estimated when physical test measurements are not known, or cannot be carried out (Genikomsou et al. 2016).

1.2 Problem Statement

TLWD systems are effective systems to mitigate the vibration of building structures, and can be installed inside of reinforced concrete walls. The TLWD inside of reinforced concrete walls is composed of multiple liquid-filled vertical tubes. However, reinforced concrete walls with circular openings will result in strength reduction as compared to solid ones, affecting their performance. With different sizes and numbers of tubes as options in TLWD systems, walls could have different opening configurations, resulting in varied strengths. It is important to investigate the strength of the walls with different opening configurations so designers can choose between different objectives (strength of wall vs. damping effect) when designing TLWD reinforced concrete walls. By knowing the behavior of the wall with openings, the engineers can design the other components of the building structure properly.

1.3 Thesis Organization

The thesis is organized as follows. Chapter 2 presents the hand calculation approach to obtain wall strengths, and then use these hand-calculated results as the criteria to do a multi-objective optimization to find the optimal solution of TLWD system with respect to column number and size. Chapter 3 describes the experimental investigations to find the load and moment capacities of the wall with circular openings, corresponding to the optimal TLWD case found in the previous chapter. Chapter 4 presents the finite element models of the wall with circular openings with respect to optimized TLWD configuration under different loading conditions to find the corresponding strengths of the wall. This chapter also contains a parametric study on column number and size, included to further verify hand calculation results and to compare with the lab testing results. Chapter 5 compares of the strengths of the reinforced concrete wall with and without circular openings. This chapter also summarizes the design method of a reinforced concrete wall with circular openings based on an improved method provided by ACI 318-14 Building Code and proposes suggestions on how to design this type of wall to meet basic strength requirements. Chapter 6 presents conclusions and future work.

CHAPTER 2. MULTI-OBJECTIVE OPTIMIZATION

2.1 Introduction

Tuned Liquid Column Damper (TLCD) was introduced more than twenty years ago. It has many advantages when compared to a traditional mass damper, such as lower cost, easier installation and few maintenance requirements (Wu and Hsieh 2002). As of today, TLCDs have been installed in many buildings. However, the strength capacity of TLCDs is limited since the system traditionally only has two columns, and requires a large space in order to effectively dissipate energy. Therefore, a new liquid damping system, called Tuned Liquid Wall Damper (TLWD), was proposed. TLWD is composed of a series of vertical columns connected at the bottom (Wu et al. 2017). The configurations of TLCD and TLWD are shown in Figure 2-1, with the orifices are located on the bottom tubes between two vertical tubes. Optimization is essential when designing a TLWD, since different combinations of liquid column sizes and number have to be considered. In optimizing the TLWD system, a multi-objective method can been carried out (Davalos and Qiao, 1996). Wall strength and damping effect are two objectives to be considered in the optimization.

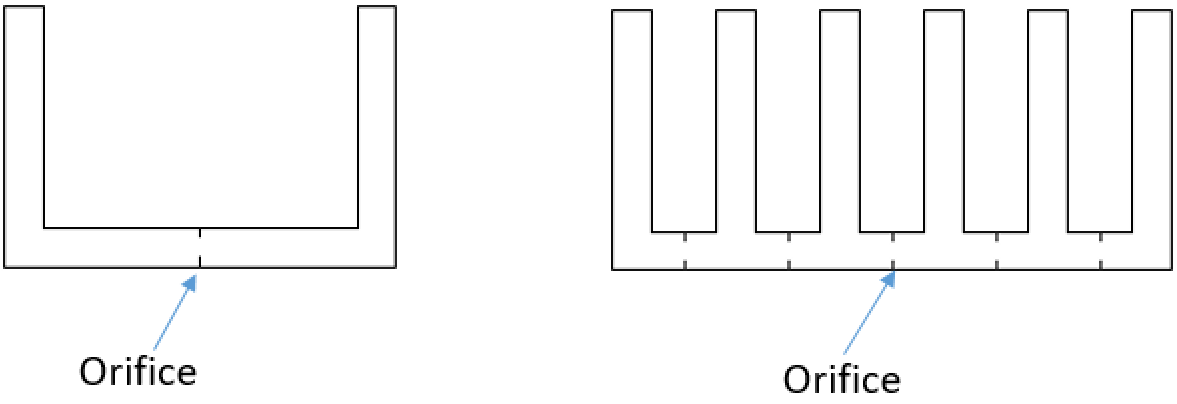

(a) (b)

Figure 2-1. (a). Configuration of the TLCD System; (b). Configuration of the TLWD System

The optimization of the TLWD system can achieve the balance of improving the damping effect of the system, while still not compromising the strength of the reinforced concrete wall. The overall optimization process can be summarized as the use of global criterion to minimize the multiple objective functions. In particular, the first step is to set up the bounds (minima and maxima) for column sizes and number. Once all data are obtained for each objective corresponding to different combinations of column sizes and number, the ideal solutions, i.e., the extreme values for each objective, will be selected. Next, the sum of the squares of the relative deviation of the criteria from ideal solution of each objective is calculated, and the smallest value obtained from the optimization function indicates the optimal design.

In this chapter, the detailed calculation process of optimization is presented, followed by the application of a multi-objective method to obtain the optimal solution. The lab testing and numerical simulation using ABAQUS will be conducted to validate these hand calculations, and is presented in the following two chapters.

2.2 Configurations of Specimen

Based on the project proposal, a 5’ high, 2’ wide and 4” thick reinforced concrete wall is designed. Due to the thickness of the wall, No. 2 bars are used to provide wider range of the PVC pipe sizes that we can choose. Based on the analysis of a 1-foot stripe wall, for the design of the transverse reinforcement, the equation is given as:

$$A_s = \rho_t * b * h \tag{1}$$

where ρ_t is the minimum transverse reinforcement ratio and taken as 0.0025, b is a 1ft strip and h is the thickness of the wall. According to the minimum reinforcement area needed per foot, eight 2-layer No.2 reinforcements are selected for transverse reinforcement, giving a reinforcement ratio of 0.295%.

For the design of the longitudinal reinforcement, the equation is given as:

$$A_s = \rho_l * b * h \tag{2}$$

where ρ_l is the minimum longitudinal ratio and is also 0.0025. Using the same b and h value, four 2-layer No.2 reinforcements are selected for longitudinal reinforcement, giving a reinforcement ratio of 0.331%. The layout of wall reinforcements is shown in Figure 2-2.

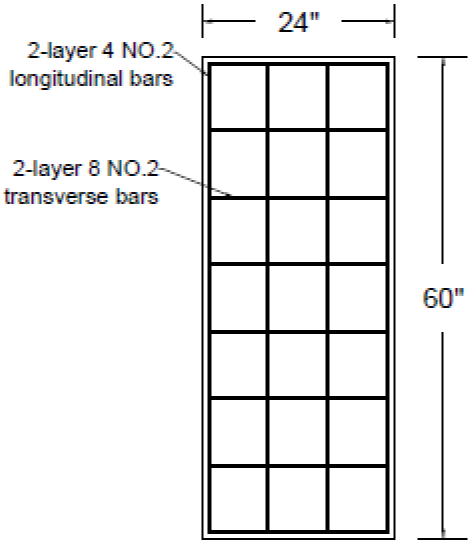

Figure 2-2. Layout of Wall Reinforcements

PVC tubes will be installed inside the wall to create the TLWD. Four parameters related to the strength of the wall (moment of inertia, shear strength, flexural strength, and bearing strength) need to be calculated corresponding to different tube sizes and number. According to ACI 318-14 Building Code, the recommended concrete cover for a cast-in-place non-prestressed concrete wall member with No.11 bars and smaller is ¾ inch, however, due to the small size of the wall specimen the limited space and the size of the plastic supports that under the reinforcements, the concrete cover has been reduced to 0.425 inch along the wall thickness direction, and small aggregate size concrete is used instead to fulfill this requirement. The concrete cover along the length and height directions of the wall are still ¾ inch (Figure 2-3).

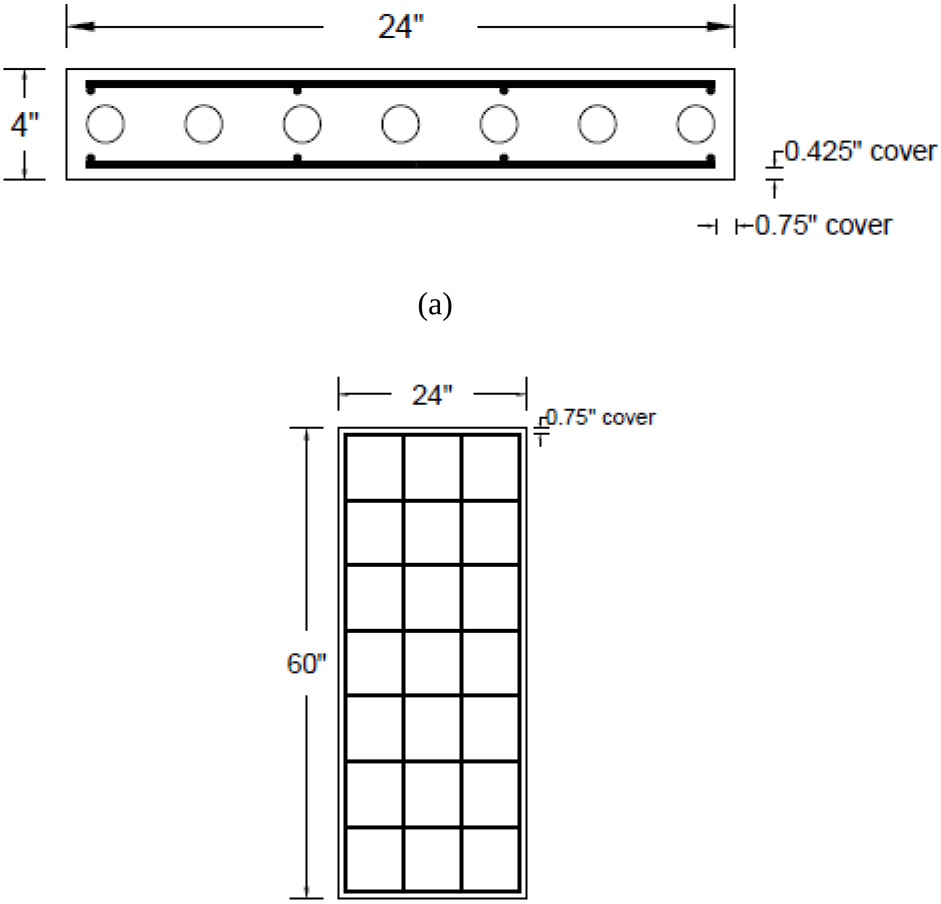

(a)

(b)

Figure 2-3. (a). Top View of the Wall with Concrete Covers; (b). Front View of the Wall with Concrete Cover

In order to optimize the TLWD system within a target range, the upper and lower bounds of column sizes are determined. In this study, the lower bound of column size follows the typical size of capillary tubes used in temperature control systems, which is about 15 to 20 mm. (0.6 – 0.8 in.) (Pfafferott and Kalz 2007). The upper bound of column size is the maximum one that can fit into the wall while still providing enough space between the pipes and wall reinforcement. Based on the available PVC pipe sizes on the market, the upper bound of the dimension of the tube is designed as 1.66” outside diameter and the lower bound of the dimension is designed as 0.84” outsider diameter. The minimum distance between the two edges of pipes is designed as ¾ inch. Based on these provisions, the number of tubes used in the TLWD can be 2 to 9 tubes or 2 to 14 with these two diameter dimensions respectively (Figure 2-4 (a) through (d)).

Since PVC pipes have distinct thickness, the outside diameter represents the actual designed sizes of tubes and the inside diameter determines how much water each tube can contain. The nominal sizes are used for identification purposes. PVC pipes with different thicknesses were divided into different categories, and these categories were named with schedule numbers. A smaller schedule number means a thinner wall thickness. Schedule 80 and 40 pipes are the most common types of PVC pipes. Schedule 30 pipes are considered as thin-wall pipes. In this study, the schedule 30 pipe is selected to compose the TLWD system, as it will have a higher water capacity as compared to pipes with the same outer diameters but greater wall thicknesses. Table 2-1 summaries the available schedule 30 tube sizes on the market, and the corresponding minimum and maximum number of pipes that can fit into the reinforced concrete wall.

Table 2-1. Available Sizes, and the Min. and Max. Allowable PVC Tubes

Nom. Size (in.)	*O.D. (in.)*	*I.D. (in.)*	*Min Num.*	*Spacing (in.)*	*Max Num.*	*Spacing (in.)*
0.5	0.84	0.71	2	21.66	14	1.666
0.75	1.05	0.92	2	21.45	12	1.95
1	1.315	1.185	2	21.185	11	2.119
1.25	1.66	1.53	2	20.84	9	2.605

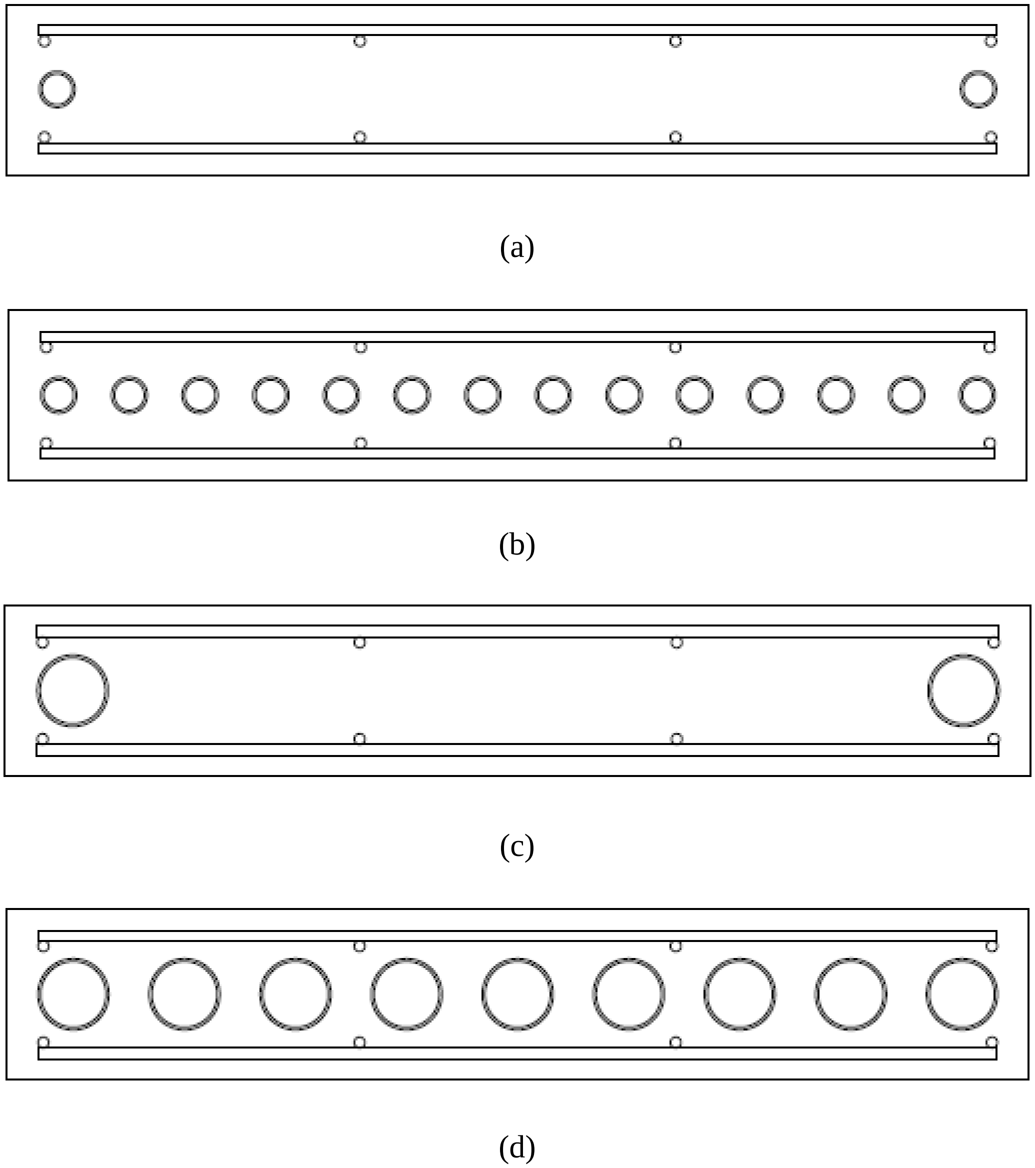

(a)

(b)

(c)

(d)

Figure 2-4. (a). Lower Bound of Dimension of Tube with Minimum Amount; (b). Lower Bound of Dimension of Tube with Maximum Amount; (c). Upper Bound of Dimension of Tube with Minimum Amount; (d). Upper Bound of Dimension of Tube with Maximum Amount

2.3 Objectives in Optimization

2.3.1 Strength of Wall

As mentioned above, four parameters are considered in calculating the strength of the wall. The first is moment of inertia, which is a geometry based parameter. The more holes and larger holes in a wall, the smaller its moment of inertia. Besides of the strength capacity of a wall, the moment of inertia of a wall is also an important to investigate because it represents the stiffness of the wall, and the reduction of the stiffness of a wall may further impact the strength capacity of a wall that caused by openings. The calculation of moment of inertia of the wall in vertical direction (y direction) with different combinations of pipes is based on the following equation:

$$I_y = \frac{1}{12}bh^3 - \sum_{i=1}^{n} A\overline{y_i}^2 - n\frac{1}{4}\pi r^4 \tag{3}$$

where b and h are width and thickness of the wall, A is the area of each hole, $\bar{y}$ are the distances from center of each hole to the neutral axis, n is the number of holes, and r is the radius of each hole. In horizontal direction (x direction), the center points of the holes fall on the neutral axis, therefore, the second term in equation three does not have to be considered. The calculated results are values of moment of inertia with respect to different tube arrangements.

The second strength parameter is shear strength. In the optimization process, only in-plane shear is considered since this is the dominant direction of shear force. The nominal shear strength of a regular reinforced concrete wall consists of two parts: shear strength from concrete, V_c, and shear strength from reinforcing, V_s. The equation for calculating V_c is:

$$V_c = 2\sqrt{f'_c}\,b_w d \tag{4}$$

where $f'c$ is the compressive strength of concrete, b_w is the thickness of the wall, d is the effective depth, which equals to the distance from the extreme compression fiber to the center of the reinforcements in tension. The equation for calculating V_s is:

$$V_s = \frac{A_v f_{yt} d}{S} \tag{5}$$

where A_v is cross-section area of transverse reinforcement, f_{yt} is specified yield strength of transverse reinforcement, and S is the spacing of transverse bars. Then shear strength of the wall, V_n, can be calculated as the sum of V_c and V_s. In these equations, f'_c is 4 ksi for normal weight concrete, and f_{yt} is 60 ksi. Two rows of No.2 transverse reinforcements give 0.1 in^2 of shear reinforcement area. Plugging all these numbers into the equation above, V_n can be obtained for a solid wall. When holes exist on the wall, V_s will not be affected because shear reinforcements remain unchanged. However, V_c will decrease due to the change of the surface area that can resist shear force. For the wall, inclined cracks exist before a shear failure can occur. If there are holes on top surface of the wall, the crack will traverse throughout the holes, and the area of the top surface of the wall within the effective depth part will decrease. Therefore, the shear capacity of the wall under in-plane shear force will be reduced accordingly, with proportional to the area reduction from the openings within the effective depth region. The approach to calculate the shear strength of the wall with holes is given as:

$$V_n = 2\sqrt{f'_c}(b_w d - A') \tag{6}$$

where A' is the area of the openings within the effective depth region on top surface of the wall. With this equation, the nominal shear strength of the wall with holes can be calculated accordingly. Based on the ACI 318-14 Building Code, a shear strength-reduction factor Φ of 0.75 need to be included, and the design shear capacity being ΦV_n.

The third strength parameter considered is the moment strength. According to ACI 318-14 Building Code for reinforced concrete structures, the Whitney Stress Block can be utilized for calculating the nominal moment strength of solid walls. In this study, the strong axis moment capacity of the wall, where the wall is being loaded on the thickness side and bend along the direction of its length, will be considered as the objective to optimize the TLWD system. The wall section was chosen to be double reinforced, so the following equation is used to calculate the nominal moment strength:

$$M_n = C_C\left(d - \frac{a}{2}\right) + C_S(d - d') \tag{7}$$

where d is the typical effective depth, which is the distance from the centroid of the reinforcement to the extreme compression fiber, a is the depth of the compression block, C_s is force in compression reinforcement, and d' is the distance from the compression edge to the centroid of the compression reinforcement. C_c is concrete compression force and can be calculated from $0.85f'_c b\beta_1 c$, where b is the width of the wall, and β_1 is 0.85 for 4 ksi concrete. The design moment capacity of the wall is equivalent to the above calculated M_n multiplied by a moment strength-reduction factor Φ of 0.9.

When there are holes in a wall, the moment capacity will decrease. According to Mansur and Tan, the existence of the openings will not affect the load-carrying mechanism of the concrete wall as long as the openings remain within the tension zone because the concrete will crack anyway under tensile stress (Mansur and Tan 1999). The tensile stress will then be taken by reinforcements after concrete cracks. Therefore, it can be concluded that the moment capacity will not decrease dramatically because the depth of the compressive stress block, a, when calculated, is only 1.12” in the wall section (Figure 2-5), which is small when compared to the total width of the wall. Thus, when holes exist inside the compressive stress block, the area of the block will decrease, it is assumed that the depth of compression chord will increase in order to keep the area of compressive stress block to be the same as original, which is 1.12 × 4 = 4.48 in^2. With the increase of a, the moment arms of the forces from both tensile and compressive reinforcements will become smaller, therefore, M_n will decrease and so does the flexural strength of the wall. On the other hand, based on the previous calculations, the moment of inertia of the wall will decrease due to the holes on the wall, and thus the cracks will initiate at an earlier stage of loading (Mansur 2006), this does not necessary mean the decrease of the moment capacity of the wall if the holes are inside tension zone.

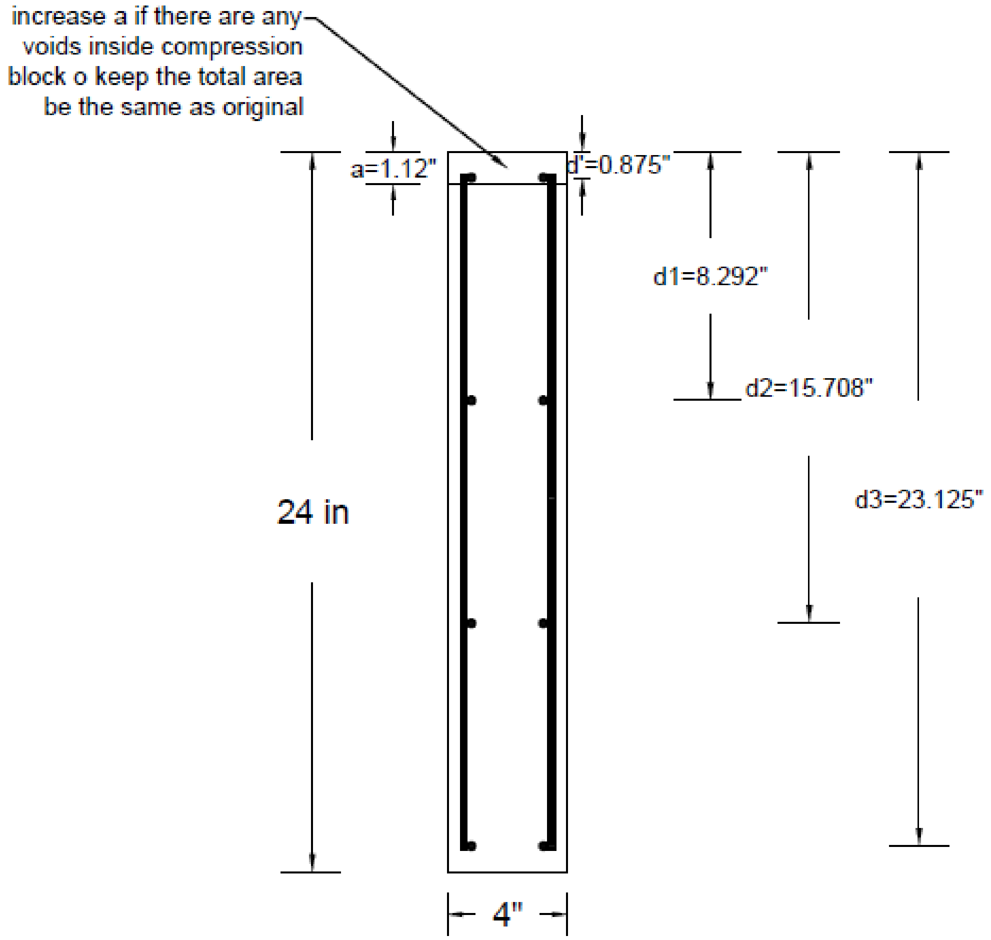

Figure 2-5. Top View of the Wall and the Compression Block in Vertical Direction

On the other hand, the weak axis moment strength of the wall is not considered in the optimization process, however, it is also been calculated. Opposite to the strong axis bending, the load that applied to the length side of the wall will cause the wall bend along the direction of its thickness, which is a weak axis bending. Based on the hand calculation, the wall is a singly reinforced structure when subjecting to weak axis bending. Same as the calculation method for strong axis bending, the idea of Whitney Stress Block will be applied. The wall's nominal weak axis moment strength is calculated by using the equation below:

$$M_n = A_s f_y (d - \frac{a}{2}) \tag{8}$$

where A_s and f_y are the cross-section area and yield stress of tensile reinforcement, respectively, d is the typical effective depth, and a is the depth of the compression block. The moment strength-reduction factor of 0.9 is multiplied by the nominal moment capacity to calculate the design moment capacity of the wall. Same as the idea used in calculating the strong axis moment strength of the wall with openings, the area reduction due to the opening inside the compression block will result in the increase of the compression zone depth and the depth of neutral axis, and thus the moment strength will decrease. For the wall specimen in this study, hand calculation shows that when the wall bends about its weak axis, the depth of the compression block is 0.326" (Figure 2-6), which is smaller than the distance between the edge of openings and the extreme compression fiber for all possible opening configurations in this study. Therefore, the openings will not fall in compression zone, and the weak axis moment strength of the wall will not affect by the openings.

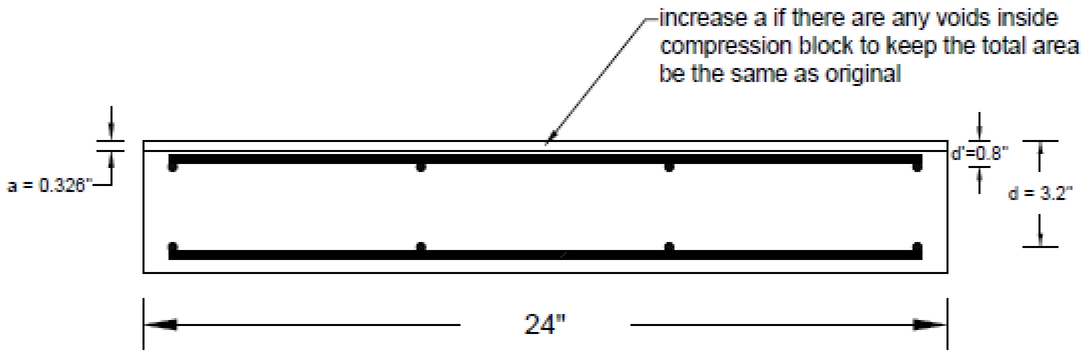

Figure 2-6. Top View of the Wall and the Compression Block in Horizontal Direction

The last strength parameter considered is the axial loading capacity. According to the 54 wall tests reported by Oberlender and Everard, buckling failures will appear if the wall is under a concentrically load and has a height to thickness ratio greater than 28, or if the wall is under an eccentrically load and has a height to thickness ratio greater than 16 (Wight 2016). For the wall specimen in this study, the height to thickness ratio is 15, which is smaller than any of these two values, therefore, buckling failure is assumed not to happen to the wall under axial load. The axial compressive strength of the wall is considered to be similar to that of a reinforced concrete column member. According to ACI 318-14 Building Code, the axial load capacity of a reinforced concrete column member is equal to the sum of axial load capacity of both concrete and steel. Based on the 564 column samples tested at the University of Illinois and Lehigh University, the strength of the concrete loaded as a column has a coefficient of 0.85 in front of its original strength. Thus, the axial compressive strength of the wall can be summarized as:

$$P = 0.85f'_c(A_g - A_{st}) + f_y A_{st} \tag{9}$$

where $f'c$ is the compressive strength of concrete, A_g is the gross area of the top surface of the wall, A_{st} is the total area of the longitudinal reinforcement, and f_y is specified yield strength of the steel reinforcement. With different liquid tube opening configurations, the top surface area of the wall will change. Therefore, by subtracting total area of the openings, the axial compressive strength of the wall with different tube arrangements can be calculated. The modified equation for calculating the axial load strength of the wall with circular openings can be expressed as:

$$P = 0.85f'c\left(A_g - A_C - A_{st}\right) + f_y A_{st} \tag{10}$$

where the new parameter, A_c, is the total area of the openings on top surface of the wall. ACI 318-14 Building Code requires the design axial strength to be calculated by multiplying a reduction factor of 0.85 to the calculated axial compressive strength for normal transverse reinforcement case, which is applied to this study.

Detailed hand calculations pertaining to the above strength parameters can be found in Appendix A, and the calculation results for all possible combinations of the hole sizes are listed in Appendix B.

2.3.2 Damping Effect of TLWD

Damping effect of TLWD is the second objective in this multi-objective optimization, as the liquid column sizes and number change, its damping capacity will be different. The procedure of calculating a TLWD's damping effect with respect to different column arrangements has been studied by Wu et al (Wu et al. 2017). A dynamic analytical model for TLWD from Wu et al. (2017) is used to calculate the damping effect the TLWD system, and the results are used to further optimize the TLWD system. Generally speaking, the damping effect of the TLWD system is represented by the maximum displacement response of a Single

Degree of Freedom (SDOF) structure that attached with a TLWD under a harmonic sweep. The schematic drawing of the model is shown in Figure 2-7, where x_s is the displacement of the structure, $P_0 \sin(\omega t)$ represents the harmonic excitation force with varying frequency ω, and H is the average liquid height inside the columns of the TLWD system. For different combinations of column sizes and number, the goal is to find the optimal H value to tune the natural frequency of the TLWD to that of the SDOF structure. For each H value, the maximum displacement responses of the structure are simulated across all frequencies, and the peak value of the displacement versus frequency curve is selected to represent the damping effect of the TLWD system. The numerical calculation of the damping effect of the TLWD system can be summarized as a minimum-maximum process:

$$min\{max(x_s)\,,\ 0 < \omega < \infty,\ 0 < H < H_{max}\} \tag{11}$$

where H_{max} is the maximum possible height of the liquid height, which is taken as the height of each column.

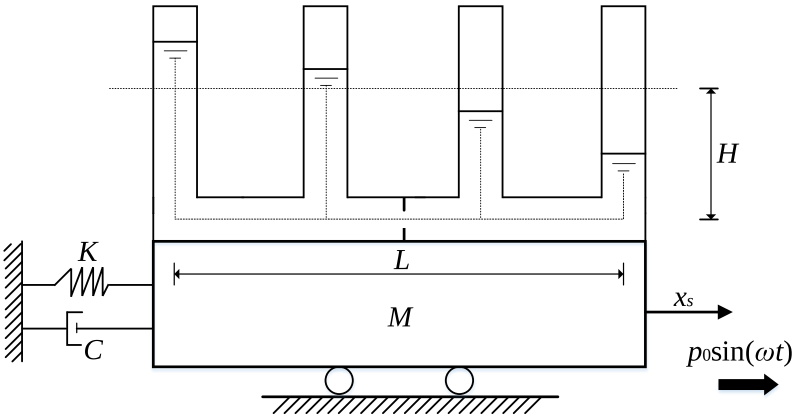

Figure 2-7. SDOF Structure Attached with TLWD

2.4 Multi-objective Optimization

2.4.1 Overview of Multi-objective Optimization Method

With the analytical results of different objectives from the previous subchapter, a multi-objective method is used to conduct the optimization for a TLWD system. When designing the TLWD system, both the damping effect and strength reduction were considered, as mentioned previously. The choice of an optimal design of TLWD can be done by taking the wall design strength, which includes moment of inertia, shear capacity, moment capacity, and bearing capacity, and damping effect of TLWD into account. Generally speaking, the optimal design problem is concerned with the stiffness, and shear, moment, and bearing capacities of the wall with holes and the effectiveness of the TLWD that will be installed inside the wall. In this study, the four strength parameters are equally weighted in doing the optimization since all of them are considered to be equally important. For example, the flexural failure, shear failure and axial loading failure are the three types of failures of a wall, and either of these failures will cause the wall be unusable, so all these three types of failure are expected to be avoid. Also, the moment of inertia of a wall represents its stiffness, as mentioned in chapter 2.3, the stiffness reduction of the wall may result in the chain effect of the capacity reduction of a wall, such as to increase the impact of the openings to the strengths of a wall. Therefore, the four strength parameters will share the same weight in the optimization. On the other hand, based on the results for all the optimization objectives in Appendix B, it can be seen that the percentage of the variation of damping effect is relatively larger than the four strength parameters, so the weight of the damping effect is considered to be the same as each of the other four strength parameters to avoid to overweight the damping effect.

In the optimization, the global criterion method, which includes the minimization of all the objective functions, is used to solve the multi-objective problem (Davalos and Qiao 1996).

In this method, the optimal solution is found by minimizing the objective function, which is defined as the sum of the squares of the relative deviation of the objective from the ideal solution. Meanwhile, the optimization is defined as a constrained multi-objective optimization problem, which means the different choices toward the optimization process happen within upper and lower bounds. The overall optimization process can be described in four steps as shown in Figure 2-8. The first step is to set up the upper and lower bounds of the design outcomes. In our study, with the restraint of the size of the wall specimen as well as the availability of PVC pipe sizes on the market, the range of column diameter, D, is 0.84" $\leq$ D $\leq$ 1.66", and range of tube number, n, is $2 \leq n \leq 14$. The second step is to calculate all the optimization objectives by following these two constraints. This step is described in detail in chapter 2.3, and the calculated results will be used as analytical solutions to compare with lab testing results and numerical simulation results in the next two chapters. The third step is the main step for doing the optimization. The objective functions will be used in the equation that considers global criterion. In this study, the total amount of combinations of tube sizes and number is fixed, so the values of each objective can be treated as discrete numbers $f_j(x)$ instead of a continuous function. For each objective, the ideal solutions will be regarded as target points $f_j(x^*)$ in the design domain. The global criterion method is based on calculating the sum of the squares equation:

$$\sum_{j=1}^{k}\left(\frac{f_j(x)-f_j(x^*)}{f_j(x^*)}\right)^2 \tag{12}$$

where j represents different objective functions and k is the number of objective functions that we have. The vector minimum equation, which aims to find the smallest value from the above equation, can be describes as:

$$min \sum_{j=1}^{k} \left(\frac{f_j(x)-f_j(x^*)}{f_j(x^*)}\right)^2 \tag{13}$$

subjected to the constraints mentioned above. The last step in the minimization process is to select the optimal solution. In the vector minimum equation shown above, by adding the squares of the relative deviation of the objective from the ideal solutions together, all the objectives are considered, and the minimum value indicates the optimal design. The final design of the TLWD system is based on this optimal result.

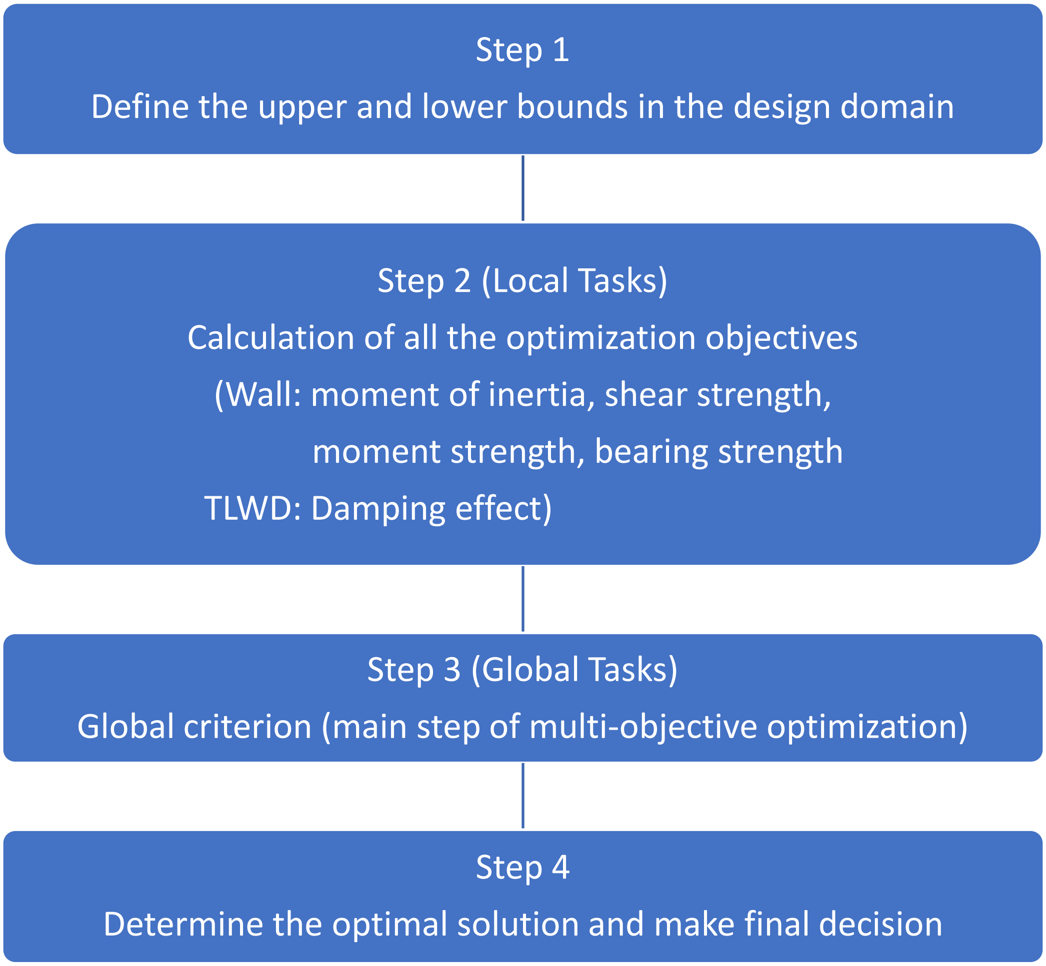

Figure 2-8. Overall Process of Multi-objective Optimization of TLWD System

2.4.2 Optimization Results and Discussions

Using the calculated results and optimization techniques presented earlier, the optimal design of a TLWD system subjected to column size and number constraints is carried out. The four parameters of the wall strength and the TLWD's damping effect with respect to different column sizes and number are shown in Figures. 2-9 (a) through (e), respectively, which are drawn with the Origin graphing software by composing a surface covering all the discrete solutions from each optimization objective. In the contour surface charts, different colors indicates the corresponding vertical axis values, where dark red indicates the greatest and dark purple indicates the smallest values. Based on the surface charts, it can be seen clearly that with the least number along with the smallest size of openings, the wall will have the largest strengths. However, for the damping effect of TLWD, it can be seen that the more tube number, the higher value the damping effect will be. In Figure 2-9 (e), the colors on the surface chart change more obvious along the tube number axis, this indicates the significant impact of the tube number with regard to the TLWD's damping effect.

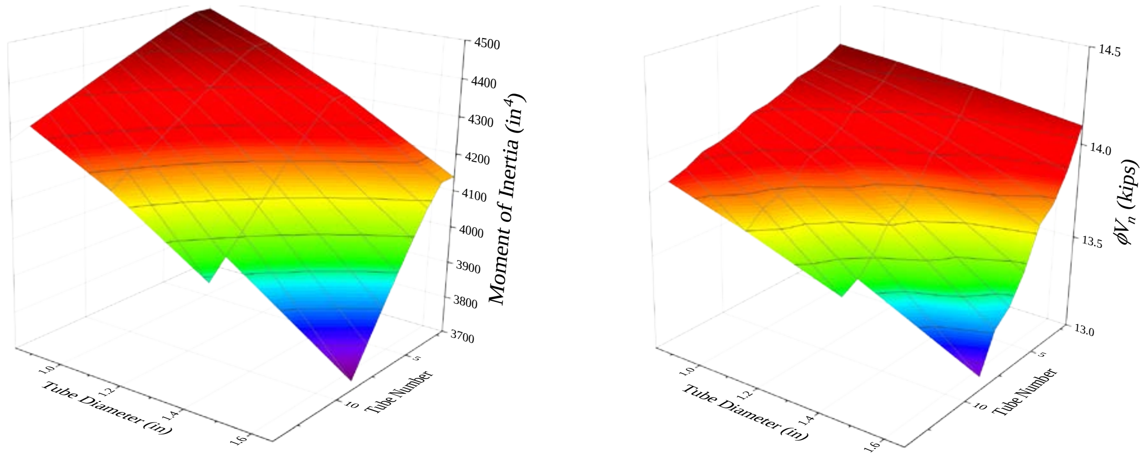

(a) (b)

Figure 2-9. Influence of Tube Diameter and Tube Size on (a). Moment of Inertia of Wall; (b). Shear Strength of Wall; (c). Moment Strength of Wall; (d). Axial Load Strength of Wall; (e). Damping Effect of TLWD

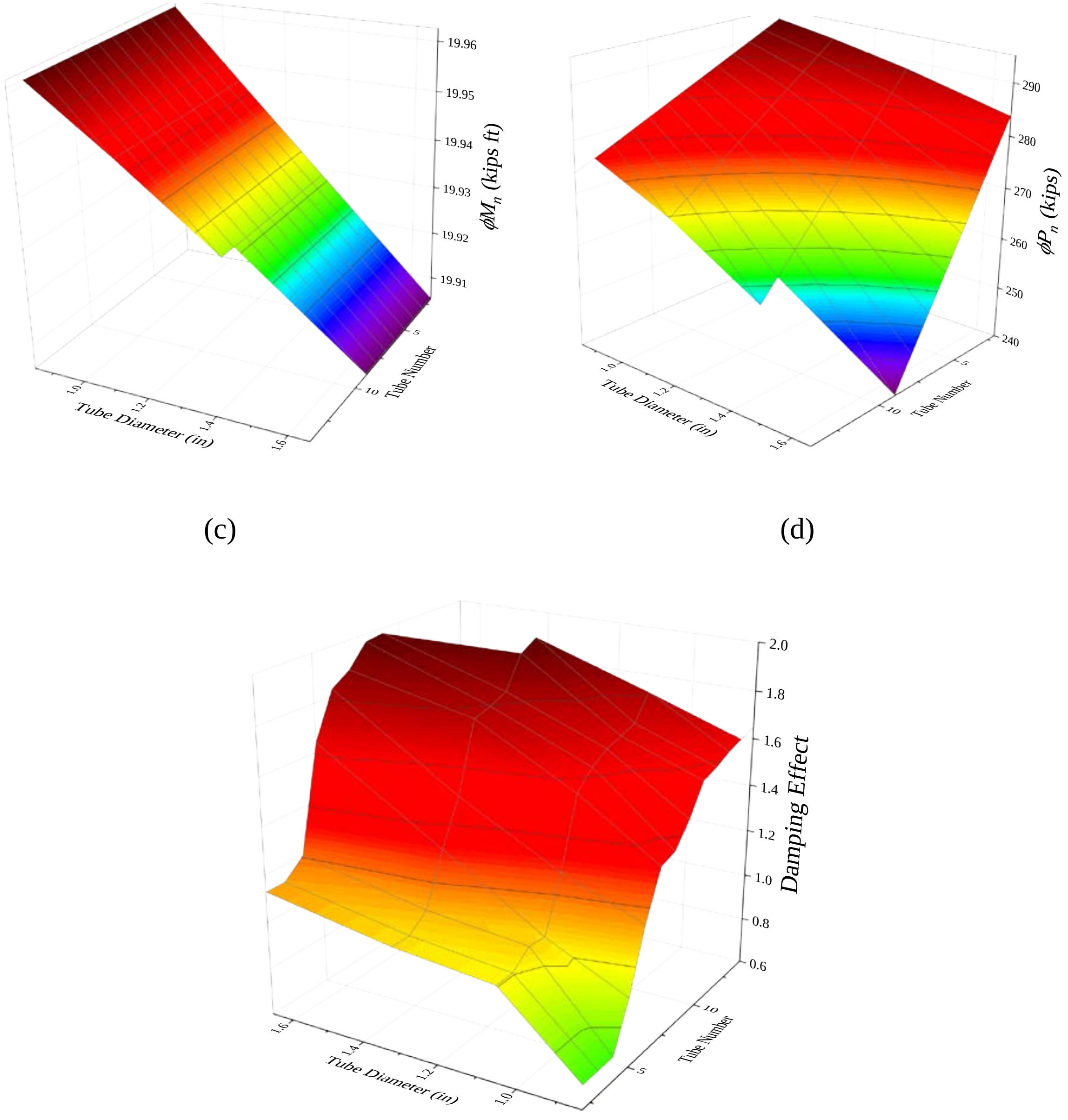

(c) (d)

(e)

Figure 2-9. (continued)

Since the wall strength and the TLWD's damping effect are expected to be as large as possible, the ideal solutions for these optimization objectives are the maximum values, and these values from the objective functions are selected as target points. The vector minimum equation, equation 12, which aims to carry out the global task, is to consider the calculated results of all the objectives from the local task. The minimum of this equation represents the maximum of the local objectives, and the optimization of the problem. From the calculation, the optimal solution of tube diameter and number are given as 1.315 in. and 7 respectively. The surface chart of vector minimum value versus tube diameter and number is shown in Figure 2-10.

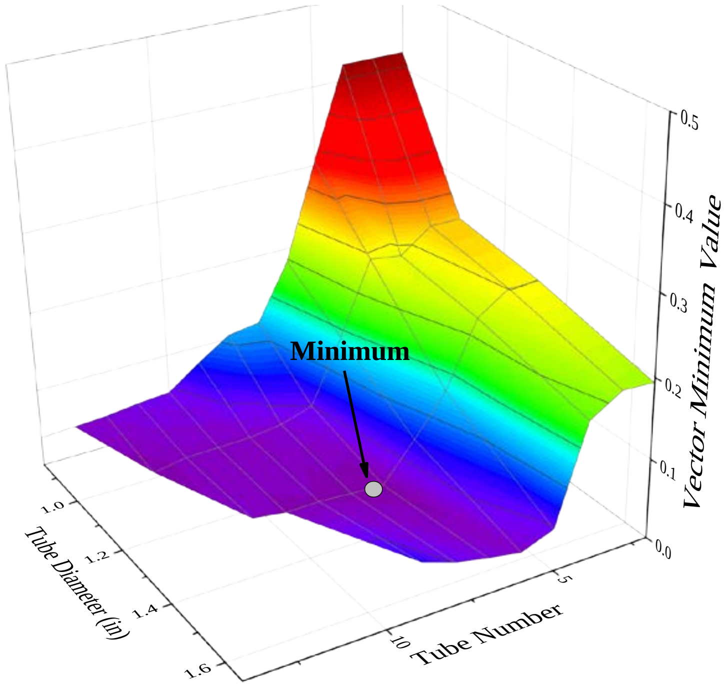

Figure 2-10. Surface Chart of Vector Minimum Value with respect to Tube Diameter and Tube Number

In general, the multi-objective optimization method starts with the local task, once the individual objective is optimized, a global task is then proceed by accounting all the parameters together. The overall optimal result is obtained by selecting the best solution from the global task. With this approach, the ideal design of the TLWD system among a wide range of combinations of tube sizes and number under previously defined constraints can be achieved and will be used as the opening configuration of the wall specimen in both lab testing and finite element modeling.

CHAPTER 3. EXPERIMENTAL INVESTIGATION

3.1 Test Plan

The objective of this experiment is to study flexural behavior of reinforced concrete walls with circular openings, which are formed by placing PVC pipes in place before pouring concrete, based on four-point bending tests on two wall panels. The size and number of the openings are from the optimal solution from Chapter 2. The panels will be tested until failure.

3.2 Materials

Due to the size limit of the wall panel, the concrete cover along the thickness of the wall panel needs to be smaller than normal aggregate size. Therefore, concrete (chip mix) with an average aggregate diameter of 3/8 inch was selected.

Nine concrete cylinders were constructed, with three in each group, to obtain compressive strengths at three specific times. The compressive tests were conducted according to ACI standards, which requires to test the cylinders at 7 days and 28 days after pouring. The compressive strength at 28 days was used to calculate the concrete’s modulus of elasticity. The remaining group of three cylinders were tested before testing the second specimen. All the cylinder tests were done utilizing the SATEC machine shown in Figure 3-1, where the top pad of the machine exerts a compressive pressure to the cylinder. The concrete compressive strengths and standard deviation for each group specimens are shown in Table 3-1, and the average values are taken as the concrete strength at these specific times.

Figure 3-1. SATEC Machine for Cylinder Test

Table 3-1. Results of Compressive Tests of the Cylinders at Seven Days after Pouring the Concrete, Dates for Testing the First and Second Specimens, the Average Value and the Standard Deviation for Each Group of Cylinders

	Cylinder 1 (psi)	**Cylinder 2 (psi)**	**Cylinder 3 (psi)**	**Average (psi)**	**Std.**
7 Days	4653	4539	4666	4619	69.87
28 Days (First Specimen)	5855	5776	5660	5764	98.08
41 Days (Second Specimen)	6504	6535	6461	6500	37.16

The reinforcing bars were purchased from aSa Rebar Company. The stress-strain relationships of the rebars were obtained from uniaxial tensile tests on four specimens. The test setup is shown in Figure 3-2. A two-foot long rebar with a strain gauge attached in the middle is supported by two hydraulic wedge grips on both the top and bottom of the bar. The top grip remains fixed while the bottom grip moves down, creating a tensile force on the bar. The rebar is tested under this tensile force until fracture occurs. The tensile forces and strains at different times during testing can be read from the machine and a data acquisition system. The stress of the rebar can be calculated by dividing the force by its cross-section area. Thus, the stress-strain diagram can be generated, as shown in Figure 3-3 for the four test specimens. According to the test data, the average stress that causes the nonlinear behavior of the specimens is 84 ksi, with an average strain of 0.003039. The average yield stress is 98 ksi, which corresponds to about 0.002 offset from the strain where nonlinear behavior starts, and the corresponding average strain is 0.005038. The average ultimate strength of the rebar is 109 ksi with a corresponding average strain of 0.03811. These values are summarized in Table 3-2.

Figure 3-2. Steel Uniaxial Tensile Test Setup

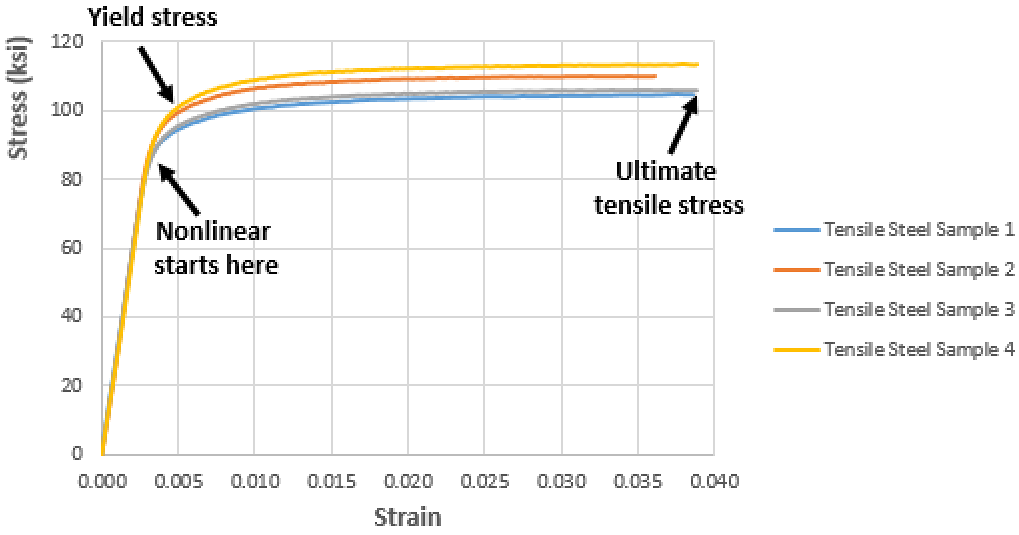

Figure 3-3. Stress-Strain Curve of the Test Rebar Specimen

Table 3-2. Stress and Strain Data at Specific Points for Test Specimens and the Average

	Specimen 1	Specimen 2	Specimen 3	Specimen 4	Average
Nonlinear Stress (ksi)	81	86	83	87	84
Nonlinear Strain	0.002875	0.003052	0.003065	0.003162	0.003039
Yield Stress (ksi)	94	99	96	101	98
Yield Strain	0.00488	0.005062	0.005074	0.005136	0.005038
Ultimate Stress (ksi)	105	110	106	113	109
Ultimate Strain	0.03864	0.03615	0.03882	0.03882	0.03811

The PVC pipes used in this test are Charlotte 200-psi type with thin wall thickness, and have a maximum working temperature of 140 degrees Fahrenheit. No tests were conducted on the pipes since they have low stiffness and strength, and only occupied a small area, the purpose of the pipes is to act as molds so that holes can be formed when pouring concrete.

3.3 Test Setup

The reinforcing bars used arrived in 20 foot increments. They were cut into the required lengths using a bolt cutter (Figure 3-4). PVC pipes were 10 feet long and were cut using a miter saw (Figure 3-5). The clear cover of rebar and PVCs specifed is ¾ inch along the height and length of the wall panel, and 0.425 inch along the thickness of the wall as mentioned in chapter 2.2.

Figure 3-4. Bolt Cutter Used in Cutting NO.2 Bars

Figure 3-5. Miter Saw for Cutting the PVC Pipes

3.3.1 Four-point Bending Test

A four-point bending test was utilized to determine the flexural performance of the walls. For the four-point bending test, two wall panels were manufactured. The mold of the test specimen was built using steel forms, which were connected by clamping bolts. Circular plywood blocks that have the same cross sectional area as the interior portion of the PVC pipes were connected to the steel forms at the PVC pipe locations (Figure 3-6) to support and hold the PVC pipes in place during concrete pouring.

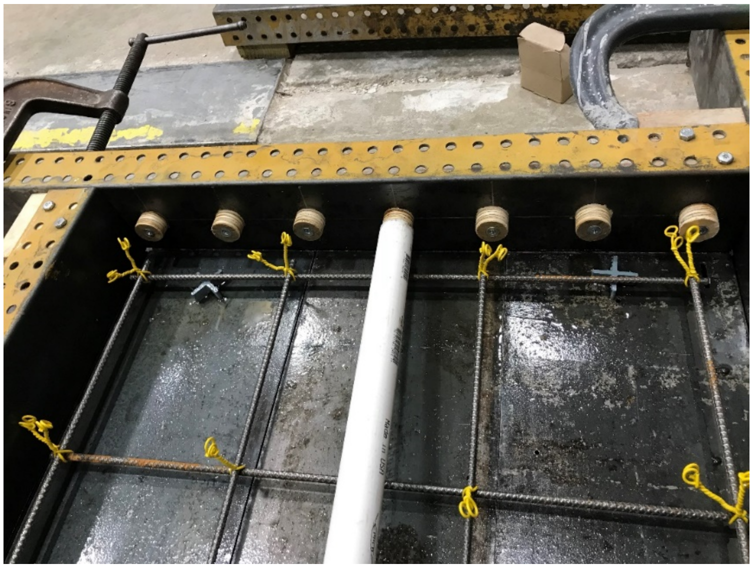

Figure 3-6. Plywood Blocks Impaled to the Steel Plates to Support PVC Pipes

In the four-point bending test, the wall panels are laid flatwise and supported by steel rods at each end. The left rod is fixed to the bottom steel plate to simulate the pin support and the right rod is free to move to simulate the roller support. The distance between the edges of the wall panel and the center of the rods is 2 inches. Two 3 inch steel plates are placed at thirds of the wall. The plates form strips, and an I-beam is placed on top. The load applied by the actuator on the top transfers through the I-beam and evenly distributed to the two steel plates. The test setup with detailed dimensions is shown in Figure 3-7 and the equipment setup in the lab is shown in Figure 3-8.

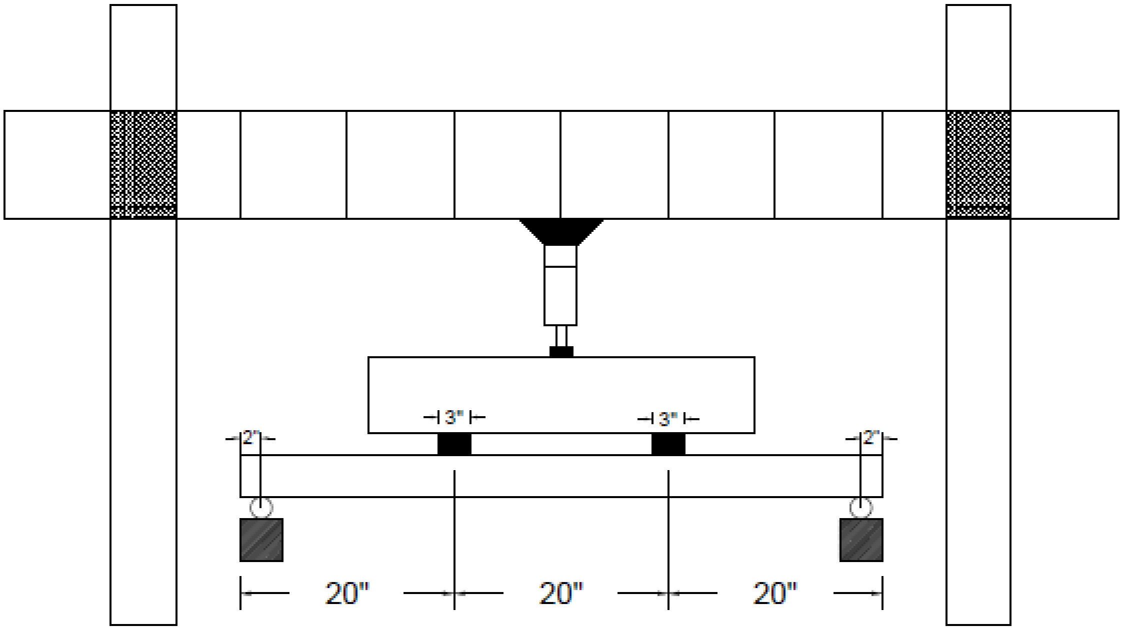

Figure 3-7. Four-point Bending Test Detailed Drawing

(a) Front View

(b) Side View

Figure 3-8. Four Point Bending Test Equipment Setup in the Lab

Strain gauges were used to measure strains at critical locations of concrete and reinforcing bars. For concrete, PL-60 type strain gauges were installed on both compression and tension sides when the wall bends. On the compression side, three gauges are installed in the middle of the wall and one gauge is installed next to the load strips. On the tension side, the locations of the strain gauges are the same, except the number of strain gauges in the middle of the wall is reduced to one. For the two layers of reinforcements, FLA-1 type strain gauges are installed, with two beside each of the load strip areas, and two at the middle of the wall. The locations of concrete gauges and steel gauges are shown in Figures 3-9 and 3-10, respectively. Five LVDTs are used to measure deflections at the two load strips and the mid-span of the wall panels, as shown in Figure 3-11. All LVDTs are attached to the bottom surface of the wall panel.

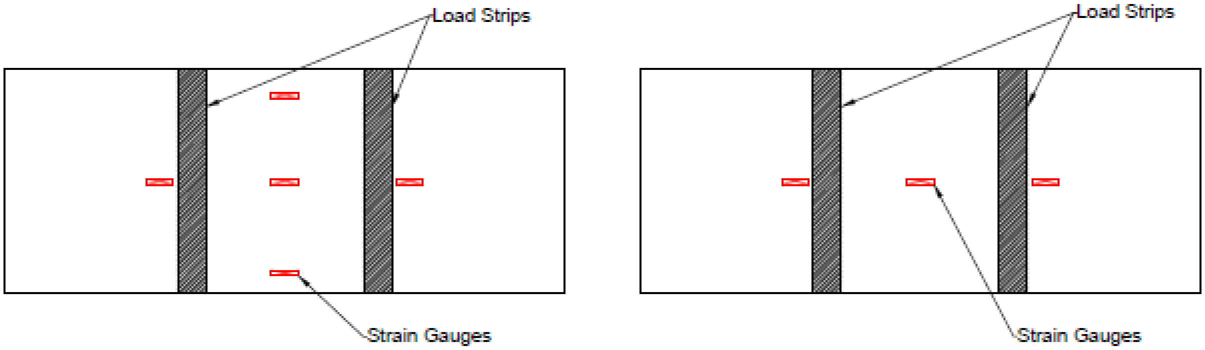

(a) (b)

Figure 3-9. (a) Locations of Concrete Gauges on Compression Side; (b) Locations of Concrete Gauges on Tension Side

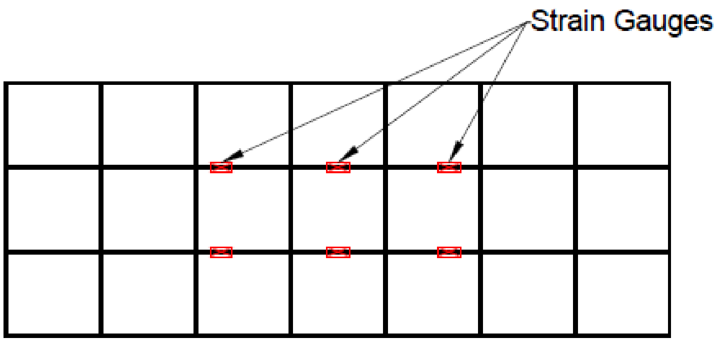

Figure 3-10. Locations of Steel Gauges

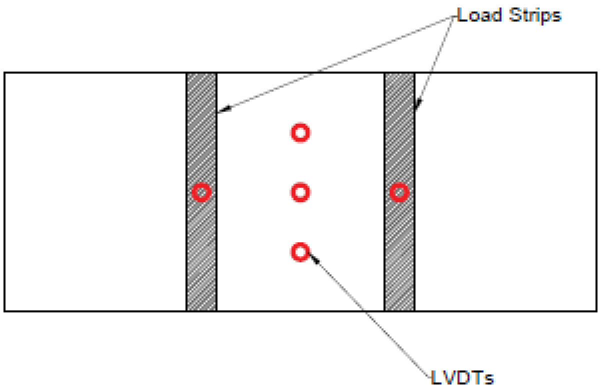

Figure 3-11. Locations of LVDTs

3.4 Test Results

3.4.1 Four-point Bending Test

At the beginning of the test, force control method is used. The load is applied in 500 lbs increment at each time. For both wall panels, cracks starts to appear at the tension side near the loading points when 3 kips is applied. As the load increases, the cracks propagate and more cracks appear in the pure bending zone between the two loading strips. According to the uniaxial tensile test mentioned above, the average yield strain of the reinforcement is 0.005038. During the test, it was found that when the displacement at mid-span reached 0.4 inches, the increase speed of the load significantly dropped, indicating that the bottom flexural reinforcement had begun to yield. This was verified by the output data from one of the strain gauges at the middle of the bottom reinforcement. Figure 3-12 shows the maximum strain at the bottom layer of the reinforcement versus the displacement at the mid-span of the wall panel, and the arrow indicates the yielded of steel from the uni-axial tensile test. It is clear that for both panels, the strain values of bottom reinforcement reached the yield strain when there is a 0.4 inches displacement at mid-span. After the flexural reinforcement yielded, testing was continue utilizing a displacement control method with a 0.1 inch displacement increment at the mid-span until the panel failed. The diagrams of the load versus displacements at mid-span, left load strip and right load strip are shown in Figures 3-13 (a) through (c) respectively, in the diagrams, the load pertains to the load that was distributed at each load strip. The displacement at the mid-span is the average value from the three LVDTs. The deflection shape of the wall panel at failure is shown in Figure 3-14.

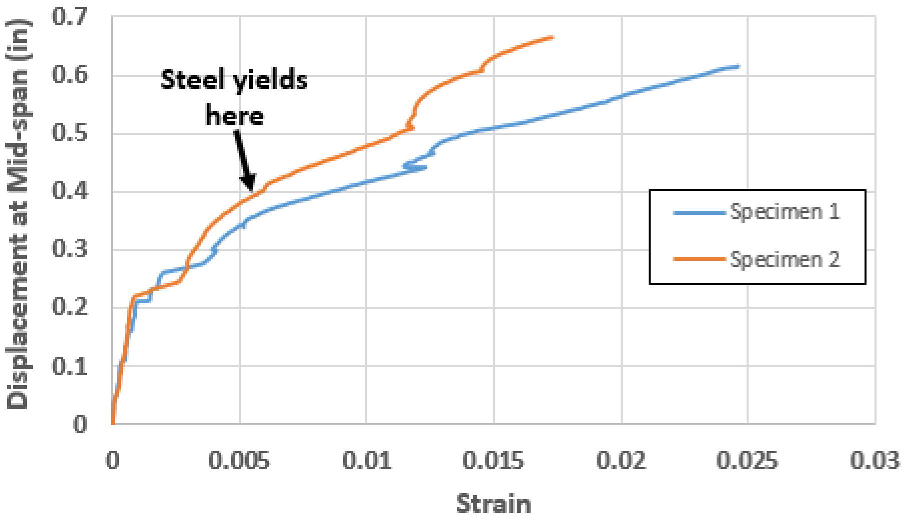

Figure 3-12. Strain on middle part of bottom reinforcement versus Displacement at Mid-span Diagram

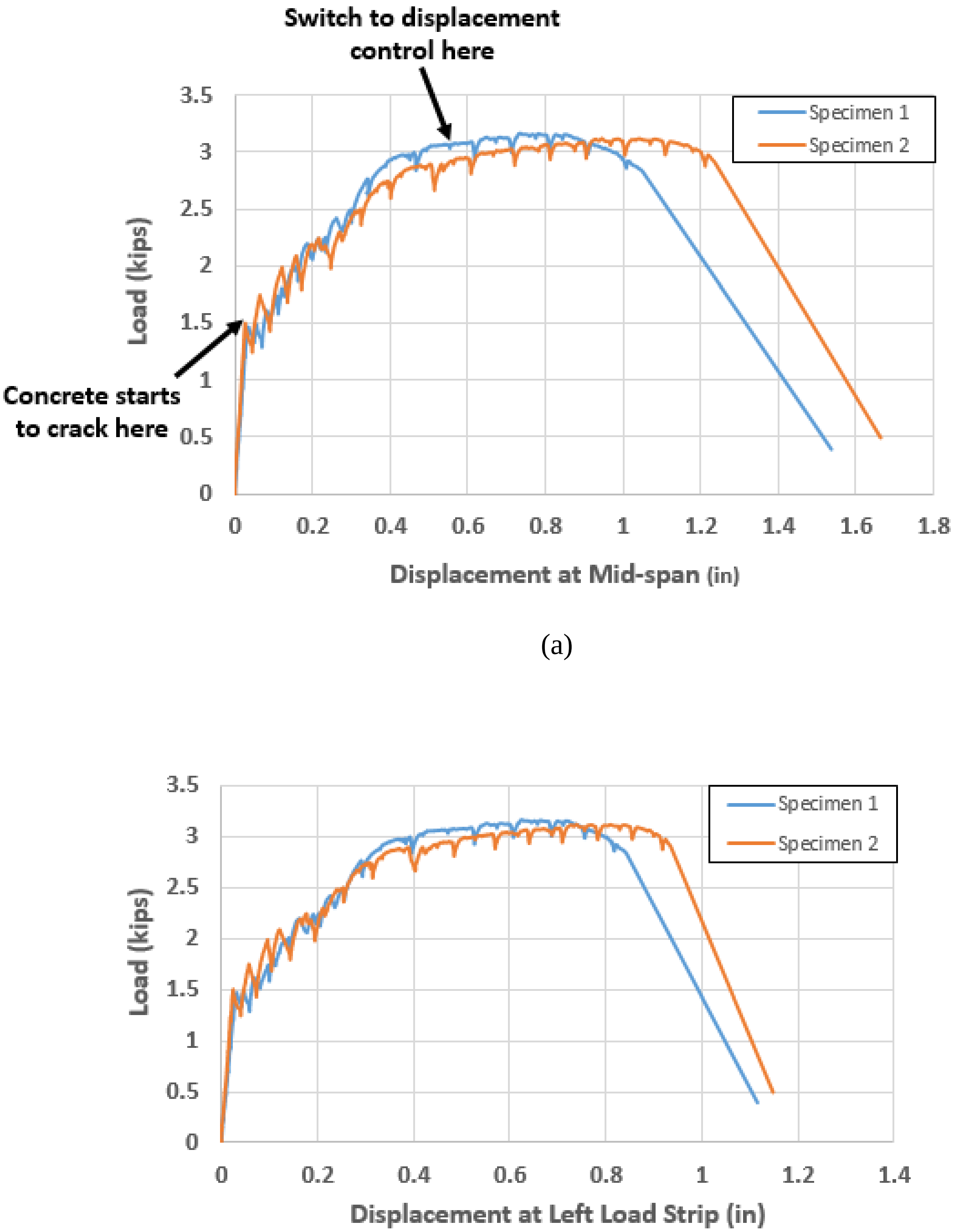

(a)

(b)

Figure 3-13. (a). Load versus Displacement at Mid-span of concrete Diagram; (b). Load versus Displacement at Left Load Strip Displacement Diagram; (c). Load versus Displacement at Left Load Strip Diagram

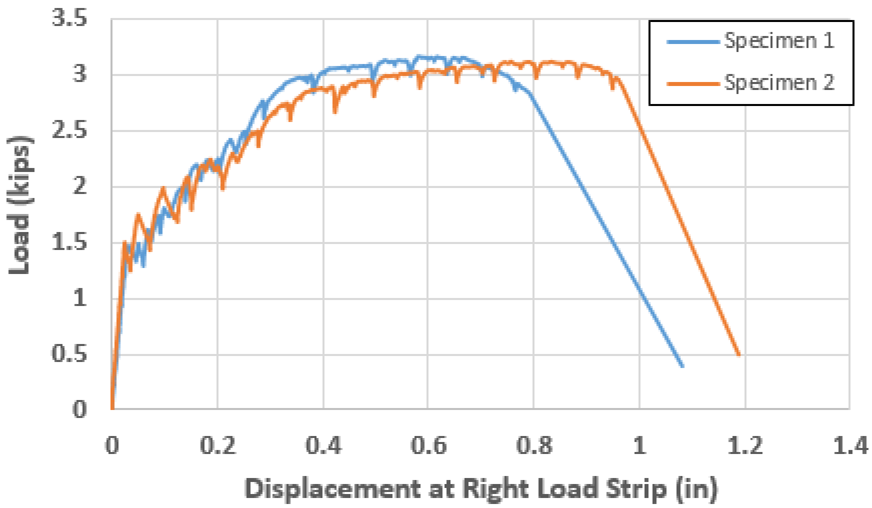

(c)

Figure 3-13. (continued)

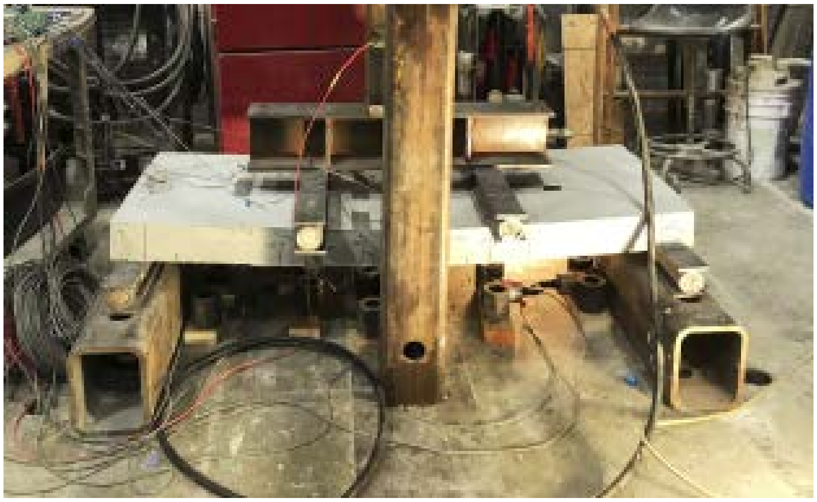

Figure 3-14. Deflection shape of the wall at failure

The strain gauges that attached to the mid-span of the concrete top surface aim to measure the compressive strain of the concrete at that location. The order of mid-span strain gauges on top surface of the concrete is shown in Figure 3-15, and the diagrams of the strain data from these three gauges at mid-span versus load for the two test specimens are shown in

Figure 3-17. Additionally, the diagrams of load versus strains on top surface of concrete at left and right load strips are shown in Figure 3-16. Note that the strain gauge attached to the left load strip of wall specimen 1 does not work properly, and therefore the data is discarded.

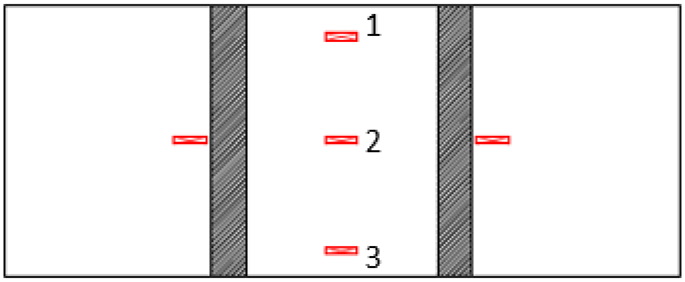

Figure 3-15. Mid-span Concrete Top Surface Strain Gauge Order

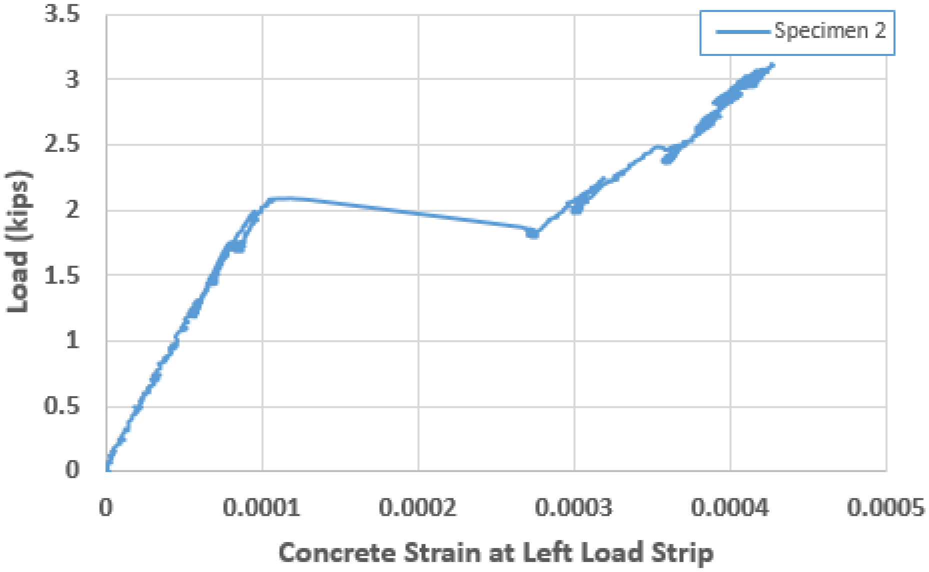

(a)

Figure 3-16. (a). Diagram of Load versus Concrete Top Surface Strain at Left Load Strip; (b). Diagram of Load versus Concrete Top Surface Strain at Right Load Strip

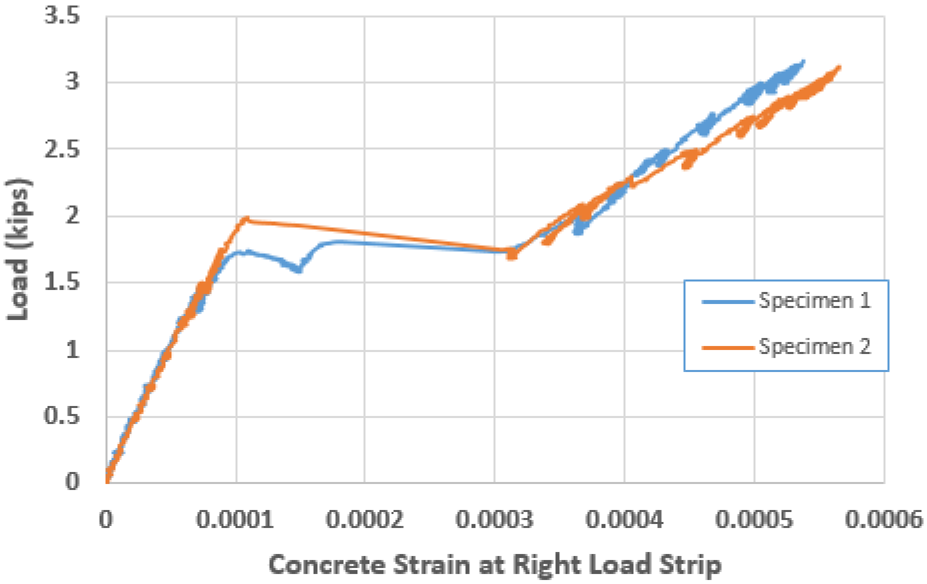

(b)

Figure 3-16. (continued)

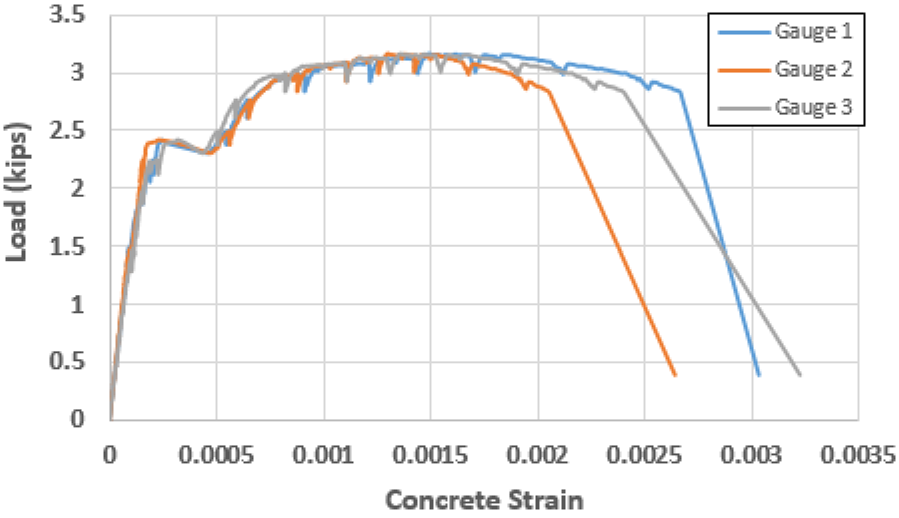

(a)

Figure 3-17. (a). Diagram of Load versus Mid-span Concrete Top Surface Strain for Wall Specimen 1; (b). Diagram of Load versus Mid-span Concrete Top Surface Strain for Wall Specimen 2

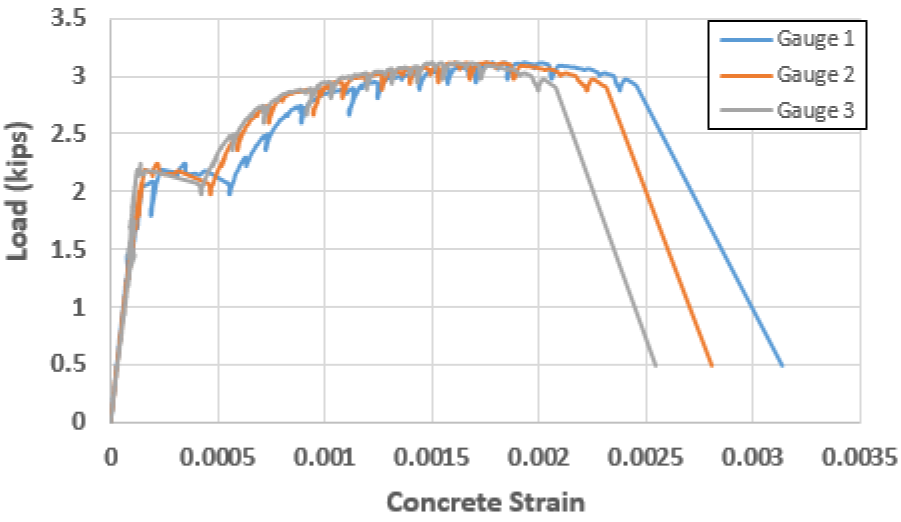

(b)

Figure 3-17. (continued)

ACI suggests the ultimate concrete compressive strain is 0.003, and that the concrete is assumed to be crushed when the concrete strain reaches this value. It can be seen from Figure 3-16 that the trend of the increasing of concrete strain at left and right load strips are almost the same for both two wall panels, and the concrete strain at the failure stage is well below 0.003. Because the maximum compressive strain happens at the mid-span of the concrete top surface, so the strain data from all the three gauges are drawn on the load-strain diagrams in Figure 3-17. According to the diagrams, the immediate drop of the curve indicates the failure of the reinforced concrete wall system. When the system fails, the strain values on top surfaces of the two wall specimens are all smaller than 0.003 for all the gauge locations along the mid-span. Therefore, the concrete does not crush at the top. This is also been verified after checking the top surface of the concrete. Figure 3-18 shows the top surface of concrete for the two wall specimens after the systems fail, and it can be seen that the concrete does not crush in the extreme compression fiber. However, after checking the reinforcements inside the wall, it was found that the flexural reinforcing was broken in the middle (Figure 3-19) in both of the testing specimens. Cracking had initiated in the center of the wall; after initiation of cracking, the flexural reinforcing failed. After failure, the crack in the middle opened significantly and extended towards the top of the wall. The major crack in the middle of the wall and the crack patterns of each wall panel are shown in Figures 3-20 and 3-21, respectively.

In looking at the strain values for the top reinforcing, it can be shown that the reinforcing almost makes no contribution to the flexural capacity of the wall when in bending about the weak axis. Figure 3-22 compares the strain values at the middle of top and bottom longitudinal reinforcements. For both wall panels, the strain at the middle of top longitudinal reinforcement is almost zero, in contrast, the strain at the middle of bottom one increases at the beginning and reaches the peak value when 0.6 to 0.7 inches displacement occurs at mid-span of the wall. Therefore, only bottom rebar should be counted when calculating the reinforcement ratio of the wall. It is concluded that when designing the wall that need to consider weak axis bending moment, the flexural reinforcement in the far tension zone needs to be carefully designed so that the wall can have enough moment capacity along the weak axis.

(a)

Figure 3-18. (a). Top Surface of Wall Specimen 1; (b). Top Surface of Wall Specimen 2

(b)

Figure 3-18. (continued)

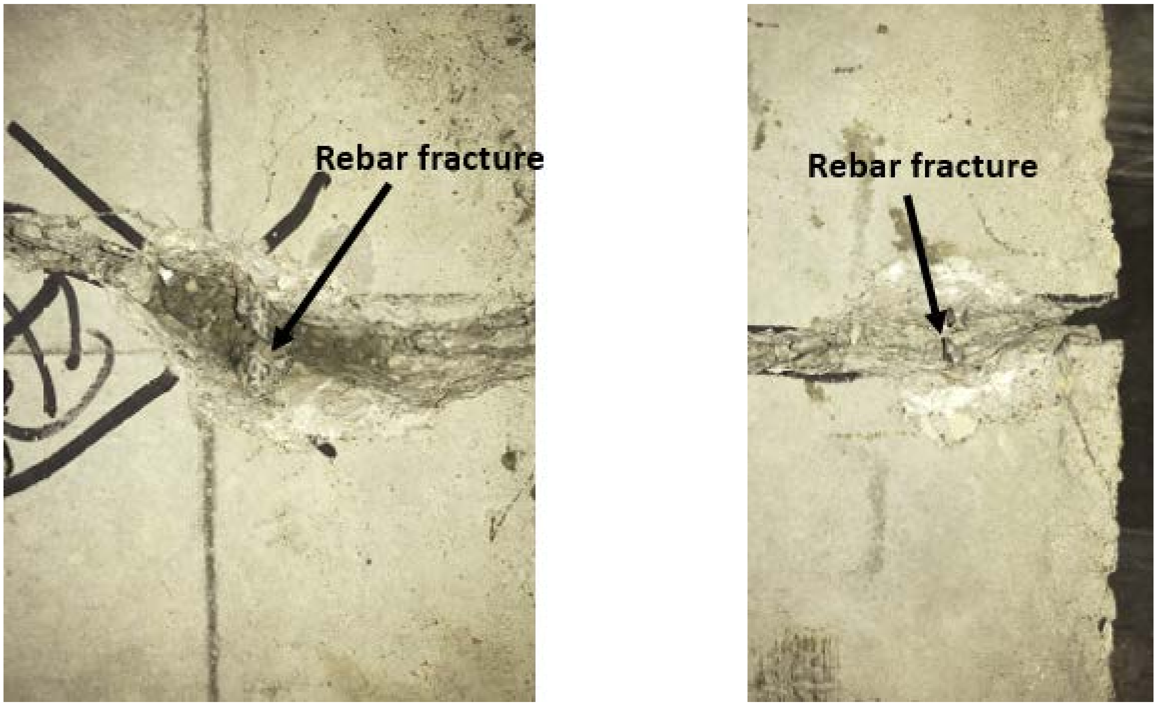

(a) (b)

Figure 3-19. (a). Interior Bottom Layer Flexural Reinforcement Fracture; (b). Exterior Bottom Layer Flexural Reinforcement Fracture

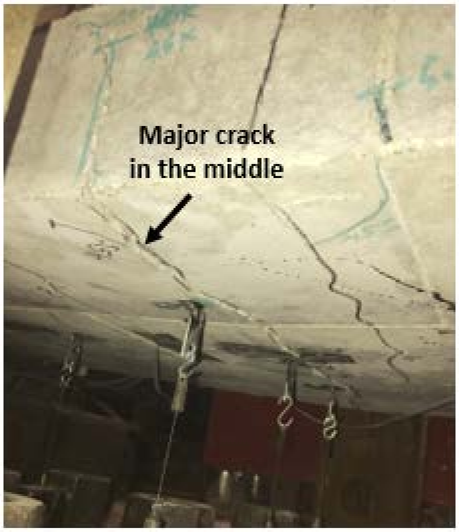

Figure 3-20. Major crack in mid-span of the wall

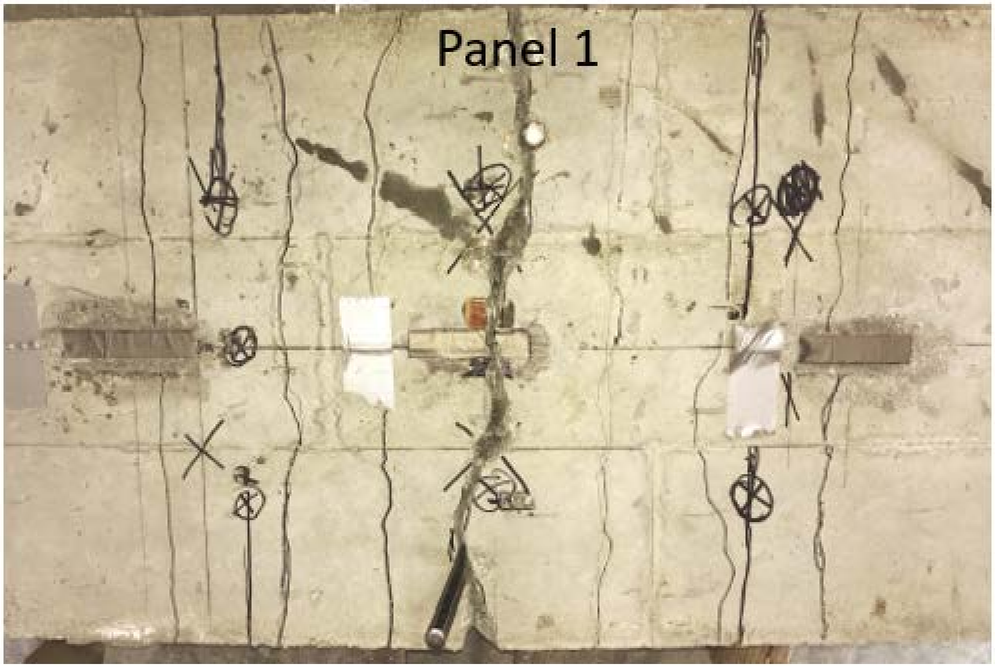

(a)

Figure 3-21. Crack Patterns on Bottom Surface of the (a). Wall Panel 1; (b). Wall Panel 2; (c). Comparison of the Cracks along the Thickness Side of the Two Panels

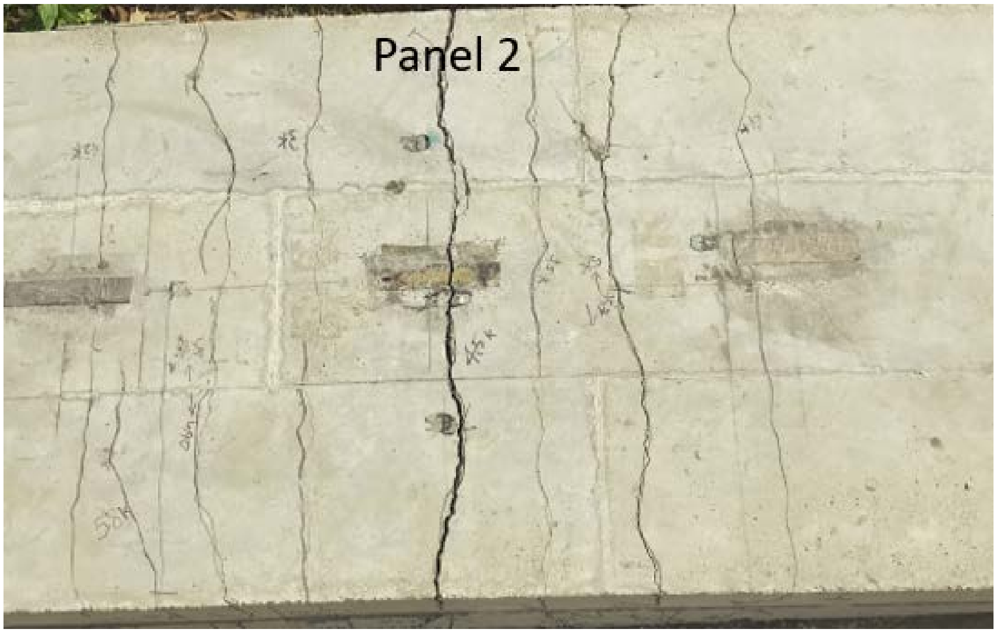

(b)

(c)

Figure 3-21. (continued)

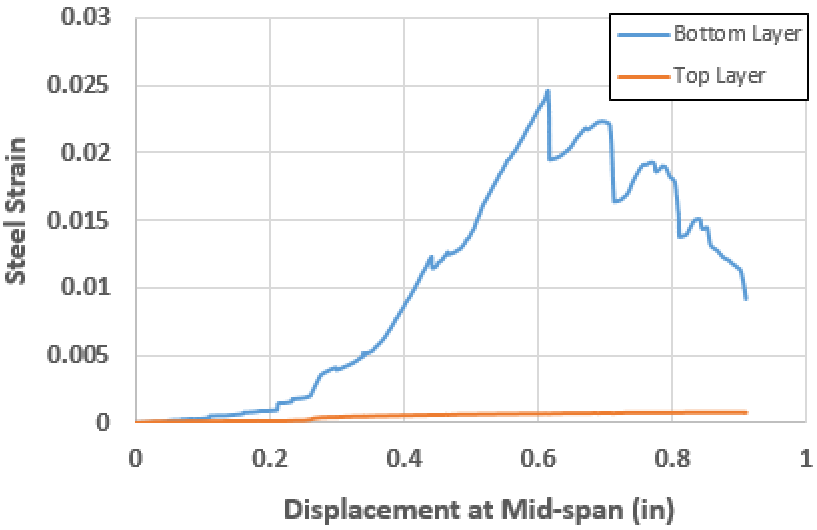

(a)

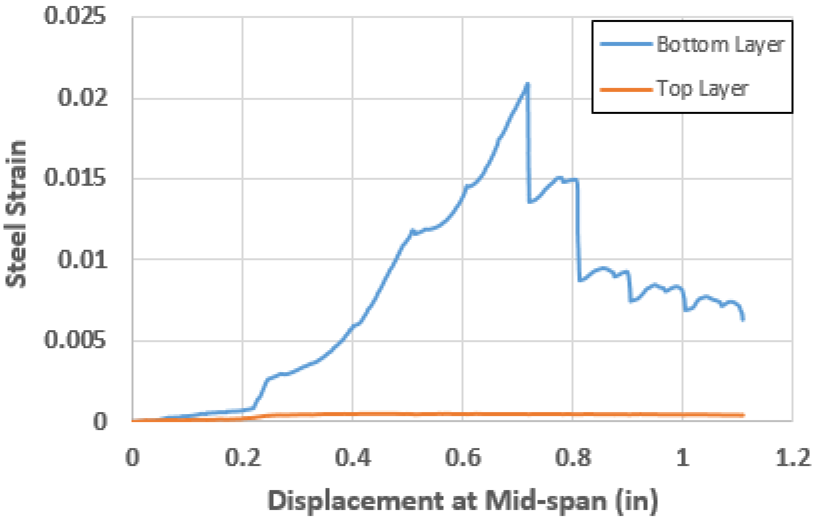

(b)

Figure 3-22. (a). Diagram of Displacement at Mid-span of Wall versus Strain at Middle of the Bottom and Top Layer Longitudinal Reinforcements for Wall Specimen 1; (b). Displacement at Mid-span of Wall versus Strain at Middle of the Bottom and Top Layer Longitudinal Reinforcements for Wall Specimen 2

To explore the increasing of the strain in the middle of the bottom layer of flexural reinforcements with respect to the load, the order of middle part of bottom flexural reinforcements is shown in Figure 3-23, and the diagrams of the strain data from these two gauges versus load for the two wall specimens are shown in Figure 3-24. The diagrams tell that for both wall panels, the strain increase fast at the beginning, and when the load reaches about 3 kips, which indicates the yielding of the steel according to the load versus mid-span concrete displacement diagrams in Figure 3-13, the load will almost remain the same but the reinforcements strain increases faster. It is observed that the ultimate strain of the reinforcements under bending load is about 0.02, which is smaller than when the reinforcements under tensile force, but the yielding strain of the reinforcements under bending load is around 0.005, which is same as the tensile load case. Therefore, it is concluded that the ultimate strain of the steel will be different if the steel is subjecting to different loading conditions, but the yielding strain will not be affected by those different loading conditions.

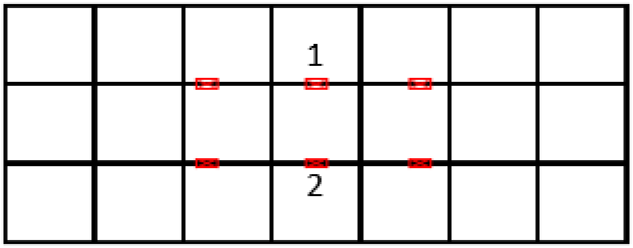

Figure 3-23. Middle of Bottom Layer Flexural Reinforcement Gauge Order

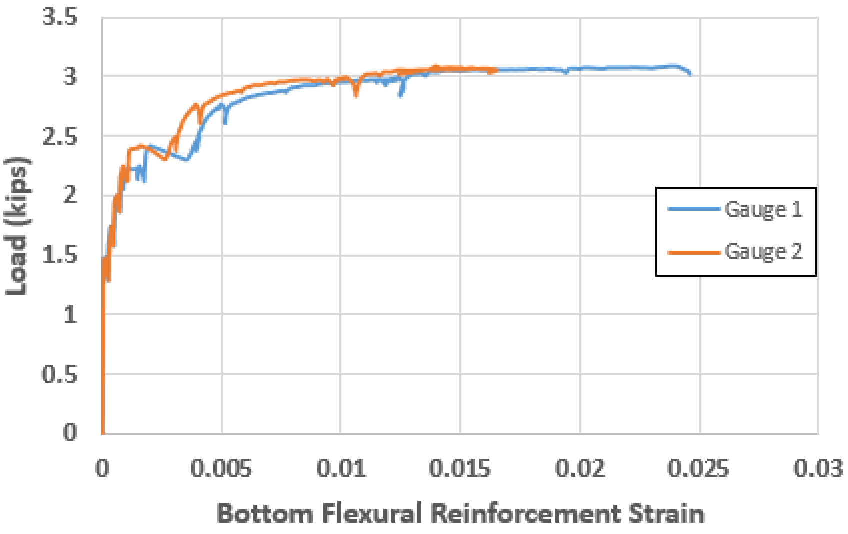

(a)

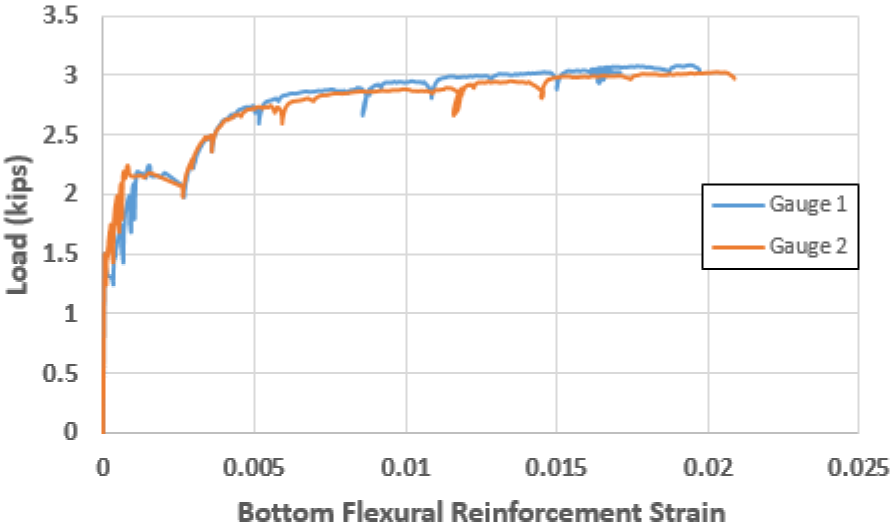

(b)

Figure 3-24. (a). Diagram of Load versus Middle of Bottom Layer Flexural Reinforcements Strain for Wall Specimen 1; (b). Diagram of Load versus Middle of Bottom Layer Flexural Reinforcements Strain for Wall Specimen 2

It is known from the cylinder tests that the compressive strength of concrete for the second wall panel is about 12% higher than that of the first wall panel. However, according to the test results, the maximum loads are almost the same for the two panels. This shows that concrete compressive strength has little effect on the moment capacity of the panels. The reason is that when the compressive stress increases, the compressive block area will be reduced to balance the compressive stress with the tensile stress from the rebar. Since the width of the wall is not changing, the depth of the compressive stress block will decrease, and the level of the resultant concrete compression force will increase. This will increase the moment arm of the tensile force from the tension steel. By doing the calculating, the increase of the compressive block depth will be very small, which limits the impact the panel’s moment strength along weak axis.

CHAPTER 4. FINITE ELEMENT MODEL

4.1 Introduction

Numerical simulations are important to verify with hand calculated results and also to validate with test results. In this study, the numerical simulations are presented by making FE models of walls under lateral load, axial load and four-point load conditions through the commercial software ABAQUS. The FE models take the nonlinear inelastic response of the walls into account, and applies displacement controls to the wall specimens to find the failure stages of the walls under specified load conditions. The mechanism of the failure is due to the crush on any portion of the concrete under compressive stress for most cases, besides that, the steel will break especially if the wall is under weak axis bending when there are not enough flexural reinforcements in the far tension zone. In defining the concrete damage model under ABAQUS, the stress on concrete will decrease slowly as the inelastic strain increases to avoid any convergence problems. In order to find the concrete failure point from ABAQUS results, the load-displacement diagram from ABAQUS output data will be drawn. ACI 318-14 Building Code suggests the maximum concrete usable strain is 0.003, and the failure load of the concrete can be known corresponding to a compressive stress of 0.003. These FE models are essential for predicting the nonlinear responses of the walls, both within the performance-based assessments, and for the improvement of the future designs of wall with openings. Due to the assumptions of the parameters in calculating the strengths of the walls as well as the model through lab testing, the reliability of the results are limited (Chen and Kabeyasawa, 2000). When doing testing, some uncontrolled differences, such as inaccuracy in concrete cover and material properties, could affect the test results a bit as compared to hand calculations and FE modeling. In this chapter, FE modeling will be used for analyses of flexural, pushover and axial loading capacity.

4.2 Details in the Model

4.2.1 Geometry

A total number of three models are made. Each of the two models for doing pushover and axial loading analysis have a footing connected on the bottom while the model used for four point bending analysis does not have a footing. The sizes of the wall and footing are in accordance with the test specimens. The number and sizes of the holes on the wall are following the optimal solutions, which are 7 and 1.315 in., respectively. Three-dimensional solid shape is used to model the wall and footing. The reinforcements are bonded inside the concrete by using embedded region constraint on ABAQUS, wire shape with assigned cross-section area is used to model different sizes of reinforcements. The reinforcement sizes in the models are also the same as the ones in test specimens, which are No. 2 for walls. No. 6 were used for the footing. In ABAQUS, all the reinforcements are under embedded constraint to the wall and bond well to the wall, they are not considered to be pulled out of the concrete, and therefore, the hooks are not necessary to be modeled in the FE model for anchoring purpose. The full models of the wall with footing and without footing are shown in Figure 4-1.

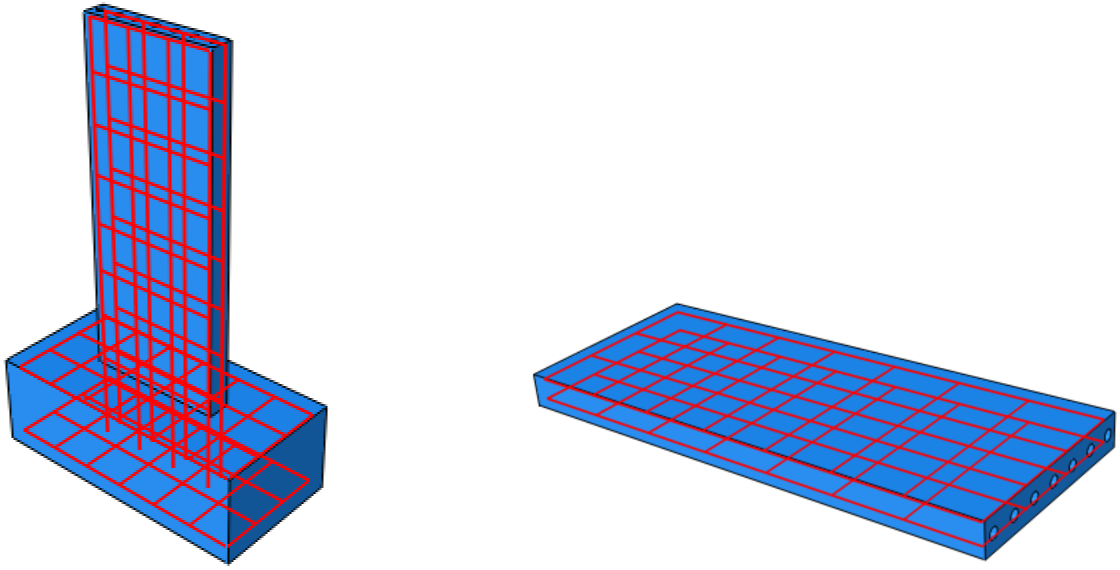

(a) (b)

Figure 4-1. (a). FE Model of Wall with Footing; (b). FE Model of Wall without Footing

In the model, each of the two layers of wall reinforcements and the footing reinforcements are merged, with ¾ in. cover along the width and height of the wall and 1-1/2 in. cover in everywhere in the footing. The reinforced bars are equally spaced along the available lengths, and the center-to-center spacing of the reinforced bars are equal to each other (Figure 4-2).

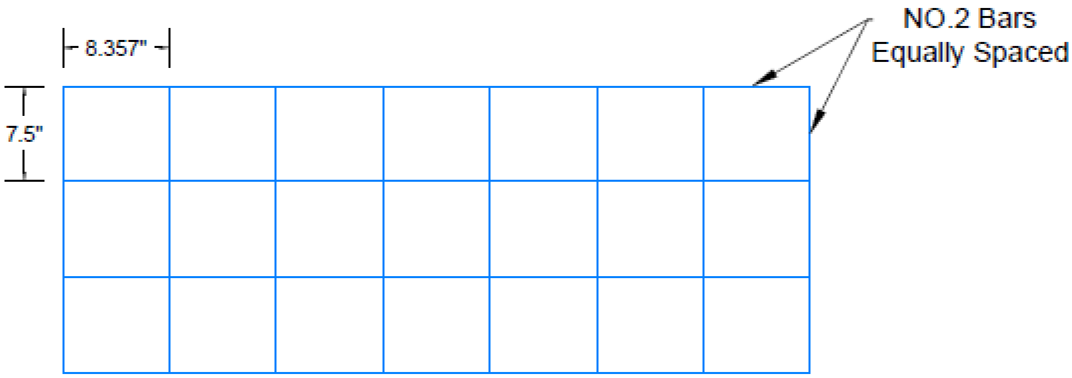

(a)

Figure 4-2. (a). Wall Reinforcements Layout; (b). Footing Reinforcements Layout

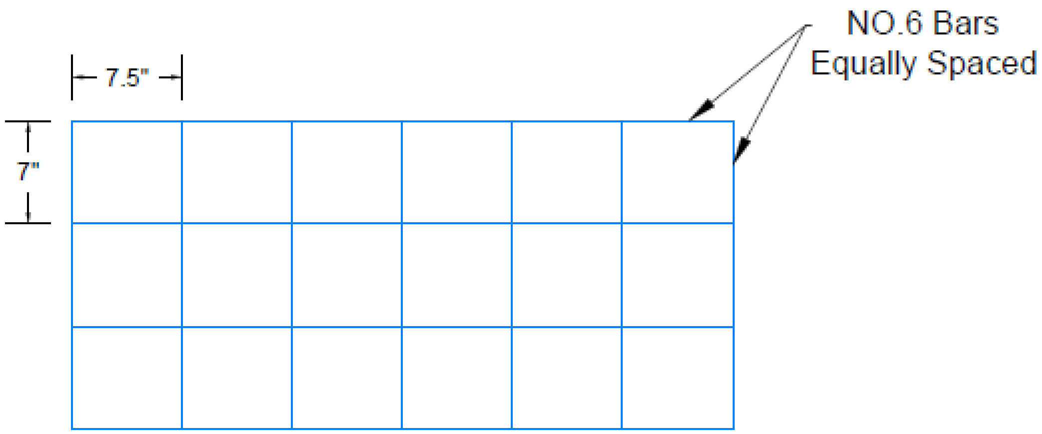

(b)

Figure 4-2. (continued)

The linear hex element with hourglass control and reduced integration C3D8R for 3D solid is used for modeling all the concrete parts. Each of these elements has 8 nodes, and the mesh technique used is to sweep through the bodies. The linear 3D truss with 2 nodes is used for modeling the reinforcements. For the two walls with footings, due to the different geometries of the wall with holes and the footing, the mesh option cannot be executed until the whole model is cut into two parts with a more uniform shape for each part. Therefore, a datum plane is made at the connection between the wall and the footing level and the partition is made by using this datum plane (Figure 4-3). The cut option does not affect either the mesh pattern or the behavior under applied loads.

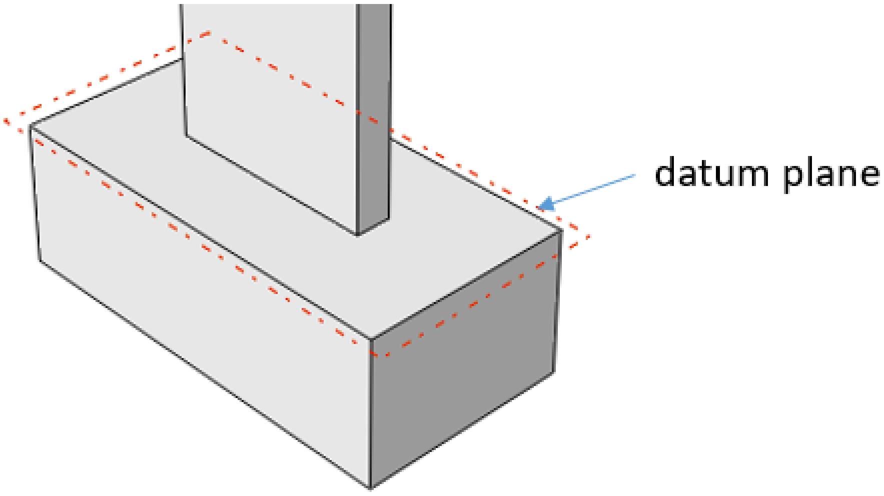

Figure 4-3. Location of Datum Plane and Cutting Level

4.2.2 Material Properties

The ultimate goal of this study is to reach the failure stage of the reinforcement concrete wall system, however, the concrete only remains elastic when it is simply isotropic at the very beginning (Tsau 2009). The steel and concrete will yield before failure happens, bringing both reinforcement and concrete to their plastic stage. Therefore, in the FE model, both elastic and inelastic properties of the concrete and steel components are needed for modeling the walls as expected.

4.2.2.1 Elastic material properties

Typically, elastic material properties are the materials' inherent properties, which include the density, Young's modulus and poisson's ratio. In the model, for concrete material, the density used is 150 lbs/ft^3, which is a typical value for normal-weight concrete. The Young's modulus is based on the compressive strength from cylinder test. According to ACI 318-14 Building Code, the modulus of elasticity for normal-weight concrete can be calculated from the equation $57000\sqrt{f'c}$ psi. Hsu and Hsu indicated that the ACI 318-14 Building Code overestimates the modulus of elasticity for high-strength concrete with compressive strength greater than 6 ksi after 28 days of pouring (Hsu and Hsu 1994). According to the concrete compressive test, the concrete of our test specimen has a strength of 5764 psi, which is considered as normal strength concrete, the modulus of elasticity is calculated following the equation from the ACI 318-14 Building Code, which is 4327 ksi, meanwhile, according to Wight, poisson's ratio for concrete under tension and compression is 0.18 to 0.2 (Wight 2016), and the middle value of 0.19 is used in this FE model. For steel material, the density is used as 490 lbs/ft^3, while the young's modulus is 29000 ksi and the poisson's ratio is 0.3.

4.2.2.2 Inelastic material properties

The nonlinear analysis in the FE models are accomplished by inputting the damaged plasticity parameters and behaviors for concrete, and the plastic behavior for steel. The concrete damaged plasticity model is recommended by ABAQUS because it provides the general capability for modeling concrete which has a brittle property (ABAQUS 6.12 Documentation), and the input of the steel plasticity values describe the behavior of steel after yielding up to is ultimate strength well. The concrete damaged plasticity parameters are shown below:

- Dilation angle: 31 °
- Eccentricity: 0
- Ratio of biaxial strength to uniaxial strength f_{b0}/f_{c0}: 1.16
- Ratio of the second stress invariant on tensile meridian K: 0.667
- Viscosity parameter: 0.0001

Material's plastic behavior occurs at the nonlinear stage, and at this time, if the forces deforming the material have been removed, the material will not completely return to its original shape, and thus the plastic strain exists. The concept of plasticity, combined with the concept of damage, correctly represent the nonlinear behavior of a material (Yu et al. 2010). ABAQUS defines both concrete compression damage and tension damage under the damaged plasticity model, and the method to define the compressive and tensile behavior of concrete is introduced separately.

The relationship between compressive stress and strain of concrete has been defined by many researchers. Among all of them, the one proposed by Hognestad is one of the most commonly used, and is shown in Figure 4-4 (Abavisani et al. 2017). In Hognestad's model, when concrete stress increases from zero to the peak value, the stress-strain relation can be describe as a second-order parabola, with the equation of

$$f_c = f'_c\left[2\frac{\varepsilon_c}{\varepsilon'_c} - \left(\frac{\varepsilon_c}{\varepsilon'_c}\right)^2\right] \tag{14}$$

where f_c is stress of concrete and f'_c is the peak stress of concrete, ε_c and ε'_c are the strains of concrete at f_c and f'_c, respectively. ε'_c can be calculated by using equation

$$\varepsilon'_c = \frac{1.8f'_c}{E_c} \tag{15}$$

where E_c is modulus of elasticity of concrete. After reaching the peak stress, the stress of concrete will decrease but the strain will still increase. Hognestad used linear relationship to describe this decline portion until the stress of concrete drop to 85% of its peak stress. The stress-strain relation is expressed as

$$fc = f'_c\,[1 - 0.15\left(\frac{\varepsilon_c - \varepsilon'_c}{\varepsilon_{cu} - \varepsilon'_c}\right)] \tag{16}$$

where ε_{cu} is ultimate strain and is taken as 0.0038 (Karasin and Gunaslan 2015).

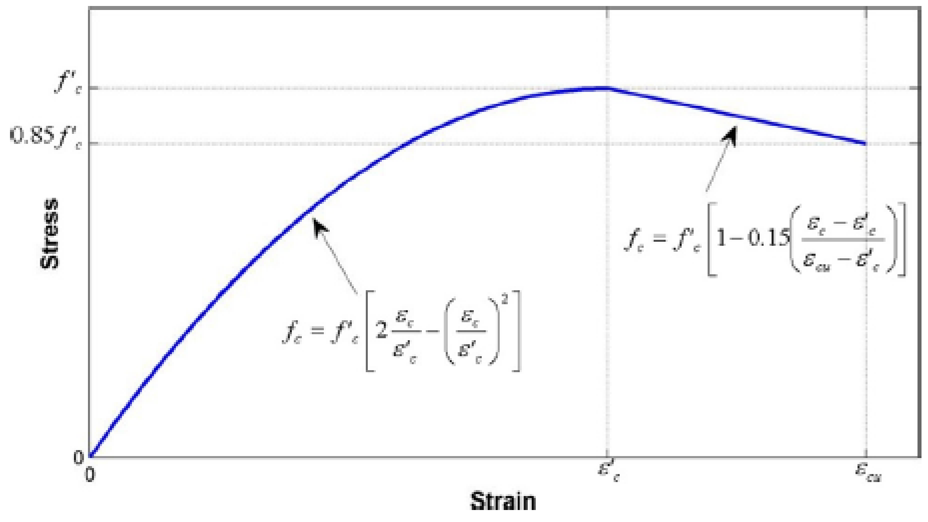

Figure 4-4. Stress-strain relation of concrete in Hognestad's model (Abavisani et al. 2017)

In this study, Hognestad model combines with the assumption from ACI 318-14 Building Code are used to define the concrete compression damage plasticity model in ABAQUS. ACI 318-14 Building Code assumes the stress-strain diagram can be treat as linear when the concrete stress below 45% of its compressive strength, which is 2594 psi. Beyond this point, Hognestad's model is used to define the relationship between stress and inelastic strain in ABAQUS.

According to ABAQUS user's manual, the inelastic strain equals the total strain minus the elastic strain in the plastic stage corresponding to the undamaged material, where the elastic strain equals to the stress of concrete over the concrete's modulus of elasticity (ABAQUS 6.12 Manual). This has been illustrated in Figure 4-5 below, and based on this relationship, the compressive behavior of concrete under damage plasticity model can be calculated.

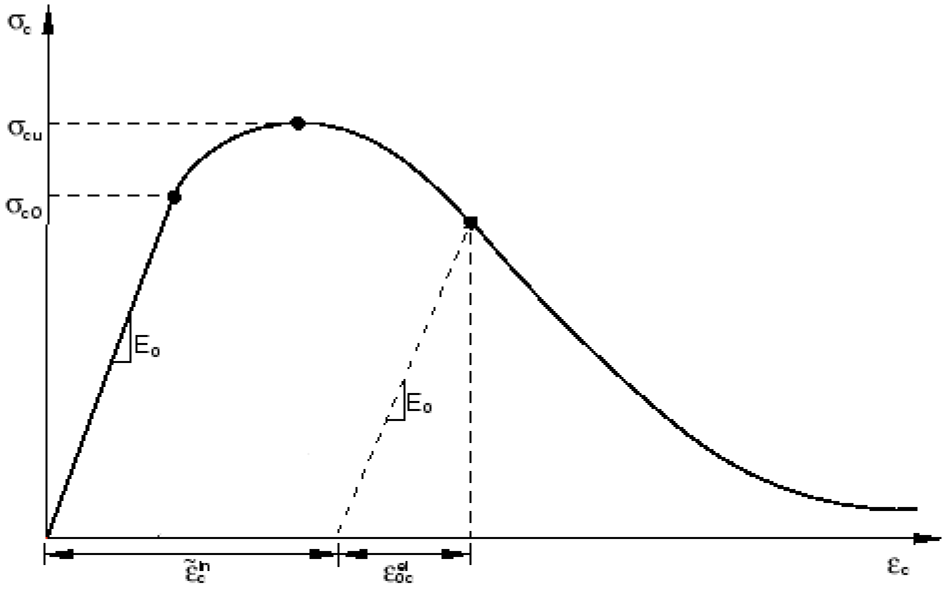

Figure 4-5. Concrete Compressive Elastic and Inelastic Strain (ABAQUS 6.12 Manual)

The concrete tension damage is another model that was defined in ABAQUS. This study will use the model that developed by Wahalathantri et al. (2011) combined with ACI 318-14 Building Code requirements to define the input parameters under the concrete tension damage plasticity model in ABAQUS. According to ACI 318-14 building Code, the average splitting tensile strength of normal weight concrete can be calculated from $6.7\sqrt{f'c}$, and by plugging the concrete compressive strength 5764 psi into the equation, the concrete cracking stress is calculated as 508.66 psi. The corresponding cracking strain can be calculated from cracking stress over the concrete's modulus of elasticity, which gives 1.175×10^{-4}. In Wahalathantri et al.'s tension stiffening model, the concrete stress-strain relation is linear until the maximum tensile stress happens, and then the concrete stress will drop with the continuous increasing of its strain. The concrete stress will drop to 0.77 of its tensile strength with a strain of 1.25 times its cracking strain, and then drop at a slower speed until 0.45 of its tensile strength with a strain of 4 times its cracking strain, and its stress will drop even slower until 0.1 of its tensile strength with a strain of 8.7 times its cracking strain. The diagram that describes Wahalathantri et al.'s model is shown in Figure 4-6 below. With the calculated concrete splitting tensile strength corresponding its cracking strain, the tension behavior of concrete under damage plasticity model can be calculated.

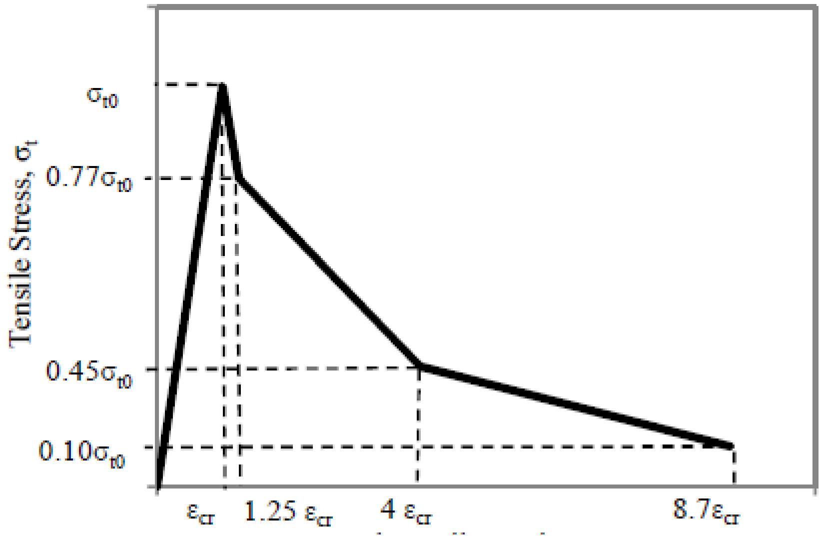

Figure 4-6. Wahalathantri et al.'s Concrete Tension Stiffening Model (Wahalathantri et al. 2011)

Following the same method as one calculates the inelastic strain of concrete under compression, the strain for concrete under tension can be calculated as well. The illustration of the concrete cracking strain is defined by ABAQUS user's manual, and is shown in Figure 4-7 below (ABAQUS 6.12 Manual). With the calculated concrete splitting tensile strength corresponding to its cracking strain, the other values that describe the concrete's tension behavior under damage plasticity model can be calculated accordingly.

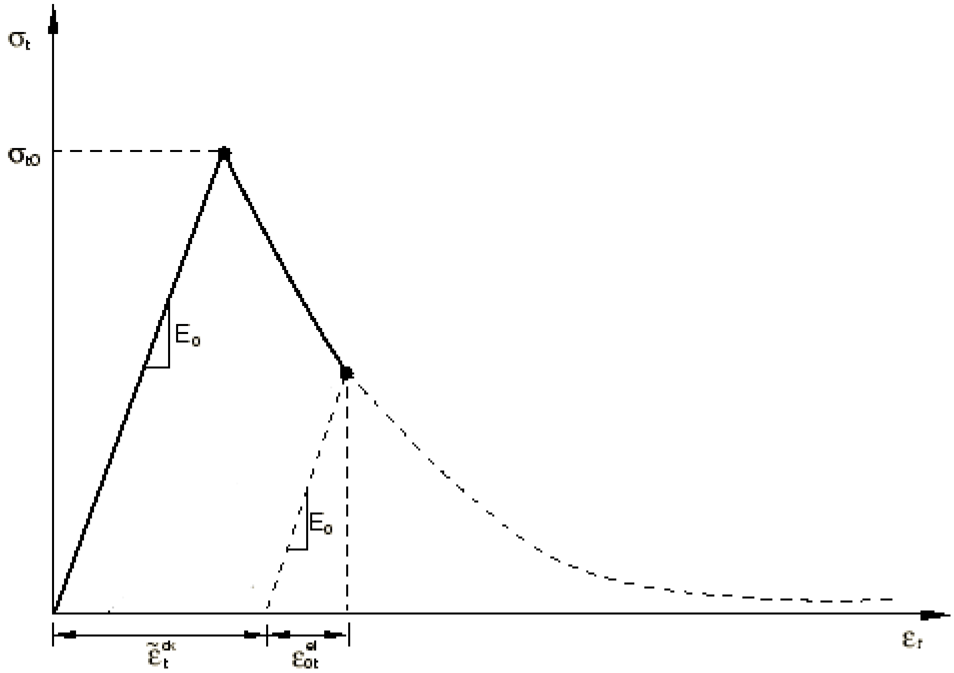

Figure 4-7. Concrete Tensile Elastic and Inelastic Strain (ABAQUS 6.12 Manual)

The damage parameter corresponding concrete compression and tension damage also need to be defined in ABAQUS, and the parameter is based on the definition of concrete plastic degradation, which is assumed to be happened in the softening range when the stress of concrete already passed the peak value and is decreasing. Lubliner et al. defined the concrete damage parameter is calculated by using the following equation:

$$d = 1 - \frac{\sigma}{\sigma_{peak}} \tag{17}$$

where σ and σ_{peak} are stress of concrete and peak stresses of concrete under compression or tension (Lubiner et al. 1988).

The data of concrete compression and tension damage plasticity models that used in the ABAQUS model for this study based on the calculation methods mentioned above is shown in Table 4-1 below.

Table 4-1. Concrete Compression and Tension Damage Plasticity Model Data

Concrete Compression Behavior		**Concrete Compression Damage**	
Yield Stress (psi)	**Inelastic Strain**	**Damage Parameter**	**Inelastic Strain**
2593.7	0	0	0
2903.2	3.75971E-5	0	3.75971E-5
3302.5	6.7635E-5	0	6.7635E-5
3701.6	0.000108044	0	0.000108044
4025.9	0.000150687	0	0.000150687
4300.5	0.00019571	0	0.00019571
4603.8	0.000258081	0	0.000258081
4812.6	0.000311431	0	0.000311431
5024.1	0.000377646	0	0.000377646
5212.7	0.000451603	0	0.000451603
5402.8	0.000549033	0	0.000549033
5500.6	0.000614123	0	0.000614123
5600.4	0.00069975	0	0.00069975
5700.2	0.000828608	0	0.000828608
5764	0.001065331	0	0.001065331
5600.1	0.001368689	0.028379487	0.001368689
5205.8	0.002099477	0.09679076	0.002099477
4899.1	0.002667877	0.15	0.002667877
Concrete Tension Behavior		**Concrete Tension Damage**	
Yield Stress (psi)	**Cracking Strain**	**Damage Parameter**	**Cracking Strain**
508.6562162	0	0	0
391.6652865	5.64211E-5	0.23	5.64211E-5
228.8952973	0.000417281	0.55	0.000417281
50.86562162	0.001010877	0.9	0.001010877

Besides the concrete, No.2 rebar is used for the reinforcements embedded inside the concrete wall. Similar to the concrete model, the steel plasticity model will be defined by inputting the relationship between the yield stress and plastic strain, however, the steel is assumed to be not damaged in the model, therefore, no damage parameters are defined for the steel material. The steel plasticity data that obtained from the average values of the four uniaxial tensile tests mentioned in Chapter 3.2 are used in the ABAQUS model.

Based on the testing results, the plastic model of the steel material in ABAQUS can be determined. Similar to the concrete plasticity model, the plastic strain of steel equals the total strain minus elastic strain, where elastic strain can be calculated from the stress of steel over its modulus of elasticity. With the input yield starts at the beginning of nonlinear stage where plastic strain appears, the data of steel plastic model that used in the ABAQUS model for this study is shown in Table 4-2 below.

Table 4-2. Steel Tension Plastic Model Data

Steel Tension Behavior	
Yield Stress (psi)	**Plastic Strain**
84375	0
88621.9	0.000743345
90749	0.000904962
92344.2	0.001098475
95167.4	0.001560527
97098.5	0.002057003
98487.1	0.002583299
100210.3	0.003399585
101413.6	0.00417819
102792.9	0.005238756
103989.5	0.006637832
105164.7	0.008499128
106068	0.01103986
106863.7	0.013954479
107512.1	0.018957718
107868.2	0.021825448
108160.6	0.029292428
108264.7	0.030867834
108559.5	0.031905767
108350.4	0.034374649

These stress/strain curves and damage curves define the concrete and steel’s plasticity in all the models.

4.2.3 Mesh Convergence Study

In order to obtain more accurate results with an appropriate mesh size, a mesh convergence study has been conducted. In the finite element model, the smaller mesh size used, the longer the run time, but the results will become more accurate. Therefore, the idea of a mesh convergence study is to keep the load condition consistent, while decreasing the mesh size of the model until the results converge to a solution. In the wall model, the number of elements along the edge of each of the holes in the wall and the global mesh size of the wall were defined as the two parameters considered to be variables in the convergence study. There are two reasons for selecting these two parameters. First, ABAQUS defines circular shapes as the connection of multiple straight lines. For example, if there are four elements along edge of a hole, then the geometry shape encloses by four lines is a square instead of a circle; the more elements along edge of the hole, the more accurate the shape. Secondly, the change of number of elements along edges of the holes will greatly impact the shape of each element on top and bottom surfaces of the wall, affecting both the total number of elements and the accuracy of the results.

In order to use uniform mesh size for all the three models, a mesh convergence study was done for each model and the smallest mesh size was used in conducting the finite element analysis. In order to reduce the number of elements, an edge mesh size was been assigned along the height of the wall due to the longer wall height than the width. The ratio of the height of each element to the width is the same as the wall height to width ratio. A constant 2-in mesh size was assigned to the footing because the footing is not the object of this study. For all the models, the mesh size starts as two inches and the number of elements along the edge of holes starts at four. The number of elements along holes will increase by two divisions each time and the global mesh size will decrease at a ratio equivalent to the hole edge elements as compared to the original hole edge element.

4.2.3.1 Four-point bending model

For the four-point bending model, 10-psi pressures are applied to the two third-stripes on the front surfaces of the wall (Figure 4-8), and the maximum vertical displacements at the mid-span of the wall is recorded with respect to total number of elements after using different mesh sizes. The results and plot of number of elements versus displacements are shown in Table 4-3 and Figure 4-9, respectively. The plot indicates that the displacement almost converges to one value when the total number of elements reaches 17884, corresponding to 12 elements along edge of the holes and a global mesh size of 0.667 in. To be more conservative, the point after this first converged point, corresponding to 14 elements along the edges of holes and a global mesh size of 0.571 inch, is selected for this model.

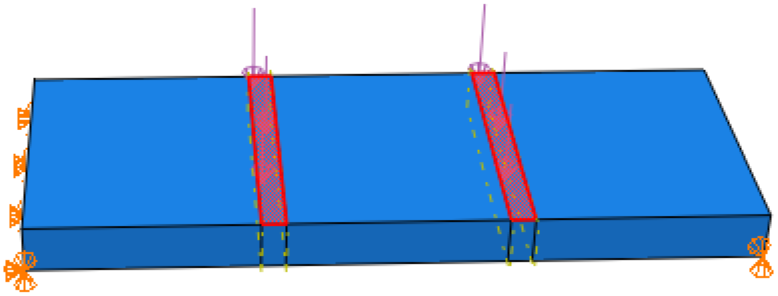

Figure 4-8. Location of Loading for Bending Model Convergence Study

Table 4-3. Four-point Bending Model Mesh Convergence Study

Number of Elements Along Edge of Holes	Global Mesh Size (in)	Total Number of Elements	Maximum Vertical Displacement (in)
4	2	1106	0.008102
6	1.333	2760	0.007827
8	1	5460	0.007774
10	0.8	11296	0.007677
12	0.667	17884	0.007651
14	0.571	26080	0.007647
16	0.5	42240	0.007637
18	0.444	55674	0.007633
20	0.4	80700	0.007628

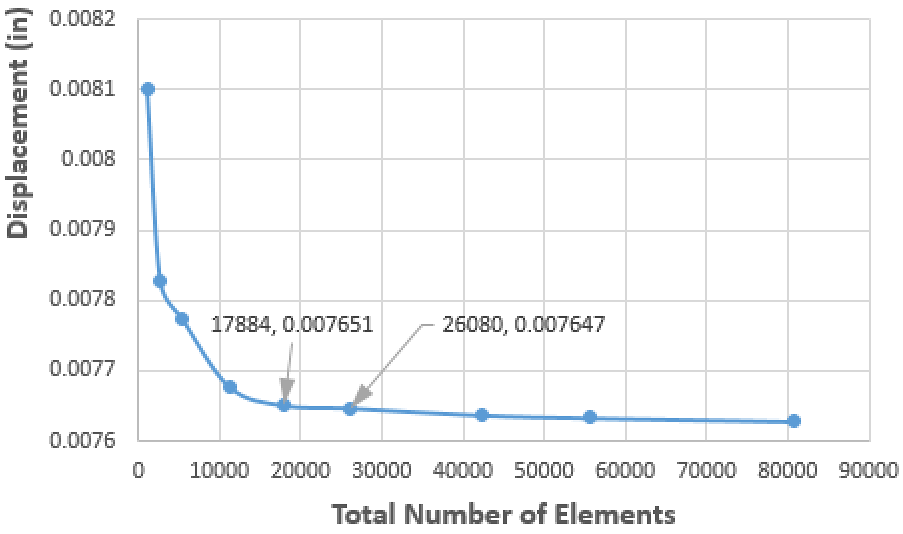

Figure 4-9. Number of Elements versus Displacement Plot for Bending Model

4.2.3.2 Axial loading model

For the axial loading model, a 1000-psi pressure is applied to top surface of the wall (Figure 4-10), and the maximum vertical displacements at pressure surface are recorded. Similarly, the results and plots are shown in Table 4.4 and Figure 4-11, and the converged point for axial loading model is selected as 29,240 elements, which corresponding to 12 elements along edge of the holes and a global mesh size of 0.667 in.

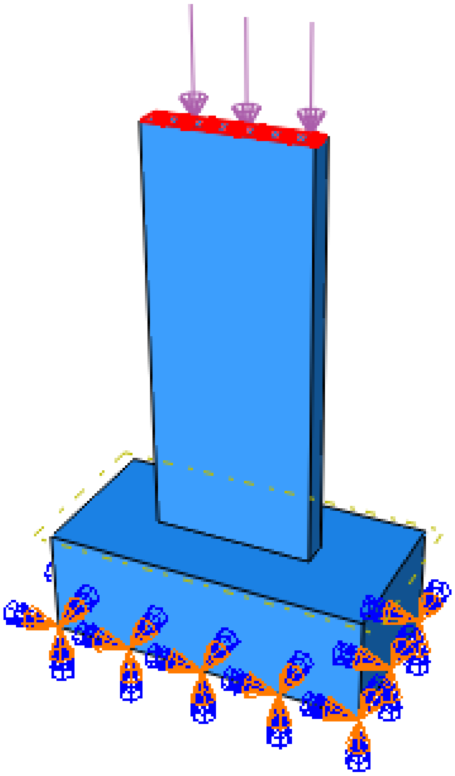

Figure 4-10. Location of Loading for Axial Loading Model Convergence Study

Table 4-4. Axial Loading Model Mesh Convergence Study

Number of Elements Along Edge of Holes	Global Mesh Size (in)	Total Number of Elements	Maximum Vertical Displacement (in)
4	2	4196	0.01686
6	1.333	7032	0.01661
8	1	11080	0.01673
10	0.8	19012	0.01655
12	0.667	29240	0.01656
14	0.571	41538	0.01651
16	0.5	57752	0.01652
18	0.444	78892	0.0165
20	0.4	105096	0.01652

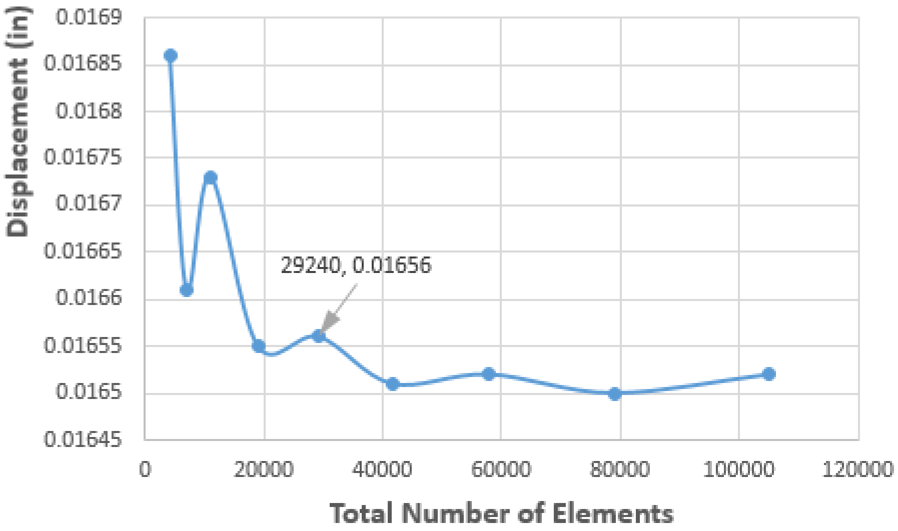

Figure 4-11. Number of Element versus Displacement Plot for Axial Loading Model

4.2.3.3 Pushover model

For the pushover model, a 50-psi pressure is applied to a 4” x 5” area of the side surface of the wall (Figure 4-12), and the maximum horizontal displacements at top surface of the wall are recorded. The results and plots are shown in Table 4-5 and Figure 4-13, and the converged point for axial loading model is selected as 40881 elements, which corresponding to 14 elements along edge of the holes and a global mesh size of 0.571 in.

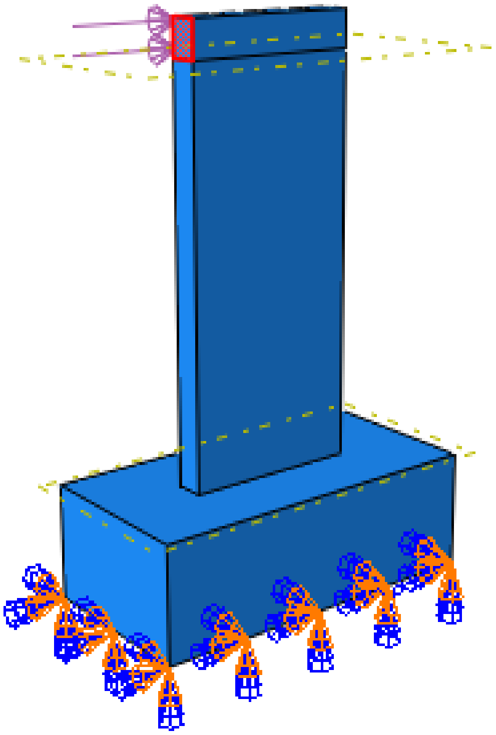

Figure 4-12. Location of Loading for Pushover Model Convergence Study

Table 4-5. Pushover Model Mesh Convergence Study

Number of Elements Along Edge of Holes	Global Mesh Size (in)	Total Number of Elements	Maximum Vertical Displacement (in)
4	2	4196	0.005544
6	1.333	7168	0.005607
8	1	11080	0.005636
10	0.8	19350	0.005664
12	0.667	29240	0.005682
14	0.571	40881	0.005687
16	0.5	57752	0.005687
18	0.444	79958	0.005696
20	0.4	105096	0.005697

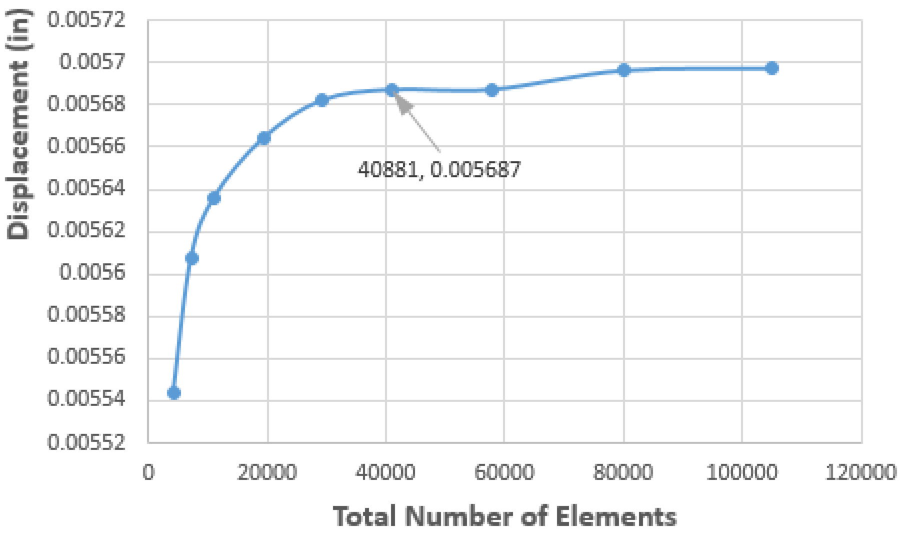

Figure 4-13. Number of Elements versus Displacement Plot for Pushover Model

Among the converged mesh sizes selected in the three models, the smallest mesh size would be 14 elements along holes with a global mesh size of 0.571 in. This mesh size is used for all the finite element models in this study. To be clarified, the final mesh size of the wall with footings are shown in Figure 4-14.

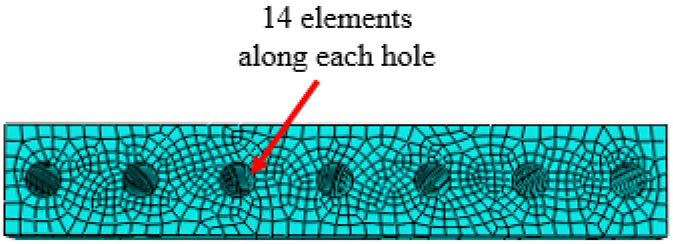

(a)

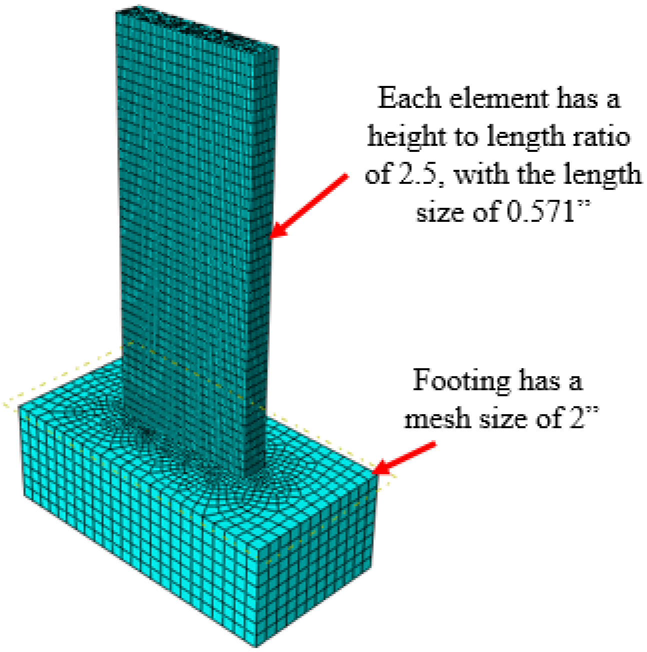

(b)

Figure 4-14. (a). Mesh Element Size along Each Hole; (b). Mesh Element Size of the Wall and the Footing

4.3 Boundary Conditions in the Model and Results from the Model

Walls in the FE models with different modeling purposes will have different load conditions and boundary conditions. These conditions are described separately for each model in this subchapter. Displacement control method is used in all the FE models, which means the walls in different models will be subjected to displacements at different intervals that can cause failure. The different load capacities of the walls can be obtained from the output load-displacement data, and these results will be compared with the hand calculations as well as the lab testing data in order to validate the model.

4.3.1 Four-point Bending Model

In the four-point bending model, the wall is laid down and simply supported with pin support on the left end and roller support on the right end. In ABAQUS, these two boundary conditions are defined by restraining the displacement along the two edges in different directions. Two 3-inch displacements are applied along the two third line strips in the middle (Figure 4-15). The wall will have a pure bending zone in between these two displacement lines where no shear exists. The most critical section is the middle of the wall, where the maximum stress and deformation happen.

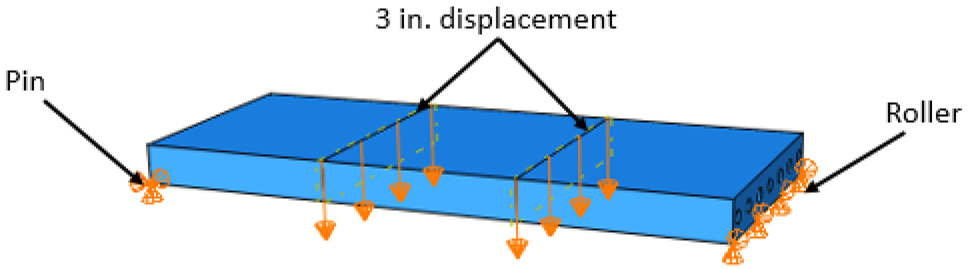

Figure 4-15. Loading Conditions and Boundary Conditions in Four-point Bending Model

The diagram of load (at either strip) versus the displacements in the middle section, left and right load strips from FE model and lab testing are shown in Figure 4-16. Based on the test data, the maximum strains happen on the middle part of the bottom layer flexural reinforcements for test specimen 1 and 2. These strain values are shown in Table 4-6 below. The average value is taken as the strain that caused the fracture of the rebar in the test.

Table 4-6. Maximum Strain Detected on the Middle Part of Bottom Layer Flexural Reinforcements from Test Specimens and the Average Value

Wall Specimen 1		Wall Specimen 2	
Maximum Strain 1	0.016513	Maximum Strain 1	0.020871
Maximum Strain 2	0.024612	Maximum Strain 2	0.023122
Average: 0.02128			

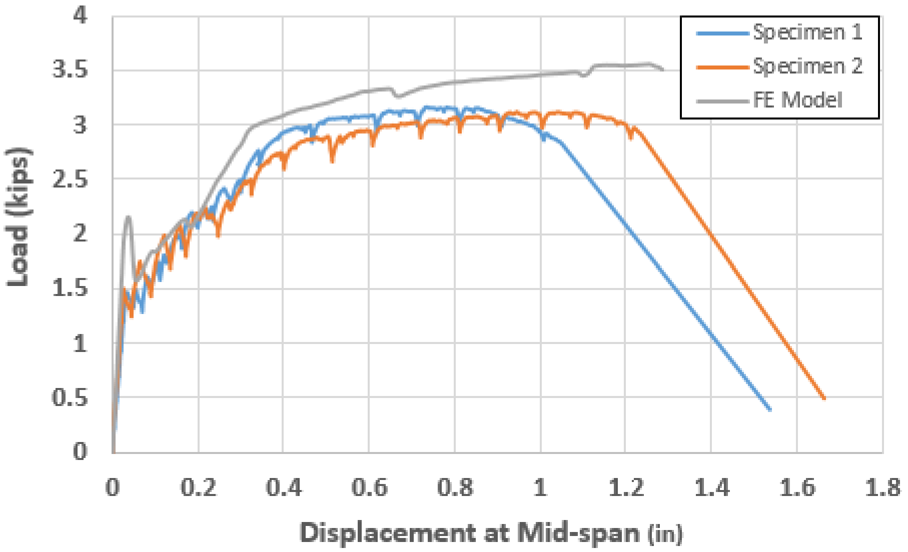

(a)

Figure 4-16. (a). Diagram of Load versus Displacement at Mid-span; (b). Diagram of Load versus Displacement at the left load strip; (c). Diagram of Load versus Displacement at the right load strip

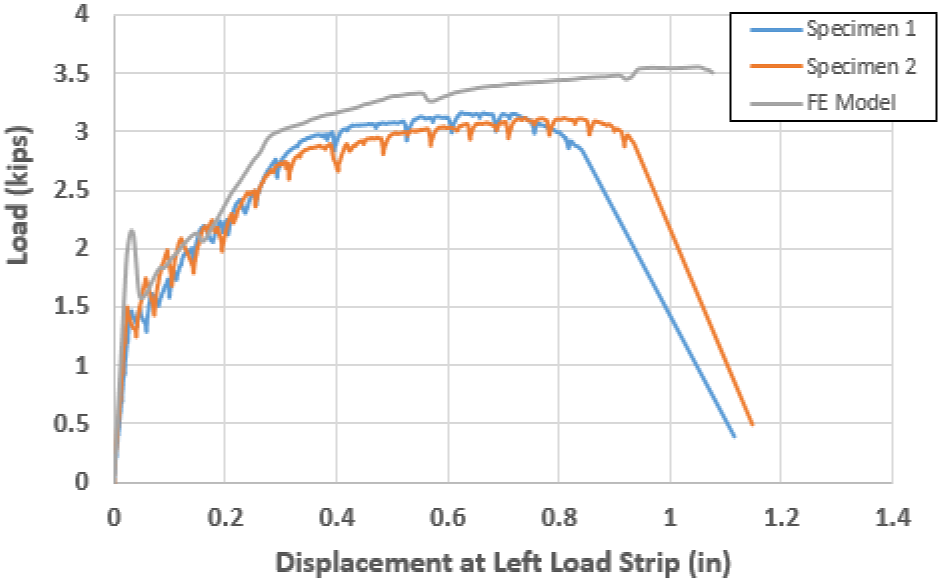

(b)

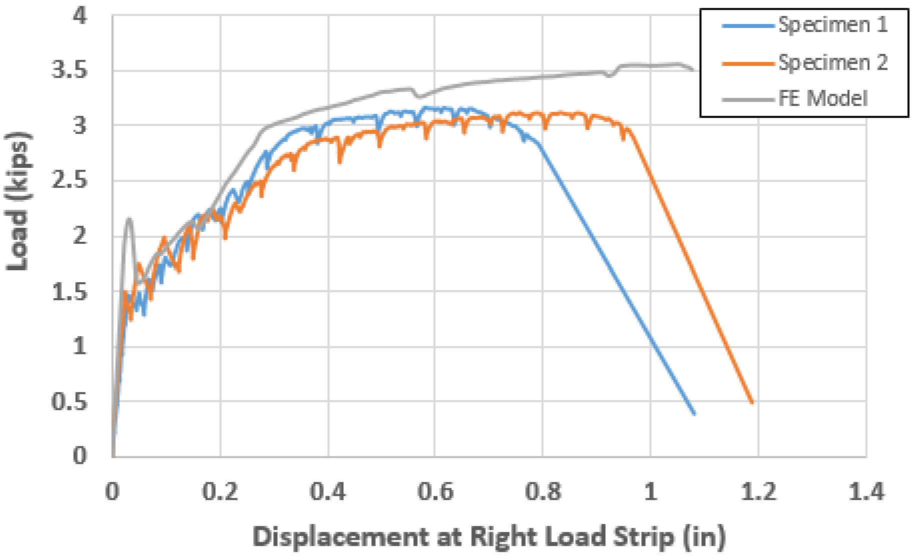

(c)

Figure 4-16. (continued)

By comparing the FE model results with the testing results, one can see that before the steel yields, there is good correlation between the FE model and testing results. After the steel yields, the testing result curve reaches the peak load value and almost remains constant as the displacement increases until failure occurs. However, the FE model curve tends to keep increasing slowly as the displacement increases. This is because in defining the steel plasticity model in ABAQUS, there is no damage parameter. Therefore, the steel acts more like an elastic material that can be stretched without fracture, indicating that rebar fracture is not a failure mode that will occur in the FE model. Additionally in defining the material properties of steel and concrete, assumptions were made. For example, the dilation angle is an estimated value, and the equation used in calculating the concrete's modulus of elasticity may not be exactly the same as the real value. These uncertainties could cause the difference between the model results and the testing results.

According to hand calculation based on ACI 318-14 Building Code requirements, the weak axis moment capacity of the wall is 5.637 kip-ft. From the peak load values obtained from lab testing and FE modeling, the moment applied can be achieved by multiplying the load value to the distance from one of the supports to the closed load location. The comparison of the results from lab testing, FE model and hand calculation are shown in Table 4-7 below. Results show that the hand calculation results is about 3.5% lower than FE model and 7.5% higher than testing results. This could because of the material properties; for example, the steel material data is based on the four tested samples, however, the reinforcements for the wall specimen might have difference from these tested steel samples. Also, in hand calculations, the ultimate concrete compressive strain that used is 0.003; for the wall specimen, the value might be slightly different. Overall, the results are fairly similar.

Table 4-7. Comparison of Weak Axis Moment Strength between Lab Testing, FE Model and Hand Calculation

	Specimen 1 Test Result	Specimen 2 Test Result	FE Model Result	Calculation Result
Weak Axis Moment Strength (k*ft)	5.273	5.201	5.845	5.637

4.3.2 Axial Loading Model

In the axial loading model, the wall is bonded with the footing, and the boundary condition fixes the bottom surface of the footing. A 2-inch downward displacement is applied to the top surface of the wall, providing a compressive force to the wall (Figure 4-17). As mentioned in chapter 2.3.1, because the height to thickness ratio of the wall is smaller than 28 for concentrically load condition or 16 for eccentrically load case, it is assumed that there is no buckling failure on the wall under this axial load. This is also verified in the FE model.

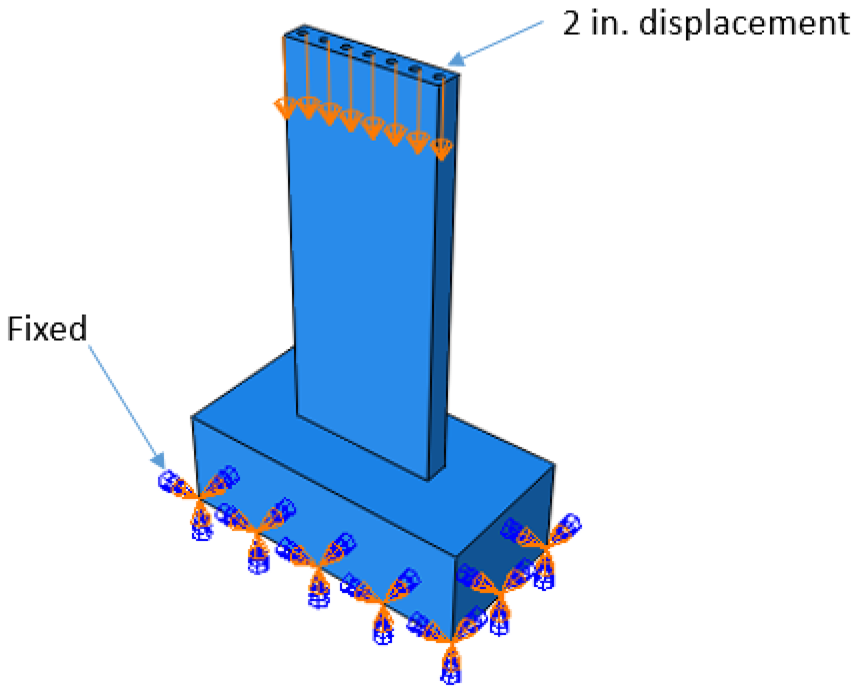

Figure 4-17. Loading Conditions and Boundary Conditions in Axial Loading Model

In verifying the axial load strength of the wall with the optimized TLWD situation, which corresponding to seven 1.315-inch diameter holes in the wall, the load-displacement relation corresponding the top surface of the wall is shown in Figure 4-18. In the plot, the displacement is the one that been applied to the top surface of the wall, and the load represents the magnitude of the force added to the wall when the corresponding displacement occurs. The peak load gives the failure load of the wall under axial loading. According to ABAQUS, the axial load strength of the wall with optimized TLWD situation is 333.24 kips. The hand calculation result based on ACI 318-14 Building Code is 316.31 kips, which has a 5% difference from the FE model result.

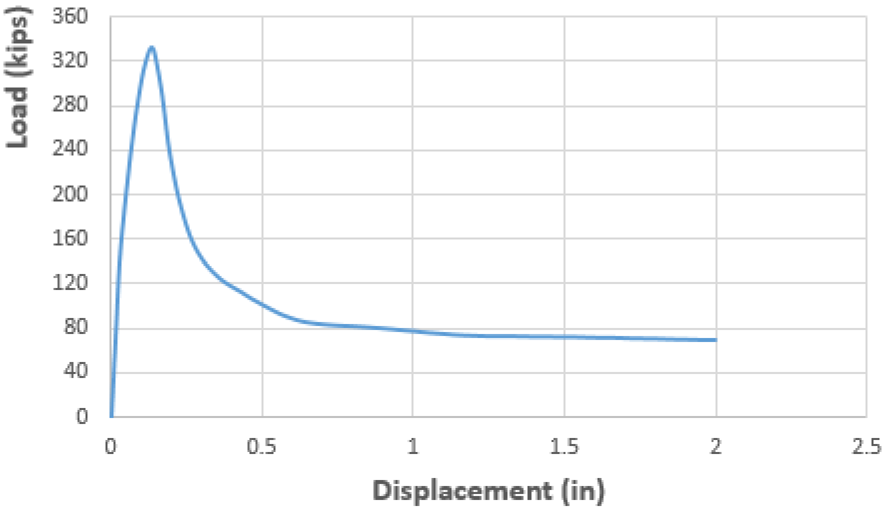

Figure 4-18. Load-displacement Diagram of the Wall with Optimized TLWD Configuration under Axial Load

In order to enhance the reliability of the results, a parametric study is conducted by comparing FE model with hand calculations for different opening configurations. In the parametric study, two numbers of holes are selected for each of the hole size, and a total number of seven opening configurations besides the optimized case have been ran in

ABAQUS, and the axial load strength of the wall can be referred to the peak load value that happen on the wall. Beyond the peak load, the wall fails from the axial load and the capacity drops immediately. Table 4-8 shows the comparison of the hand calculation results and the FE model results, and Figure 4-19 shows the load-displacement curves of the wall from the opening configurations other than the optimized case. It is known from the optimized TLWD case that the wall will fail with 1-in displacement, so the curves stop at 1-inch displacement in order to save time.

Table 4-8. Comparison of Hand Calculation Results and FE Model Results for the Axial Load Capacity of the Wall

	FE Model Results (kips)	Calculation Results (kips)	Difference
2 – 0.84” dia.	379.91	344.86	9%
14 – 0.84” dia.	350.05	322.25	8%
6 – 1.05” dia.	350.84	330.97	6%
10 – 1.05” dia.	340.39	319.19	6%
8 – 1.315” dia.	329.43	311.69	5%
4 – 1.66” dia.	342.97	319.2	7%
9 – 1.66” dia.	301.71	282.41	6%

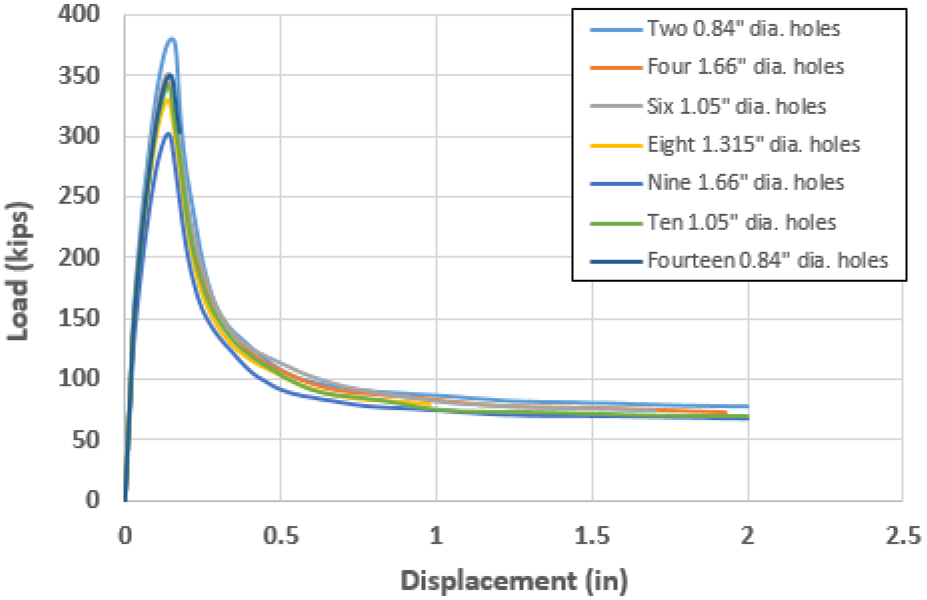

Figure 4-19. Parametric Study of the Axial Loading Capacity of the Wall with Different Opening Configurations

According to Table 4-8, it can be seen that from hand calculation and FE model results, the openings somewhat affect the axial loading capacity, with an 18% strength reduction between the largest and smallest values. In fact, the axial strength of the wall greatly impacted by the surface area of the top of the wall, and the area reduction of the top surface of the wall is proportional to the reduction of the axial load strength of the wall. This is because with the same concrete compressive stress, the load capacity of the wall will be larger if there is a larger surface area that can take the stress.

On the other hand, by comparing the hand calculation results to the FE model results, the FE model results are 5-10% greater than the hand calculation results for all the opening configurations. Several reasons could cause this happens. First, the hand calculation method from ACI 318-14 Building Code is conservative because for designing a structure, it is always better to overdesign than underdesign to against safety threats such as the natural disasters.

Therefore, the hand calculated capacity is lower than the wall's actual strength so that the designed can follow the design limit properly. Second, the FE model does not consider any buckling and internal concrete crush issues, the wall might fails due to the possion's ratio of the concrete, the concrete expand too much in the horizontal direction than in the vertical direction, this can result in a higher failure load.

4.3.3 Pushover Model

In the pushover model, same as the axial loading model, the wall is bonded with the footing and the bottom surface of the footing is fixed. There are two purpose of the pushover model, first is to verify the in-plane shear strength, and second is to verify the strong axis moment strength of the wall. For exploring the in-plane shear strength, more longitudinal reinforcements are added inside the wall, and for exploring the strong axis moment strength, the reinforcements are the same as the original design. A 3-inch lateral displacement is applied to the top surface of the wall to provide the pushover force to the wall for both of the two models (Figure 4-20).

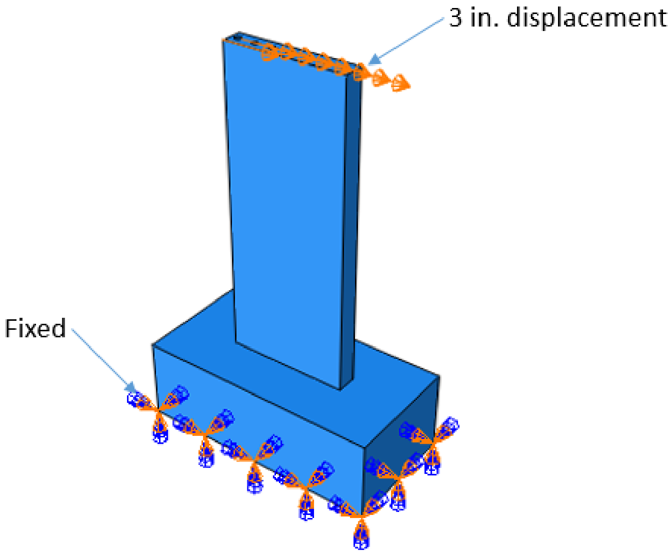

Figure 4-20. Loading Conditions and Boundary Conditions in Pushover Model

In order to verify the in-plane shear strength of the wall, shear failure is expected to be govern on the wall, therefore, more flexural reinforcements are added in the model to prevent the wall fail from flexure. In this model, 40 longitudinal reinforcements are used for each layer, which compose a ratio of 4.3%. The wall with the optimized TLWD situation, which corresponding to seven 1.315-inch diameter holes, is used in the model. The diagram of load versus the displacement on top surface of the wall is shown in Figure 4-21. Similar to the axial loading model, the peak load gives the failure load of the wall with added flexural reinforcements under pushover load. According to ABAQUS, the in-plane shear strength of the wall with optimized TLWD situation is 14.82 kips, and the hand calculation result based on ACI 318-14 Building Code is 18.27 kips. The hand calculation result shows a 23% higher than the FE model result.

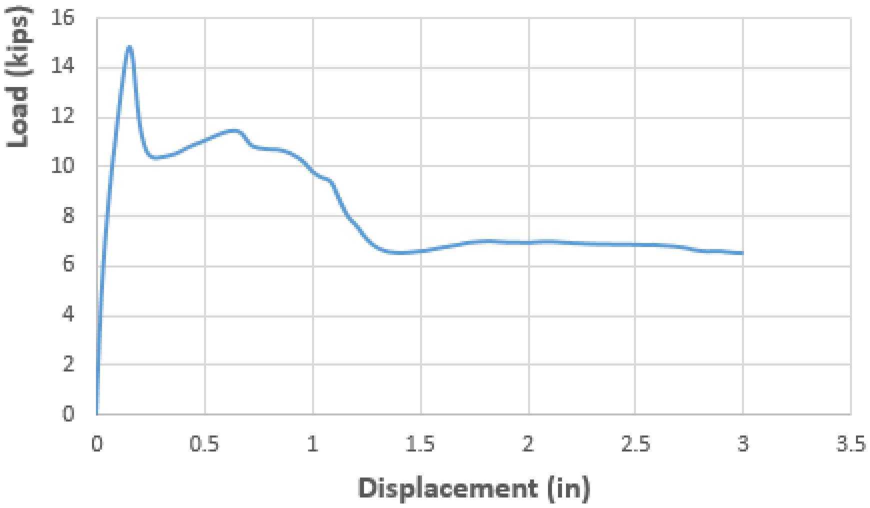

Figure 4-21. Load-displacement Diagram of the Wall with Optimized TLWD Configuration under Pushover Load with Added Longitudinal Reinforcement

Same as the axial loading model, a parametric study has been conducted to compare verify with the hand calculation results. The shear strength of the wall can also be obtained by looking at the peak load value on the wall from the load-displacement diagram. After the peak value, the wall fails from the shear force, and once shear crack happens, the load capacity of the wall drops suddenly until it drops slower at a lower capacity. Table 4-9 shows the comparison of the hand calculation results and the FE model results, and Figure 4-22 shows the load-displacement curves of the wall from the opening configurations other than the optimized case. The curves stop at 1-in displacement to save time.

Table 4-9. Comparison of Hand Calculation Results and FE Model Results for the Shear Capacity of the Wall

	FE Model Results (kips)	Calculation Results (kips)	Difference
2 – 0.84” dia.	19.27	19	1%
14 – 0.84” dia.	16.49	18.44	12%
6 – 1.05” dia.	16.15	18.63	15%
10 – 1.05” dia.	15.69	18.34	17%
8 – 1.315” dia.	14.75	18.21	24%
4 – 1.66” dia.	13.69	18.34	34%
9 – 1.66” dia.	12.99	17.43	34%

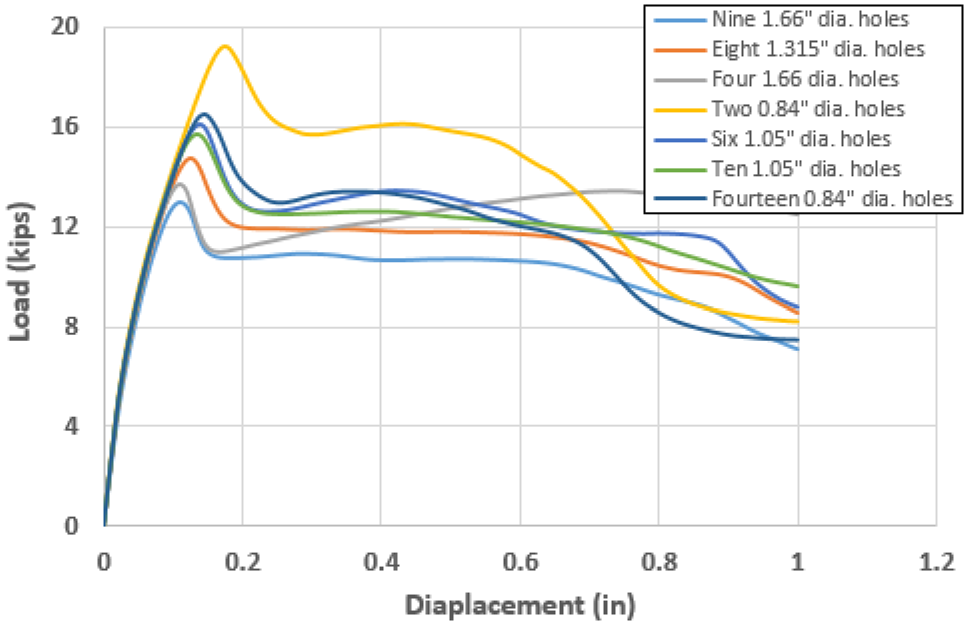

Figure 4-22. Parametric Study of the Shear Capacity of the Wall with Different Opening Configurations

According to the data from table, the differences between the FE model results and the hand calculations are small when there are few and small holes in the wall, however, as the hole sizes get larger and hole number gets more, the difference tends to increase, and the greatest difference happens at the largest hole size but fewest hole number. This shows that the hand calculation method developed in chapter 2 for calculating shear strength overestimates the shear capacity of the wall with large size openings. The larger size of the holes exist in the wall, will affect the stiffness of the wall system more, and the change of the stiffness might have a significant impact on the shear strength of the wall. This could result in that even though the number of holes are few, the large hole diameter will greatly affect the shear strength of the wall. However, in the hand calculation, only the reduced area within the effective depth region has been considered in calculating the wall’s shear strength, this can result in a higher estimate shear capacity of the wall with openings, especially with large diameter openings because of the weakness of the critical section on the wall around the holes.

The second purpose of the pushover model is to verify the strong axis moment strength of the wall with the optimized TLWD situation. The load-displacement relation corresponding to the top surface of the wall is shown in Figure 4-24. According to the output results from ABAQUS, the compressive strain of the wall reach 0.003 at the bottom corner of the wall, which is indicated in Figure 4-23 at the step time of 0.1942. This means that 19.42% of the 3-inch displacement is applied to the top of the wall, and the wall is crush at this stage. According to ABAQUS, the load acting on top of the wall when the concrete compressive strain reaches 0.003 is 5.347 kips. With a multiplication of the wall height of 5 ft, the strong axis moment strength of the wall with optimized TLWD situation is 26.735 kip-ft. The hand calculation result based on ACI 318-14 Building Code is 22.143 kip-ft, which is 17% lower than the FE model results.

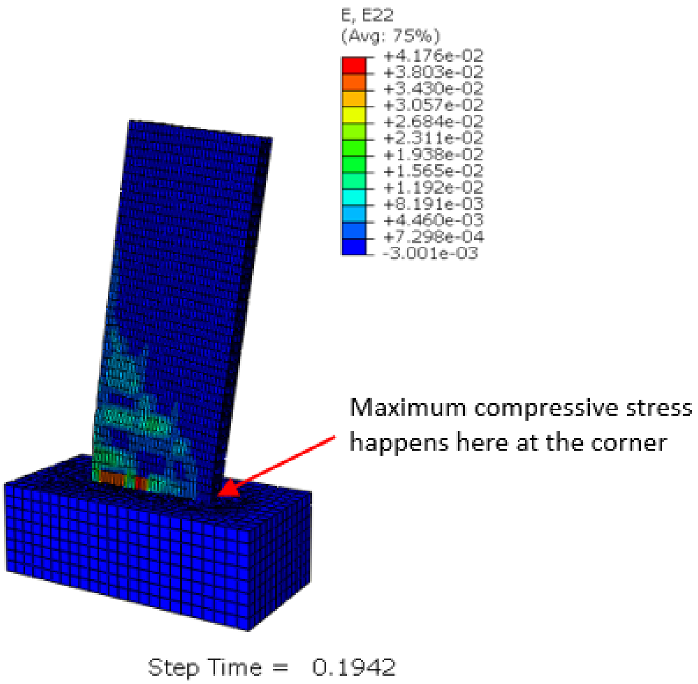

Figure 4-23. Strain on the Wall when the Maximum Compressive Stress Reaches 0.003

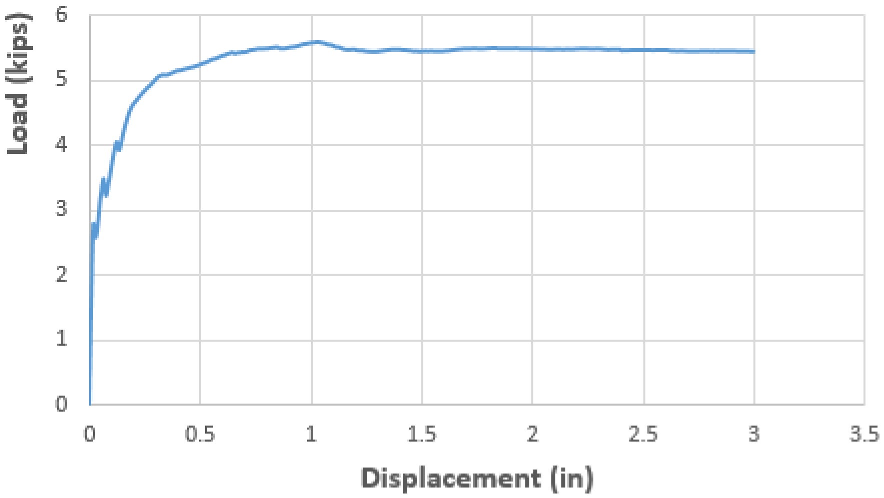

Figure 4-24. Load-displacement Diagram of the Wall with Optimized TLWD Configuration under Pushover Load

Similarly, a parametric study has been conducted for verification purpose. Based on the assumption that the wall crushes at the corner when the compressive strain reaches 0.003, the failure load of the wall can be determined from the load-displacement diagram by looking at the magnitude of the load when the strain reaches this ultimate value. Table 4-10 shows the comparison of the hand calculation results and the FE model results, and Figure 4-25 shows the load-displacement curves of the wall from the opening configurations other than the optimized case. Note that in this figure, the curve stops when the assumed ultimate compressive strain 0.003 happens, and the wall is considered as crushed at the end of each curve. The pushover load at the crushed stage can be read from the value in vertical axis. Multiplying the crushed load by the wall height, which is 5 ft, gives the strong axis moment strength of the wall.

Table 4-10. Comparison of Hand Calculation Results and FE Model Results for the Strong Axis Moment Capacity of the Wall

	FE Model Results (kip-ft)	Calculation Results (kip-ft)	Difference
2 – 0.84” dia.	27.61	22.18	20%
14 – 0.84” dia.	26.94	22.18	18%
6 – 1.05” dia.	26.79	22.16	17%
10 – 1.05” dia.	26.89	22.16	18%
8 – 1.315” dia.	26.52	22.14	17%
4 – 1.66” dia.	26.72	22.12	17%
9 – 1.66” dia.	25.88	22.12	15%

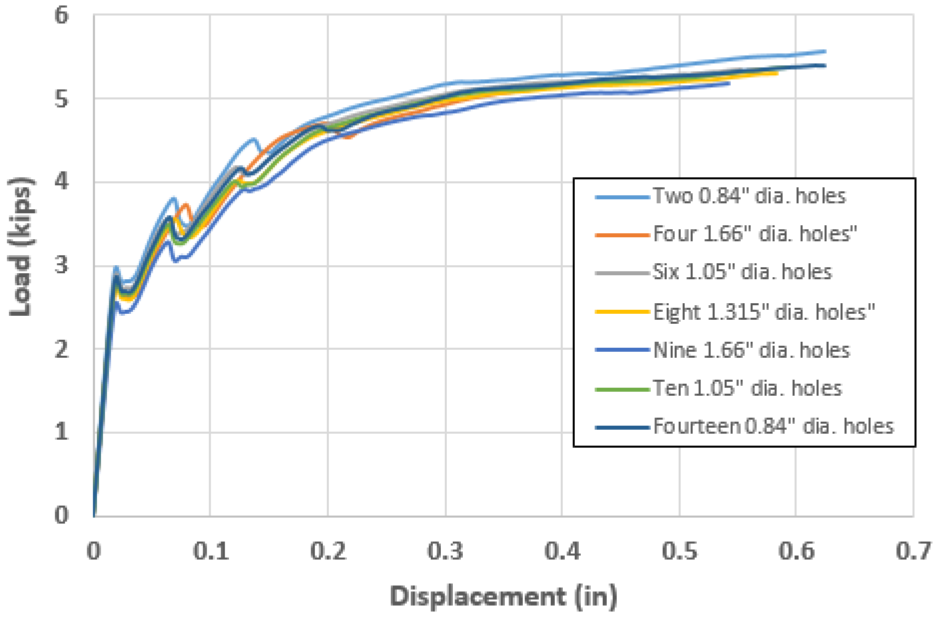

Figure 4-25. Parametric Study of the Strong Axis Moment Capacity of the Wall with Different Opening Configurations

From the table, it can be seen that based on both hand calculation results and the FE model results, the difference between the strong axis moment strengths of the wall with different opening configurations are very small. This is also shown in Figure 4-25, where the crushing load of the wall with different openings are very close to each other. This is different from the shear and axial loading capacities of the wall, where the impact of openings on the wall is relatively greater. This is because the majority of the holes are in the tension zone of the concrete, and these empty areas in the tension zone will not affect the pushover load capacity and the strong axis moment strength of the wall because the concrete will crack anyway under tensile stress, and the reinforcement will take the tensile force instead after crack happens.

The differences between hand calculation results and FE model results are around 15-20% for all the opening configurations. Several reasons could cause this differences. First, the hand calculation is based on the cross section of the wall, however, in the FE model, the footing with a larger cross section area is included, affecting the moment capacity of the wall, possibly resulting in a higher moment strength. Second, the defined material properties, such as the dilation angle of concrete and concrete modulus of elasticity, could also affect the results from the FE model. Furthermore, in both the FE model and hand calculations, the steel yield stress is used as 60 ksi. After the steel yields, it is assumed that the steel stress will remain constant in hand calculations. However, the actual steel stress might be higher than 60 ksi after it yields in the FE model, resulting in a higher moment capacity of the wall.

CHAPTER 5. DESIGN METHOD FOR WALL WITH CIRCULAR OPENINGS

The study of the strengths of the wall in this thesis are based on the ACI 318-14 Building Code. The building code provides a method for calculating the strengths of solid walls; this study aims to extend from these methods to develop the equations for calculating the strengths of walls with circular openings as well as to find the factor in front of the extended equations to obtain more accurate results. Table 5-1 summarizes the equations from the ACI 318-14 Building Code to calculate the moment of inertia and the shear, moment and bearing capacity of a wall. The extended methods to calculate the wall strengths with circular openings that were mentioned previously in chapter 2.3 are also included.

Table 5-1. Comparison of Equation for Calculating the Strengths of Solid Wall from ACI 318-14 Building Code and Wall with Circular Openings from Improved Method from this Study

(a)

	Moment of Inertia
ACI 318-14 **Building Code**	$I_y = \frac{1}{12} bh^3$ where b and h are the width and thickness of the wall
Extended Method	$I_y = \frac{1}{12} bh^3 - \sum_{i=1}^{n} A\overline{y_i}^2 - n\frac{1}{4}\pi r^4$ where A is the area of each hole, $\overline{y_i}$ are the distances from center of each hole to the neutral axis, n is the number of holes, and r is the radius of each hole.

Table 5-1. (continued)

(b)

	Shear Strength
ACI 318-14 **Building Code**	$V_n = V_c + V_s$ where $V_C = 2\sqrt{f'c}b_wd$ is the shear strength from concrete $V_S = \frac{A_v f_{yt} d}{S}$ is the shear strength from shear reinforcements
Extended Method	$V_n = V_c + V_s$ where $V_C = 2\sqrt{f'c}(b_wd - A')$ is the shear strength from concrete $V_S = \frac{A_v f_{yt} d}{S}$ is the shear strength from shear reinforcements if the openings does not affect the shear reinforcements

Table 5-1. (continued)

(c)

	Moment Strength
ACI 318-14 **Building Code**	$M_n = A_s f_y(d - \frac{a}{2})$ for singly reinforced concrete structures $M_n = C_C\left(d - \frac{a}{2}\right) + C_S(d - d')$ for doubly reinforced concrete structures
Extended Method	$M_n = A_s f_y(d - \frac{a'}{2})$ for singly reinforced concrete structures $M_n = C'_C\left(d - \frac{a'}{2}\right) + C'_S(d - d')$ for doubly reinforced concrete structures where a’ is the increased depth of compressive stress block when considering area reduction from the openings that inside the compressive stress block; C'_s is the new force in the compression reinforcement that calculated bases on the new depth of compressive stress block

Table 5-1. (continued)

(d)

	Axial Load Strength
ACI 318-14 **Building Code**	$P_n = 0.85f'c(A_g - A_{st}) + f_yA_{st}$
Extended Method	$P_n = 0.85f'c(A_g - A_c - A_{st}) + f_yA_{st}$ where A_c is the total area of the openings on top surface of the wall

The calculated results of the strengths of the solid wall and wall with optimized opening configuration are shown in appendix A, and the results of the strengths of with all possible opening configurations in the study are shown in appendix B. Based on the comparison of hand calculation results and FE model results that shown in chapter 4, it is obvious that the wall strengths that calculated from the extended method is not very accurate especially for the shear strength, where the difference could go beyond 30%. In order to reduce the difference between the calculation results and the FE results and to obtain more accurate results from doing hand calculations, a factor is necessary to be included in front of each equation to generate the improved method for calculating the wall strengths. These factors are defined by using the least squares method.

First is the moment of inertia of the wall. Since the extended method shown in Table 5-1 for calculating the wall with openings are already proofed in ACI 318-14 Building Code, therefore, this method does not need any improvements. The final equation for calculating the moment of inertia of wall with circulating openings can be referred to equation 3 in chapter 2.

Second is the shear strength of the wall. As one can see that the extended method will give more inaccurate results with the increasing hole sizes and number (Table 4-9), it is assumed that the adjustment factor has a relationship with both of these two parameters. By doing multiple trials, the factor is found to be correlated with the total area of the holes in the wall, and can be expressed as:

$$\emptyset = \frac{1}{1+\frac{A}{\alpha}} \tag{18}$$

where $\emptyset$ represents the adjustment factor, and A is total area of the holes. α is the number that obtained from the least squares method. The least squares method takes the minimization of the sum of the squares of the errors made in every single equation into account. In finding the shear factor, there are total 8 opening configurations considered, and the goal is to minimize the sum of the square of all the eight differences between the factored calculation results and the FE model results, which can be expressed below:

$$min\,\sum_{i=1}^{8}(y_i * \frac{1}{1+\frac{A}{\alpha}} - x_i)^2 \tag{19}$$

where x is the FE model results and y is the calculation results. The number α that indicates the minimum sum square value will be selected in the adjustment factor equation. By applying the error function in MATLAB, the number α is found to be 45.173, and thus, the adjustment factor can be expressed as:

$$\emptyset = \frac{1}{1+\frac{A}{45.173}} \tag{20}$$

Plugging this adjustment factor into the extended equation, the improved equation for calculating the shear strength of wall with circulating openings is:

$$V_n = \emptyset\left[2\sqrt{f'_c}(bd - A') + \frac{A_v f_{yt} d}{s}\right] \tag{21}$$

The differences between the FE model results and calculation results by using the improved method are shown in Table 5-2, and the comparison between the original/improved calculation results and the FE model results is shown in Figure 5-1, where case 1-8 are accord with the opening configuration order in Table 5-2. From the table, one can see that the differences between the FE model and calculation results are significantly reduced with the improved method. This is also clearly shown in Figure 5-1, where the improved calculation results are much closer to the FE model results comparing to the original calculation results. Therefore, we concluded that the improved method effectively increase the accuracy of calculating the shear strength of the wall with circular openings.

Table 5-2. Differences of FE Model and Calculation Results for the Shear Strengths of Wall with Different Opening Configurations

	FE Model Results (kips)	Calculation Results (kips)	Difference
2 – 0.84” dia.	19.27	18.55	3.7%
14 – 0.84” dia.	16.49	15.74	4.5%
6 – 1.05” dia.	16.15	16.71	3.5%
10 – 1.05” dia.	15.69	15.39	1.9%
7 – 1.315” dia.	14.82	15.09	1.8%
8 – 1.315” dia.	14.75	14.68	0.5%
4 – 1.66” dia.	13.69	15.39	12.4%
9 – 1.66” dia.	12.99	12.18	6.2%

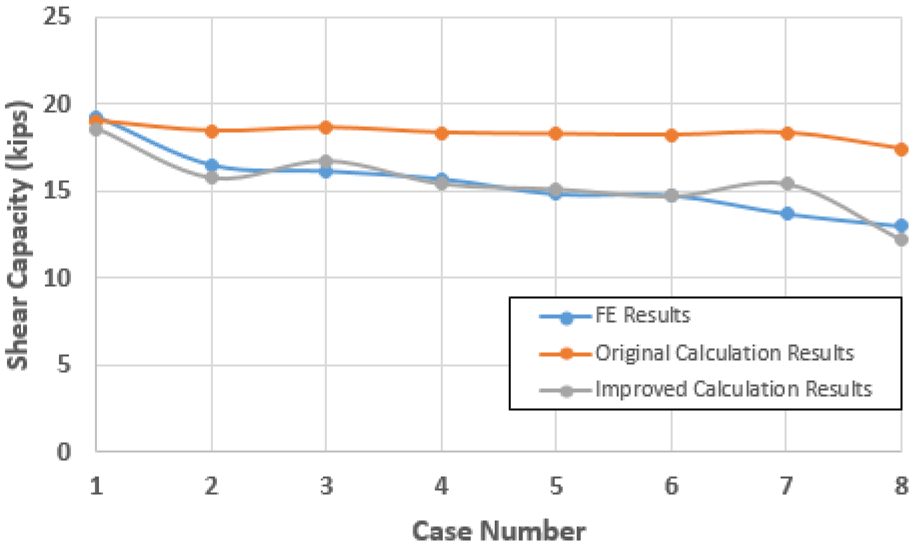

Figure 5-1. Comparison of the Original/Improved Calculation Results and the FE Model Results for the Shear Strengths of the Wall with Different Opening Configurations

The third one is the flexural strength of the wall. Table 4-10 shows that the calculation results have 15 – 20% differences from the FE model results, which means the differences do not have a significant change with respect to different configurations of the holes in the wall. Therefore, the adjustment factor can be assumed as a constant number. Similarly, by using the least squares method, the goal is to minimize the sum of the square value of the differences between the factored calculation results and the FE model results from the selected eight opening configurations, and the equation can be summarized as:

$$min \sum_{i=1}^{8}(x_i - \alpha * y_i)^2 \tag{22}$$

where x is the FE model results and y is the calculation results. By using MATLAB, the number α of 1.21 will give the minimum sum square value, and thus, the adjustment factor can be expressed as:

$$\emptyset = 1.21 \tag{23}$$

Plugging this adjustment factor into the extended equation, the improved equation for calculating the flexural strength of wall with circulating openings is:

$$M_n = \emptyset\left[C'_c\left(d - \frac{a'}{2}\right) + C_s(d - d')\right] \tag{24}$$

The differences between the FE model results and calculation results by using the improved method are shown in Table 5-3, and the comparison between the original/improved calculation results and the FE model results is shown in Figure 5-2. It can be seen that the differences between the FE model and calculation results are reduced to within 5% by using the improved method. This is clearer in looking at the comparison figure in Figure 5-2, where the improved calculation results and FE model results are getting closer to each other. Therefore, the improved method can also provide more accurate results in calculating the flexural strength of the wall with circular openings.

Table 5-3. Differences of FE Model and Calculation Results for the Flexural Strengths of Wall with Different Opening Configurations

	FE Model Results (kip-ft)	Calculation Results (kip-ft)	Difference
2 – 0.84” dia.	27.61	26.84	2.8%
14 – 0.84” dia.	26.94	26.84	0.4%
6 – 1.05” dia.	26.79	26.81	0.1%
10 – 1.05” dia.	26.89	26.81	0.3%
7 – 1.315” dia.	26.74	26.79	0.2%
8 – 1.315” dia.	26.52	26.79	1%
4 – 1.66” dia.	26.72	26.77	0.2%
9 – 1.66” dia.	25.88	26.77	3.4%

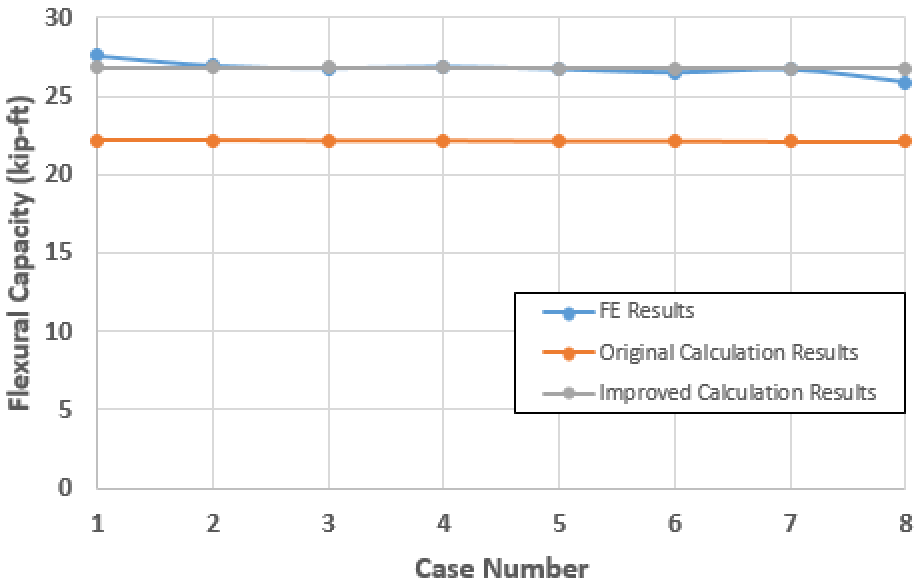

Figure 5-2. Comparison of the Original/Improved Calculation Results and the FE Model Results for the Flexural Strengths of the Wall with Different Opening Configurations

The last one is the axial strength of the wall. As shown in Table 4-8, the calculation results 5–10% differences from the FE model results, which also means the percentages of the differences do not dramatically change with different configurations of the holes in the wall, and the adjustment factor is assumed to be a constant number. Following the same method to minimize the sum of the square value of the eight differences between the factored calculation results and the FE model results as shown in equation 22, the adjustment factor is finally found and is expressed below:

$$\emptyset = 1.07 \tag{25}$$

Plugging this factor in front of the extended equation, the improved equation for calculating the axial strength of wall with circulating openings is:

$$M_n = \emptyset\left[0.85f'_c\left(A_g - A_o - A_{st}\right) + f_y A_{st}\right] \tag{26}$$

With this improved method, the differences between the FE model results and calculation results are shown in Table 5-4, and the comparison between the original/improved calculation results and the FE model results is shown in Figure 5-3. The differences between the FE model and calculation results are effectively reduced to within 3% by using the improved method. Also, by looking at Figure 5-3, the improved calculation results and FE model results are almost overlap with each other. Therefore, the improved method also successfully improved the calculation results in obtaining the axial strength of the wall with circular openings.

Table 5-4. Differences of FE Model and Calculation Results for the Axial Strengths of Wall with Different Opening Configurations

	FE Model Results (kips)	Calculation Results (kips)	Difference
2 – 0.84” dia.	379.91	369	2.9%
14 – 0.84” dia.	350.05	344.81	1.5%
6 – 1.05” dia.	350.84	354.14	0.9%
10 – 1.05” dia.	340.39	341.53	0.3%
7 – 1.315” dia.	333.24	338.12	1.5%
8 – 1.315” dia.	329.43	333.51	1.2%
4 – 1.66” dia.	342.97	341.54	0.4%
9 – 1.66” dia.	301.71	302.18	0.2%

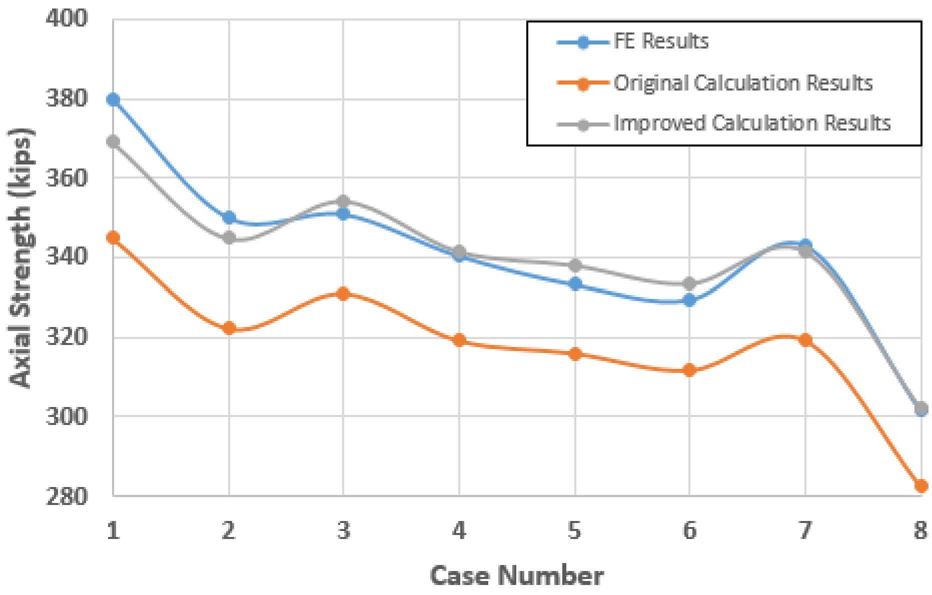

Figure 5-3. Comparison of the Original/Improved Calculation Results and the FE Model Results for the Axial Strengths of the Wall with Different Opening Configurations

In order to explore the influences of the openings to the different strengths of the wall, Table 5-5 summarize the strengths of wall with smallest available area of openings, two 0.84” diameter holes, as compared to the wall with the largest available area of openings, nine 1.66” diameter holes. Note that M_{n1} is the strong axis moment strength and M_{n2} is the weak axis moment strength.

Table 5-5. Comparison of the Strengths of Wall with Available Smallest and Largest Area of Circular Openings

	I_y (in^4)	V_n (kips)	M_{n1} (kip-ft)	M_{n2} (kip-ft)	P_n (kips)
Wall with Two 0.84” Diameter Holes	4478	19.27	27.61	4.68	379.91
Wall with Nine 1.66” Diameter Holes	3723.4	12.99	25.88	4.4	301.71
Strength Reduction	16.9%	32.6%	6.3%	6%	20.6%

By comparing the FE model results between the wall with available smallest and largest area of openings, it can be concluded that the longitudinal openings have relatively small effects to the moment strengths on both strong and weak axis of the wall. This is because the compression block depth is very smaller in both directions with the reinforcement design of the wall, and very small portions of the holes fall in the compression block, and thus the moment strength reduction is limited. However, the openings in the wall will result in somehow reductions for moment of inertia and axial strength, and even more significant reduction for shear strength.

The design method of wall with circular openings is generated based on how much impact the openings will have to the strengths of the wall. Since the moment strength will not be influenced a lot, only a few more flexural reinforcements need to be added in the wall. However, the designer could intentionally increase the amount of shear reinforcements when designing a wall with openings so that the shear strength reduction from the openings could be compensated for. Also, according to the improved equation, a smaller distance from the center of the opening to the neutral axis will lead to less moment of inertia reduction, therefore, the openings can be designed closer to the neutral axis of the wall to decrease the effect from moment of inertia of the wall. For a bearing wall, the axial load strength is the most important aspect that needs to be considered, as walls are always under compressive loading conditions due to gravity loads. The compressive strength of the concrete material composing the wall will be the dominant factor that determines the axial strength of the wall. Therefore, when designing the wall with openings, the designers can choose to design walls made with higher compressive strength concretes to improve axial loading capacity.

In conclusion, in order to design walls with circular openings, it is necessary to keep the locations of the holes closer to the neutral axis. The spacing between the flexural and shear reinforcements can be reduced to enhance the moment and shear capacities of the wall. Also, if necessary, a higher strength concretes can be used to provide the wall with a higher axial loading capacity. If the designers can weigh the increased cost of the improvement in designing the wall with openings and the purpose of these openings, they can decide whether it is worth to have such openings in the wall and to accommodate the strength of the wall, the design method of the wall can then be amended accordingly with respect to different types of walls, and the effects openings in the wall can be minimized.

CHAPTER 6. CONCLUSIONS AND FUTURE WORK

As the number of tall and slender buildings around the world increases, wind and earthquake loads are a significant concern to engineers, causing excessive vibrations to the occupants, and large displacement and base moments that could cause both structural and safety issues. Therefore, the walls inside the tall buildings are needed to mitigate the vibration. This research studied the TLWD case, which is a multi-column liquid damper that was proposed recently by Wu et al. The TLWD system can be installed inside structural walls to reduce vibration of the building. The walls will have circular openings in the longitudinal direction corresponding to the TLWD’s configuration. The objectives of this study were to optimize the TLWD configuration, considering both the strengths of the wall and the damping effect of the TLWD, to investigate the strengths of the wall with different circular opening configurations, and to improve the design method for solid walls from ACI 318-14 Building Code so that the method can be applied to design for walls with circular openings.

As mentioned in chapter 3, the lab tests include four-point bending, axial loading and pushover tests to investigate the moment and axial strengths of the wall with openings, as well as to validate the FE models and the hand calculations. The four-point bending test is finished at this time, and the axial loading and pushover tests will be conducted throughout the summer on the wall specimens and footing mentioned before.

In chapter 4, several FE models are made to detect the shear, moment and axial strengths of the wall with different opening configurations. Results from the FE models were compared to the hand calculations. The shear strength results showed the highest amount of differences. Further improvements can be made to the FE models, modifying material properties and the boundary conditions. After the axial loading and the pushover tests are done, the results from the FE models can be validated. The hand calculation methods can also be compared.

Overall, future work should address more lab testing for walls with different opening configurations to further prove the rationality of the hand calculation methods, as well as to develop the FE models so that the models can make more accurate predictions. Once the method of calculating the strengths of the walls with circular openings are well proved, then designers can be more confident in designing such walls.

REFERENCES

Abaqus/CAE User’s Manual (6.12) – Abaqus Version 6.12. (2012).

Abavisani, I., Rezaifar, O., & Kheyroddin, A. (2017). Alternating Magnetic Field Effect on Fine-aggregate Concrete Compressive Strength. *Construction and Building Materials, 134*(March), 83–90. https://doi.org/10.1016/j.conbuildmat.2016.12.109

American Concrete Institute. *Building Code Requirements for Structural Concrete (ACI 318-14)*. Farmington Hills, MI, USA, 2014.

Athanasopoulou, A. (2010). Shear strength and drift capacity of reinforced concrete and high-performance fiber reinforced concrete low-rise walls subjected to displacement reversals. *ProQuest Dissertations and Theses*, 316.

Caramia, M., & Dell'Olmo, P. (2008). *Multi-objective Management in Freight Logistics*.

Chai, W., & Feng, M. Q. (1997). Vibration Control of Super Tall Buildings Subjected To Wind Loads. *Int J. Non-Lmear Mechanics*, *32*(4), 657–668. https://doi.org/10.1016/S0020-7462(96)00094-7

Chankong, V., & Haimes, Y. Y. (1983). Multiobjective Decision Making: Theory and Methodology. Retrieved from http://store.doverpublications.com/0486462897.html

Chen, S., & Kabeyasawa, T. (2000). Modeling of Reinforced Concrete Shear Wall for Nonlinear Analysis. *12WCEE, Twelfth World Conference on Earthquake Engineering, New Zealand*, (1596), 1–8.

Davalos, J. F., Qiao, P., & Barbero, E. J. (1996). Multiobjective material architecture optimization of pultruded FRP I-beams. *Composite Structures*, *35*(3), 271–281. https://doi.org/10.1016/0263-8223(96)00035-9

Demeter, I., Stoian, V., & Dan, D. (1990). Seismic Retrofit of Cut-out Weakened Precast RC Walls.

Friswell, M. I., & Mottershead, J. E. (1995). *Finite element model updating in structural dynamics*. https://doi.org/10.1007/978-94-015-8508-8

Gebreyohaness, a S., Clifton, G. C., & Butterworth, J. W. (2012). Finite element modeling of non-ductile RC walls. *15th World Conference on Earthquake Engineering (15WCEE), Lisbon, Portugal*, *11*.

Genikomsou, A. S., & Polak, M. A. (2016). Finite-Element Analysis of Reinforced Concrete Slabs with Punching Shear Reinforcement. *Journal of Structural Engineering*, *142*(12), 1–15. https://doi.org/10.1061/(ASCE)ST.1943-541X.0001603.

Hidalgo, P., Jordan, R. M., & Martinez, M. (2002). An analytical model to predict the inelastic seismic behavior of shear-wall, reinforced concrete structures. *Engineering Structures*, *24*(1), 85–98. https://doi.org/10.1016/S0141-0296(01)00061-X

Hsu, L. S., & Hsu, C.-T. T. (1994). Complete stress — strain behaviour of high-strength concrete under compression. *Magazine of Concrete Research*, *46*(169), 301–312. https://doi.org/10.1680/macr.1994.46.169.301

Karasin, A., Günaslan, S. E., & Öncü, M. E. (2014). Models for Confined Concrete Columns With, (January), 55–63.

Kwok, K. C. S., Hitchcock, P. A., & Burton, M. D. (2009). Perception of vibration and occupant comfort in wind-excited tall buildings. *Journal of Wind Engineering and Industrial Aerodynamics*, *97*(7–8), 368–380. https://doi.org/10.1016/j.jweia.2009.05.006

Lefas, I., Kotsovos, M., & Ambraseys, N. (1990). Behavior of reinforced concrete structural walls: strength, deformation characteristics, and failure mechanism. *ACI Structural Journal*, (87), 23–31. Retrieved from http://www.concrete.org/Publications/InternationalConcreteAbstractsPortal.aspx?m=details&i=2911

Lubliner, J., Oliver, J., Oller, S., & Oñate, E. (1989). A plastic-damage model for concrete. *International Journal of Solids and Structures*, *25*(3), 299–326. https://doi.org/10.1016/0020-7683(89)90050-4

Mansur, M. A. (2006). Design of Reinforced Concrete Beams with Web Openings. *Proceedings of the 6th Asia-Pacific Structural Engineering and Construction Conference*, (September), 5–6. https://doi.org/10.14359/720

Mansur, M. A., & Tan, K.-H. (1999). Concrete Beams with Openings Analysis and Design.

Mohammed, B. S., Ean, L. W., & Malek, M. A. (2013). One way RC wall panels with openings strengthened with CFRP. *Construction and Building Materials,* 40, 575–583. https://doi.org/10.1016/j.conbuildmat.2012.11.080

Picardi, R. C. (2018). Special problems of tall buildings (shear walls , stability of columns , effect of thermal gradients , construction problems).

Pillai, S. U., & Parthasarathy, C. V. (1977). Ultimate strength and design of concrete walls. *Building and Environment,* 12(1), 25–29. https://doi.org/10.1016/0360-1323(77)90003-8

Popescu, C., Sas, G., Blanksvärd, T., & Täljsten, B. (2015). Concrete walls weakened by openings as compression members: A review. *Engineering Structures*, 89, 172–190. https://doi.org/10.1016/j.engstruct.2015.02.006

Rist, V. C., & Svensson, S. (2016). Methodology for Preliminary Design of High-rise Buildings.

Sastry, K., Goldberg, D., & Kendall, G. (2005). *Search Methodologies*. *Compute*. https://doi.org/10.1007/978-1-60761-842-3_19

Steffen, F. (n.d.). Wind-Induced Vibrations in High-Rise Buildings.

Tyau, J. (2009). Finite Element Modeling of Reinforced Concrete Using 3-Dimensional Solid Elements.

Wahalathantri, B. L., Chan, T. H. T., & Fawzia, &. (2011). a Material Model for Flexural Crack Simulation in Reinforced Concrete Elements Using Abaqus. *In Proceedings of the First International Conference on Engineering, Designing and Developing the Built Environment for Sustainable Wellbeing*, 260–264. Retrieved from https://eprints.qut.edu.au/41712/1/eddBE2011_260-264_Wahalathantri.pdf

Wight, J. K. (2016). *Reinforced Concrete*.

Wu, H., Cao, L., Chen, A., & Laflamme, S. (2017). A novel tuned liquid wall damper for multi-hazard mitigation. *Proceedings of SPIE - The International Society for Optical Engineering*, *10164*(April 2017). https://doi.org/10.1117/12.2261632

Wu, J. S., & Hsieh, M. (2002). Study on the dynamic characteristic of a U-type tuned liquid damper. *Ocean Engineering*, *29*(6), 689–709. https://doi.org/10.1016/S0029-8018(01)00040-3

Yu, T., Teng, J. G., Wong, Y. L., & Dong, S. L. (2010). Finite element modeling of confined concrete-II: Plastic-damage model. *Engineering Structures*, *32*(3), 680–691. https://doi.org/10.1016/j.engstruct.2009.11.013

Zhang, L., & Yang, Z. (2008). The Finite Element Analysis on Reinforced Concrete Short Pier Shear Wall Structures Combination of rectangle plain-plate finite element The model of reinforced concrete plain-plate finite element, *6*(1), 64–72.

Zhang, X., Qin, Y., & Chen, Z. (2016). Experimental seismic behavior of innovative composite shear walls. *Journal of Constructional Steel Research*, 116, 218–232. https://doi.org/10.1016/j.jcsr.2015.09.015

Zhang, Y.-G., Lu, M.-W., & Hwang, K.-C. (1994). Finite element modeling of reinforced concrete structures. *Finite Elements in Analysis and Design*, *18*(1–3), 51–58. https://doi.org/10.1016/0168-874X(94)90089-2

APPENDIX A. HAND CALCULATIONS OF THE STRENGTHS OF WALL

WALL REINFORCEMENT DESIGN:

The wall with embedded TLWD should be considered as a seismic force-resisting system or wall with high shear force. According to ACI 318-14 chapter 18.10.2.1, the reinforcement ratios for both longitudinal and transverse directions should be at least 0.25%, and reinforcement spacing in each direction should not exceed 18 inches. Additionally, longitudinal reinforcement ratio should be at least $0.0025 + 0.5(2.5 - \frac{h_w}{l_w})(\rho_t - 0.0025)$ from ACI 318-14 chapter 11.6.2. In the equation, h_w is height of the wall, l_w is width of the wall, for NO.2 bar, $A_s = 0.0491$ in^2, $d_b = 0.25$ in.

Transverse reinforcement Requirement: $A_s = \rho_t \times 12'' \times h = 0.0025 \times 12 \times 4 = 0.12\,\frac{in^2}{ft}$

Try 2-layer 8 NO.2 rebar along the height of the wall. With concrete cover of 0.75" at top and bottom, bar spacing is $(60 - 0.75 \times 2 - 0.25)/(8 - 1) = 8.32''$.

Check ρ_t: $\rho_t = (0.0491 \times 12/8.32) \times 2/(12 \times 4) = 0.295\% > 0.25\%$, OK.

Longitudinal Reinforcement Requirement: $A_s = \rho_l \times 12'' \times h = 0.0025 \times 12 \times 4 = 0.12\,\frac{in^2}{ft}$

Try 2-layer 4 NO.2 rebar along the width of the wall. With concrete cover of 0.75" at left and right, bar spacing is $(24 - 0.75 \times 2 - 0.25)/(4 - 1) = 7.42''$.

Check ρ_l: $\rho_l = (0.0491 \times 12/7.42) \times 2/(12 \times 4) = 0.331\% > 0.25\%$, OK.

Also, $0.0025 + 0.5\left(2.5 - \frac{60}{24}\right)(0.00295 - 0.0025) = 0.25\% < 0.331\%$, OK.

Both transverse and lognitudinal reinforcement spacings are smaller than 18", so this meets the spacing requirement.

For the walls with footings, longitudinal NO.2 bars will extended from the walls to the footings, the hook standards of these extended bars at the bottom are referred to ACI 318-14 chapter 25.3.1:

by using 90° hook, for NO.2 bars, minimum inside bend diameter is $6d_b = 6 \times 0.25 = 1.5''$, hook tail straight extension length is $l_{ext} = 12d_b = 12 \times 0.25 = 3''$.

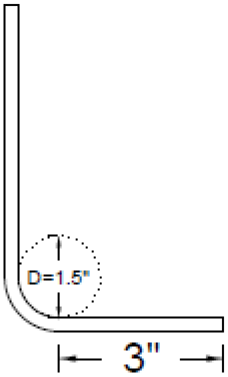

Before soing the optimization, we assume the concrete strength is 4 ksi, therefore, the TLWD system is optimized based on a concrete strength of 4 ksi. In all the calculations of the strengths of the wall panels, 4 ksi is used as f’$_c$, in the lab testing, the real concrete strength may not be 4 ksi, and concrete strength input under material properties in ABAQUS will be revised to the real strength value of the test specimens.

WALL STRENGTHS:

Moment of Inertia:

Moment of inertia in vertical direction of wall:

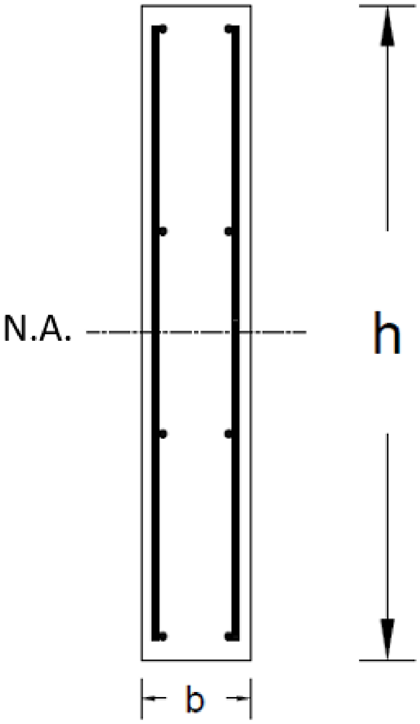

For solid wall case, $I_y = \frac{1}{12}bh^3 = \frac{1}{12} \times 4 \times 24^3 = 4608\ in^4$

Example of the calculation of wall’s moment of inertia in vertical direction with circular openings corresponding to optimized TLWD case:

7 – 1.315” diameter holes:

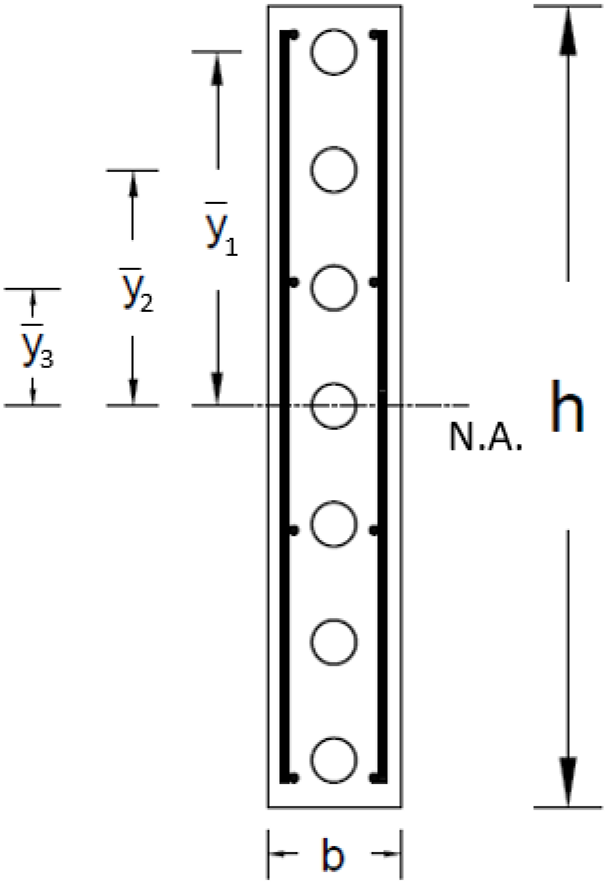

$$A = \frac{1}{4}\pi R^2 = \frac{1}{4}\pi \times 1.315^2 = 1.358\ in^2$$

$$I_y = \frac{1}{12}bh^3 - A\overline{y_1} \times 2 - A\overline{y_2} \times 2 - A\overline{y_3} \times 2 - \frac{1}{4}\pi r^4 \times 7$$

$$= 4608 - 1.358 \times 10.5925^2 \times 2 - 1.358 \times 7.0617^2 \times 2 - 1.358 \times 3.5308^2 \times 2 - \frac{1}{4} \times 0.6575^4 \times 7$$

$$= 4132.9\ in^4$$

__In-plane Shear Capacity:__

For solid wall case:

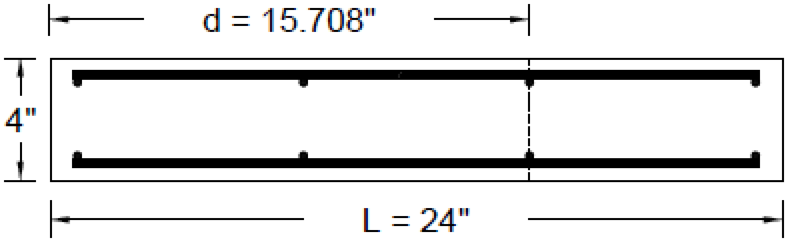

Shear strength from concrete: $V_c = 2\sqrt{f'_c} b_w d = 2\sqrt{4000} \times 4 \times 15.708 = 7.948\ k$

Shear strength from shear reinforcements:

$$V_s = \frac{A_v f_{yt} d}{S} = \frac{0.0491 \times 2 \times 60 \times 15.708}{8.32} = 11.124\ k$$

$$V_n = V_c + V_s = 7.948 + 11.124 = 19.072\ k$$

$$\emptyset V_n = 0.75 \times 19.072 = 14.304\ k$$

Example of the calculation of wall's in-plane shear capacity with circular openings corresponding to optimized TLWD case:

7 – 1.315" diameter holes:

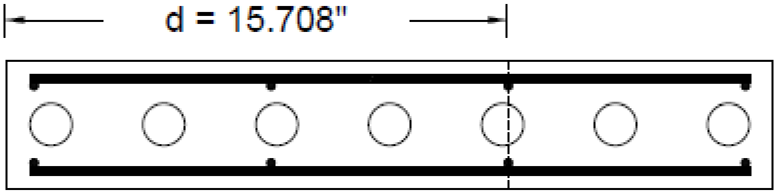

The shear crack is assumed to be go through the holes in the effective depth region, so the shear resistance from concrete is reduced to $2\sqrt{f'_c}(b_w d - A')$ where A' is the top surface area of the holes within the effective region. Since the holes do not affect the shear reinforcements, so the shear resistance from the reinforcements remain the same as the solid case.

$$V_s = \frac{A_v f_{yt} d}{S} = \frac{0.0491 \times 2 \times 60 \times 15.708}{8.32} = 11.124\ k$$

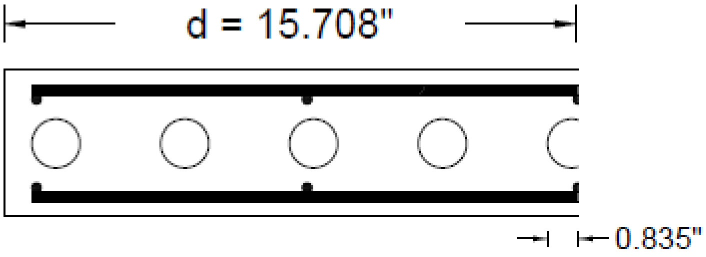

From the figure above, it can be seen that part of the fifth hole falls in the effective depth range.

Horizontal length of the fifth falls in the effective depth region:

$$15.708 - \frac{24 - 0.75 \times 2 - 1.315}{6} \times 4 = 0.835"$$

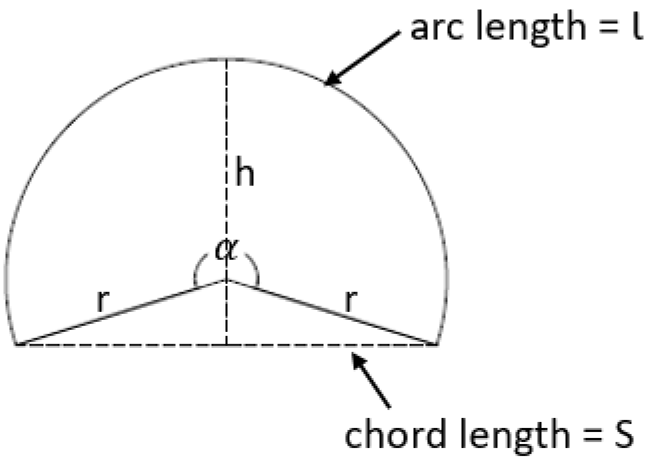

$h = 0.835$, r=0.6575

$$\alpha = 2arc\cos\left(1 - \frac{h}{r}\right) = 2arc\cos\left(1 - \frac{0.835}{0.6575}\right) = 211.324°$$

$$l = r\theta = 0.6575 \times \frac{211.324}{\frac{180}{\pi}} = 2.425"$$

$$S = 2\sqrt{2 \times r \times h - h^2} = 2\sqrt{2 \times 0.6575 \times 0.835 - 0.835^2} = 1.266"$$

$$A_C = r \times \frac{l}{2} - \frac{s(r-h)}{2} = 0.6575 \times \frac{2.425}{2} - 1.266 \times \frac{0.6575 - 0.835}{2} = 0.91\ in^2$$

$$A = 4\pi r^2 + A_C = 4\pi \times 0.6575^2 + 0.91 = 6.343\ in^2$$

$$V_c = 2\sqrt{f'_c}(b_w d - A') = 2\sqrt{4000}(4 \times 15.708 - 6.343) = 7.145\ k$$

$$V_n = V_c + V_s = 11.124 + 7.145 = 18.269\ k$$

$$\emptyset V_n = 0.75 \times 18.269 = 13.702\ k$$

Strong Moment Capacity:

For solid wall case:

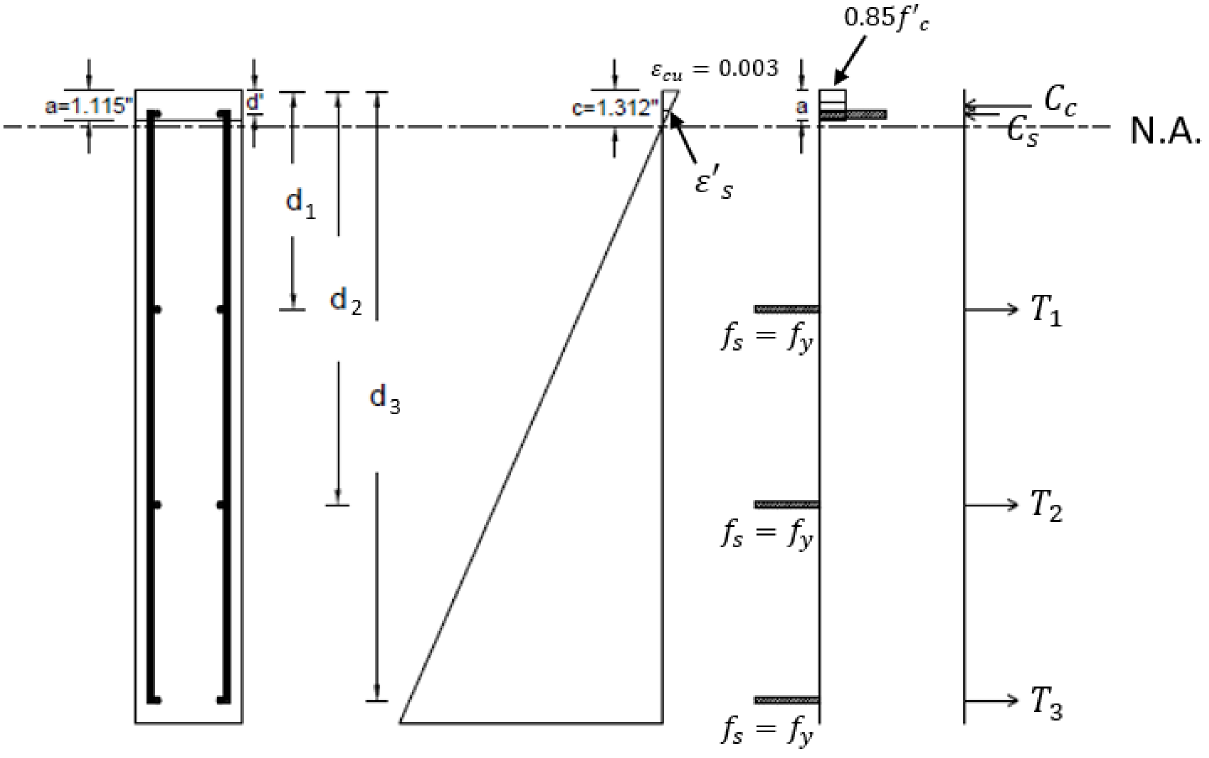

Calculate when $\varepsilon_{cu} = 0.003$ at extreme fiber in compression

$$A_1 f_{s1} + A_2 f_{s2} + A_3 f_{s3} = A'\left(f'_s - 0.85 f'_c\right) + 0.85 f'_c b \beta_1 c$$

$$d_1 = 0.875 + \frac{24 - 0.75 \times 2 - 0.25}{3} = 8.292"$$

$$d_2 = 0.875 + \frac{24 - 0.75 \times 2 - 0.25}{3} \times 2 = 15.708"$$

$$d_3 = 0.875 + \frac{24 - 0.75 \times 2 - 0.25}{3} \times 3 = 23.125"$$

$$0.0491 \times 2 \times \left(0.003 \times \frac{8.292 - c}{c} \times 29000\right) + 0.0491 \times \left(0.003 \times \frac{15.708 - c}{c} \times 29000\right)$$

$$+ 0.0491 \times 2 \times \left(0.003 \times \frac{23.125 - c}{c} \times 29000\right)$$

$$= 0.0491 \times 2 \times \left(0.003 \times \frac{c - 0.875}{c} \times 29000 - 0.85 \times 4\right) + 0.85 \times 4 \times 4$$

$$\times 0.85c$$

Solve for c = 4.7”

Check if steel yields:

1st layer steel stress: $\sigma_1 = 0.003 \times \frac{8.292 - 4.7}{4.7} \times 29000 = 66.49\ ksi > \ f_y = 60\ ksi$, so first layer steel yields. $\sigma_2\ and\ \sigma_3$ will be greater than σ_1, so tension steel in all layers yield when compressive concrete strain at extreme fiber reaches 0.003. Thus, $f_{s1} = f_{s2} = f_{s3} = 60$ ksi.

$$A_1 \times 60 + A_2 \times 60 + A_3 \times 60 = A'(f'_s - 0.85f'_c) + 0.85f'_c b\beta_1 c$$

$$0.0982 \times 60 \times 3 = 0.0982 \times \left(0.003 \times \frac{c - 0.875}{c} \times 29000 - 3.4\right) + 0.85 \times 4 \times 4 \times 0.85c$$

Solve for c = 1.312”

$$a = \beta_1 c = 0.85 \times 1.312 = 1.115"$$

Compression reinforcement:

$\varepsilon'_s = \frac{c - d'}{c}\varepsilon_{cu} = \frac{1.312 - 0.875}{1.312} \times 0.003 = 0.001 < 0.002$, Not yield, OK

$$C_c = 0.85f'_c b\beta_1 c = 0.85 \times 4 \times 4 \times 0.85 \times 1.312 = 15.167\ k$$

$$M_n = C_c\left(d_3 - \frac{a}{2}\right) + C_s(d_3 - d') - T_1(d_3 - d_1) - T_2(d_3 - d_2)$$

$$= 15.167 \times \left(23.125 - \frac{1.115}{2}\right) + 0.0982 \times \left(0.003 \times \frac{1.312 - 0.875}{1.312} \times 29000 - 3.4\right) \times (23.125 - 0.875) - 0.0982 \times 60 \times (23.125 - 8.292) - 0.0982 \times 60 \times (23.125 - 15.708)$$

$$= 267.071\ k * in$$

$$= 22.256\ k * ft$$

$$\emptyset M_n = 0.9 \times 22.256 = 20.03\ k * ft$$

Example of calculation of the wall's strong axis moment capacity with circular openings corresponding to optimized TLWD case:

7 – 1.315" diameter holes:

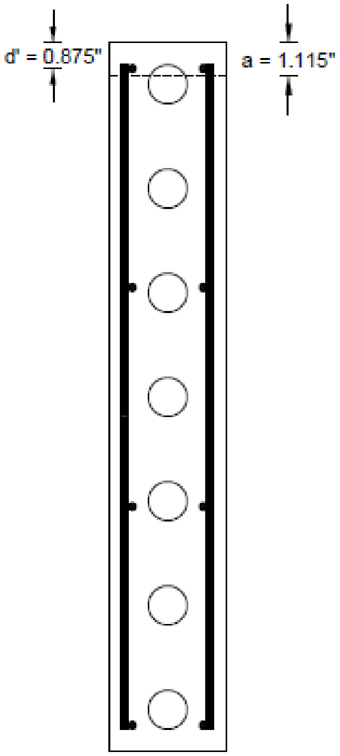

Original compression block area: $1.115 \times 4 = 4.46\ \text{in}^2$, when partial of the hole falls inside the compression block:

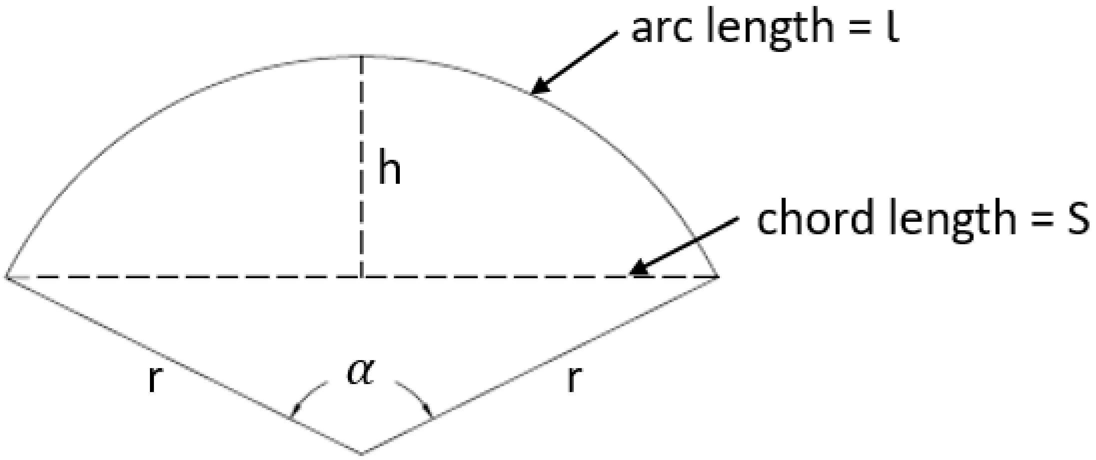

$h = 1.115 - 0.75 = 0.365$, r=0.6575

$$\alpha = 2 \times arc\cos\left(1 - \frac{h}{r}\right) = 2 \times arc\cos\left(1 - \frac{0.365}{0.6575}\right) = 127.17°$$

$$l = r \times \theta = 0.6575 \times \frac{127.17}{\frac{180}{\pi}} = 1.459"$$

$$S = 2\sqrt{2 \times r \times h - h^2} = 2\sqrt{2 \times 0.6575 \times 0.365 - 0.365^2} = 1.178"$$

$$A = r \times \frac{l}{2} - \frac{S(r-h)}{2}$$

$$= 0.6575 \times \frac{1.459}{2} - \frac{1.178(0.6575 - 0.365)}{2}$$

$$= 0.308\ in^2$$

$\frac{0.308}{4} = 0.077"$, 1.115+0.077=1.192"

increase a to 1.192”

now h = 1.192 – 0.75 = 0.442”

following the same method, the area of the circle segment is 0.401 in^2

1.192 x 4 – 0.401 = 4.367 in^2 < 4.46 in^2

increase a to 1.226”

now h = 1.226 – 0.75 = 0.476”

area of compression block is 4.461 in^2 ≈ 4.46 in^2, OK

use a = 1.226”

$$c = \frac{a}{\beta_1} = \frac{1.226}{0.85} = 1.442"$$

$$M_n = T_1 d_1 + T_2 d_2 + T_3 d_3 - C_s * d' - C_c * \frac{a}{2}$$

$$= 0.0982 \times 60 \times (8.292 + 15.708 + 23.125) - 0.0982 \times \left(0.003 \times \frac{1.442-0.875}{1.442} \times 29000 - 3.4\right) \times 0.875 - 0.85 \times 4 \times 4.461 \times \frac{1.226}{2}$$

$$= 265.716\ k * in$$

$$= 22.143\ k * ft$$

$$\emptyset M_n = 0.9 \times 22.143 = 19.929\ k * ft$$

From previous calculation, one can see that no matter how many holes in the wall, it will have the same strong axis moment capacity if the distance from edge of the first hole to edge of concrete and diameters of the first hole remain constant. Therefore, the capacity only need to be calculated one time for one hole size. Following the same method, the depths of compression block and the strong axis moment capacities of the wall with different opening sizes are shown below:

Hole Diameter (in)	**Compression Block Depth (in)**	**Moment Capacity (k*ft)**	**$\emptyset M_n$ (k*ft)**
0.84	1.188	22.179	19.961
1.05	1.205	22.163	19.947
1.315	1.226	22.143	19.929
1.66	1.254	22.117	19.905

Weak Axis Moment Capacity:

For solid wall case:

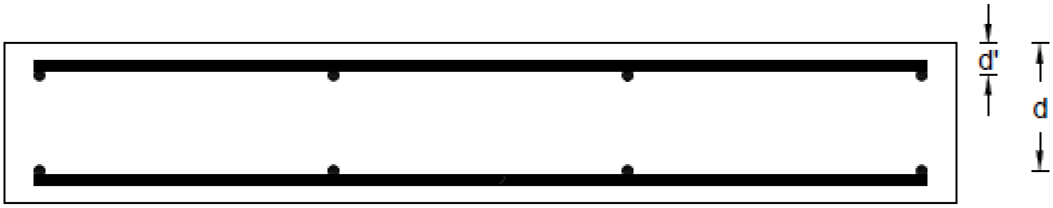

$$f'_c = 5363.67\,psi \;\rightarrow\; \beta_1 = 0.85 - \frac{0.05(5763.67 - 4000)}{1000} = 0.762$$

calculate when $\varepsilon_{cu} = 0.003$ at extreme fiber in compression:

$$A * f_s = A' * \left(f'_s - 0.85f'_c\right) + 0.85f'_c b\beta_1 c$$

$$d' = 0.425 + 0.25 + \frac{0.25}{2} = 0.8''$$

$$d = 4 - 0.425 - 0.25 - \frac{0.25}{2} = 3.2''$$

$$0.0491 \times 4 \times \left(0.003 - \frac{3.2 - c}{c} \times 29000\right)$$

$$= 0.0491 \times 4 \times (0.003 \times \frac{c - 0.8}{c} \times 29000 - 0.85 \times 5.76367 + 0.85$$

$$\times 5.76367 \times 24 \times 0.762 \times c$$

solve for c = 0.708" < d'

therefore, the two layers of flexural reinforcements are all tensile reinforcements

$$a = \beta_1 c = \frac{A_s f_y}{0.85f'_c b} = \frac{0.3928 \times 97.547}{0.85 \times 5.76367 \times 24} = 0.326''$$

$$c = \frac{0.326}{0.762} = 0.428''$$

$$\varepsilon_{s1} = \frac{d - c}{c}\varepsilon_{cu} = \frac{3.2 - 0.428}{0.428} \times 0.003 = 0.0194$$

$f_{s1} = 0.0194 \times 29000 = 563.47\ ksi > 97.547\ ksi$, bottom layer of tensile steel yields

$$\varepsilon_{s2} = \frac{d' - c}{c}\varepsilon_{cu} = \frac{0.8 - 0.428}{0.428} \times 0.003 = 0.00261$$

$f_{s2} = 0.00261 \times 29000 = 75.617\ ksi < 97.547\ ksi$, top layer of tensile steel does not yield

$$M_n = A_{s1}f_y\left(d - \frac{a}{2}\right) + A_{s2}f_{s2}\left(d' - \frac{a}{2}\right)$$

$$= 0.1964 \times 97.547 \times \left(3.2 - \frac{0.326}{2}\right) + 0.1964 \times 75.617 \times \left(0.8 - \frac{0.326}{2}\right)$$

$$= 67.644\ k * in$$

$$= 5.637\ k * ft$$

$$\emptyset M_n = 0.9 \times 5.637 = 5.073\ k * ft$$

Since “a” is smaller than the concrete-reinforcement cover along the thickness direction, which is 0.425”, therefore, the distance from edge of the openings to edge of concrete will be greater than “a” for all the opening configurations. Thus, the openings will not effect the weak axis moment capacity of the wall.

FOOTING DESIGN:

Footing design is based on axial loading case because according to both FE model and hand calculation, bearing capacity of the wall is much higher than the lateral loading capacity of the wall, which means the magnitude of the axial load required to cause the failure of the wall is much greater than the lateral load.

Note: The research object is the wall, so the design of the footing is conservative to avoid any unexpected damage of the footing.

According to FE model and hand calculation, the axial load that causes the failure of the wall with smallest and fewest openings is below 400 kips, a 400-kip load is used in the calculation to obtain conservative design.

$$\frac{400}{\frac{24}{12}} = 200\frac{k}{ft}$$

Self weight of solid wall: $150 \times 5 \times \frac{4}{12} = 0.25\frac{k}{ft}$

Total load: $200 + 0.25 = 200.25\frac{k}{ft}$

No need to consider soil pressure because the footing stands on the ground. Try a 16” thick, 2’ wide footing:

Factor net pressure: $q_{net} = 1.2 \times \frac{200.25}{2} = 120.15\ ksf$

Check for shear:

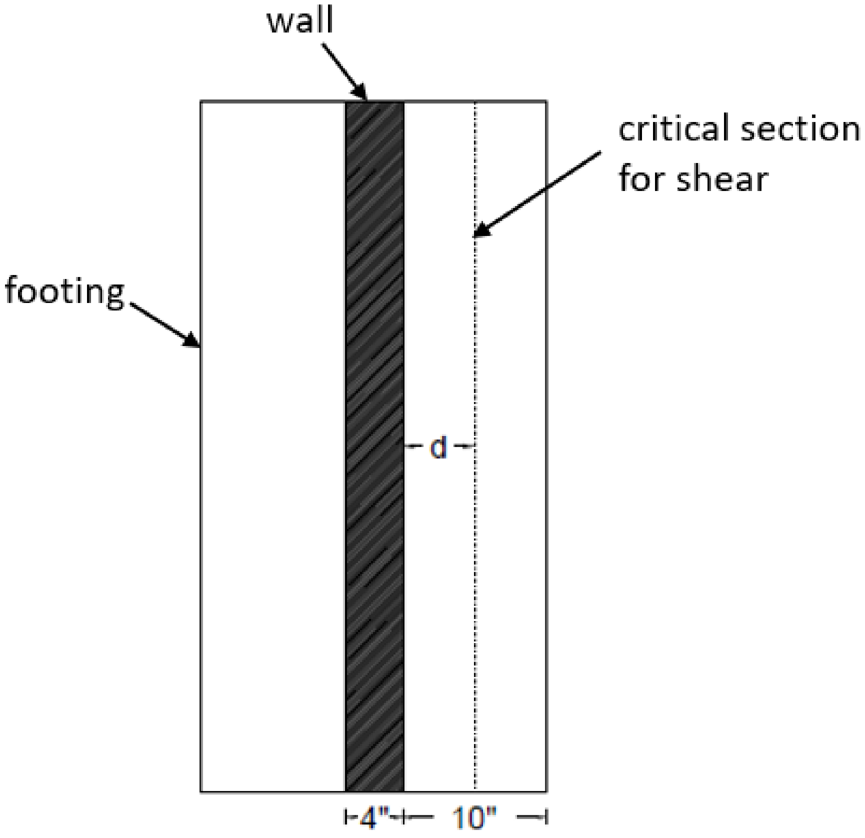

According to ACI Code, the concrete cover is recommended as 1.5” for cast-in-place nonprestressed concrete pedestal. Try NO.6 bars:

$$d = 16 - 1.5 - \frac{1}{2} \times 0.75 = 14.125" > 10"$$

Therefore, there is no critical section for shear.

Design flexural reinforcement:

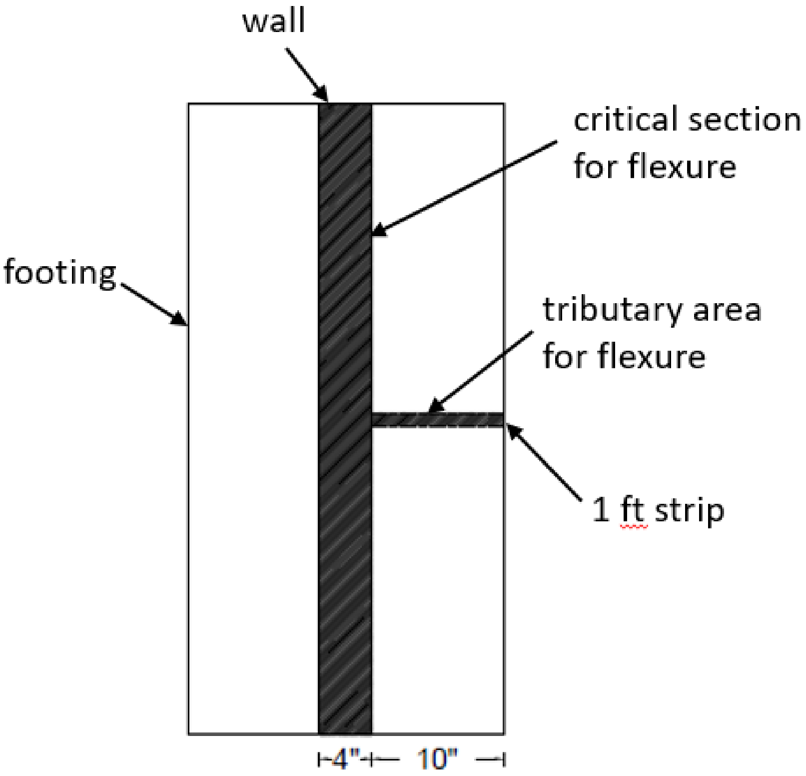

Required moment:

$$M_n = 120.15 \times \frac{(\frac{10}{12})^2}{2} \times 1kip * \frac{ft}{ft} = 41.72\ kips * \frac{ft}{ft}$$

We want:

$$M_u \leq \emptyset M_n = \emptyset A_s f_y jd$$

assume j = 0.95

$$A_s = \frac{41.72 \times 12}{0.9 \times 60 \times (0.95 \times 14.125)} = 0.69 \frac{in^2}{ft}$$

From ACI 318-14 Table 7.6.1.1:

$$A_{s,min} = 0.0018bh = 0.0018 \times 12 \times 16 = 0.346 \frac{in^2}{ft}$$

Therefore, A_s governs

Minimum spacing of bars: 3h or 18”

$3h = 3 \times 12 = 36" > 18"$, so 18” governs

Try 7 # 6 bars:

spacing = $\frac{48-1.5\times 2-0.75}{6} = 7.375"$

$A_s = 0.44 \times 12 \div 7.375 = 0.716\ in^2 > 0.69 in^2$

Because the calculation of A_s was based on an assumed j value, recompute the moment capacity:

$$a = \frac{0.716 \times 60}{0.85 \times 4 \times 12} = 1.05\ in$$

$$\emptyset M_n = 0.9 \times 0.716 \times 60 \times \left(14.125 - \frac{1.05}{2}\right)$$

$$= 43.82\ k * ft > M_u = 41.72\ k * ft, \quad \text{OK}$$

Check ε_t and use it to check Ø:

$$\frac{c}{0.003} = \frac{d_t - c}{\varepsilon_t} \rightarrow \varepsilon_t = \frac{d_t - c}{c} \times 0.003 = \frac{14.125 - \left(\frac{1.05}{0.85}\right)}{\frac{1.05}{0.85}} \times 0.003 = 0.031 > 0.005$$

so $f_s = f_y$, Ø = 0.9

Select minimum temperature reinforcement:

From ACI 318-14 Table 7.6.1.1

$A_s = 0.0018bh = 0.0018 \times 24 \times 16 = 0.69\ in^2$

maximum spacing = min(5h = 5×16 = 80”; 18”) = 18”

so provide 4 # 6 bars to be conservative

$A_s = 4 \times 0.44 = 1.76\ in^2 > 0.69\ in^2$, OK

Final design:

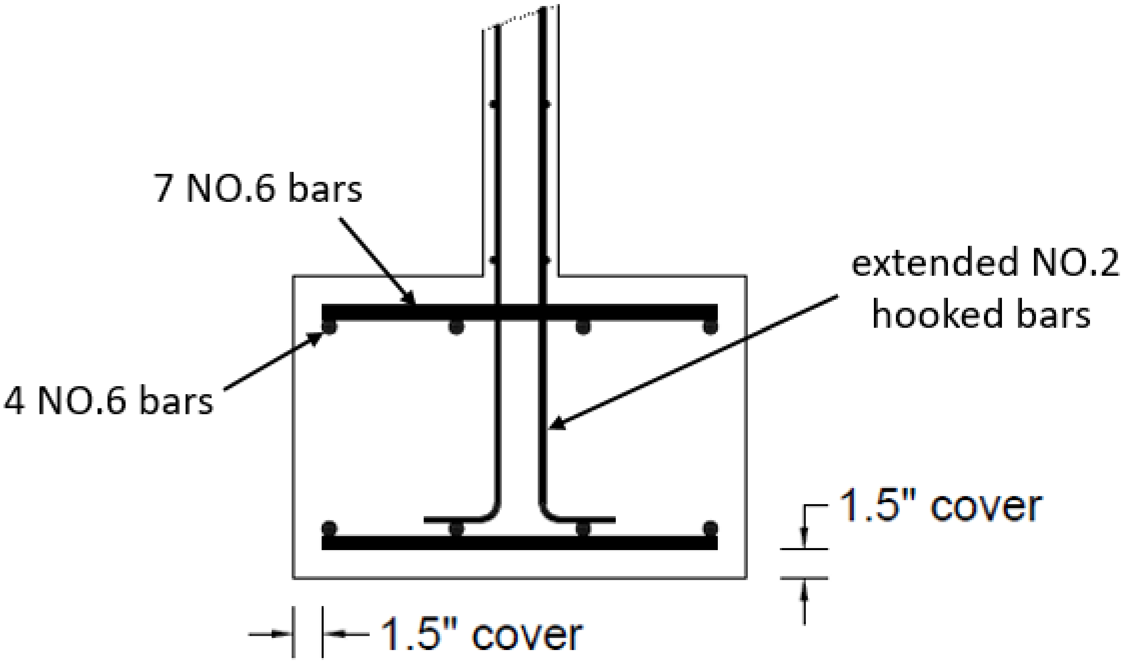

APPENDIX B. RESULTS OF THE OPTIMIZATION OBJECTIVES AND THE CORRESPONDING VECTOR MINIMUM VALUES

Tube Dia. (in)	Tube Number	I_y (in^4)	V_n (kips)	ΦV_n (kips)
0.84	2	4478	19.002	14.251
0.84	3	4477.9	18.931	14.199
0.84	4	4463.5	18.886	14.165
0.84	5	4445.4	18.861	14.146
0.84	6	4425.9	18.791	14.093
0.84	7	4405.6	18.746	14.059
0.84	8	4385	18.721	14.041
0.84	9	4364	18.651	13.988
0.84	10	4342.9	18.606	13.954
0.84	11	4321.7	18.581	13.936
0.84	12	4300.4	18.511	13.883
0.84	13	4279.1	18.466	13.849
0.84	14	4257.7	18.441	13.831
1.05	2	4408.7	18.962	14.222
1.05	3	4408.6	18.853	14.139
1.05	4	4386.4	18.78	14.085
1.05	5	4358.7	18.743	14.057
1.05	6	4328.8	18.634	13.975
1.05	7	4297.7	18.561	13.921
1.05	8	4266	18.524	13.893
1.05	9	4234	18.414	13.811
1.05	10	4201.6	18.342	13.757
1.05	11	4169.1	18.305	13.729
1.05	12	4136.4	18.195	13.647
1.315	2	4302.9	18.9	14.175
1.315	3	4302.8	18.728	14.046
1.315	4	4268.8	18.613	13.96
1.315	5	4226.3	18.556	13.917
1.315	6	4180.4	18.385	13.788
1.315	7	4132.9	18.269	13.702
1.315	8	4084.4	18.213	13.66
1.315	9	4035.2	18.041	13.531
1.315	10	3985.7	17.926	13.444
1.315	11	3935.9	17.86	13.395
1.66	2	4137.3	18.798	14.098
1.66	3	4136.9	18.524	13.893
1.66	4	4084.3	18.339	13.754
1.66	5	4018.7	18.25	13.688
1.66	6	3947.8	17.977	13.482
1.66	7	3874.3	17.791	13.343
1.66	8	3799.4	17.699	13.274
1.66	9	3723.4	17.429	13.072

Tube Dia. (in)	Tube Number	M_n (k*ft)	ΦM_n (k*ft)	Pn (kips)	ΦP_n (kips)
0.84	2	22.179	19.961	344.864	293.134
0.84	3	22.179	19.961	342.98	291.533
0.84	4	22.179	19.961	341.096	289.931
0.84	5	22.179	19.961	339.211	288.33
0.84	6	22.179	19.961	337.327	286.728
0.84	7	22.179	19.961	335.443	285.127
0.84	8	22.179	19.961	333.559	283.525
0.84	9	22.179	19.961	331.675	281.923
0.84	10	22.179	19.961	329.79	280.322
0.84	11	22.179	19.961	327.906	278.72
0.84	12	22.179	19.961	326.022	277.119
0.84	13	22.179	19.961	324.138	275.517
0.84	14	22.179	19.961	322.254	273.916
1.05	2	22.163	19.947	342.744	291.333
1.05	3	22.163	19.947	339.8	288.83
1.05	4	22.163	19.947	336.856	286.328
1.05	5	22.163	19.947	333.912	283.825
1.05	6	22.163	19.947	330.968	281.323
1.05	7	22.163	19.947	328.024	278.82
1.05	8	22.163	19.947	325.08	276.318
1.05	9	22.163	19.947	322.136	273.816
1.05	10	22.163	19.947	319.192	271.313
1.05	11	22.163	19.947	316.248	268.811
1.05	12	22.163	19.947	313.304	266.308
1.315	2	22.143	19.929	339.397	288.488
1.315	3	22.143	19.929	334.78	284.563
1.315	4	22.143	19.929	330.162	280.638
1.315	5	22.143	19.929	325.544	276.713
1.315	6	22.143	19.929	320.927	272.788
1.315	7	22.143	19.929	316.309	268.863
1.315	8	22.143	19.929	311.691	264.938
1.315	9	22.143	19.929	307.074	261.013
1.315	10	22.143	19.929	302.456	257.088
1.315	11	22.143	19.929	297.838	253.163
1.66	2	22.117	19.905	333.916	283.828
1.66	3	22.117	19.905	326.557	277.574
1.66	4	22.117	19.905	319.199	271.319
1.66	5	22.117	19.905	311.84	265.064
1.66	6	22.117	19.905	304.482	258.810
1.66	7	22.117	19.905	297.123	252.555
1.66	8	22.117	19.905	289.765	246.3
1.66	9	22.117	19.905	282.407	240.046

Tube Dia. (in)	Tube Number	Damping Effect	Vector Minimum Value
0.84	2	0.7	0.420217
0.84	3	0.7	0.42026
0.84	4	0.7	0.420383
0.84	5	0.89	0.305924
0.84	6	1.14	0.18318
0.84	7	1.33	0.111186
0.84	8	1.35	0.105155
0.84	9	1.44	0.078838
0.84	10	1.56	0.049945
0.84	11	1.58	0.046575
0.84	12	1.61	0.041689
0.84	13	1.63	0.039107
0.84	14	1.65	0.036781
1.05	2	1	0.247776
1.05	3	1	0.248012
1.05	4	1.06	0.219497
1.05	5	1.05	0.22503
1.05	6	1.27	0.134015
1.05	7	1.55	0.053431
1.05	8	1.62	0.040734
1.05	9	1.66	0.035767
1.05	10	1.68	0.034823
1.05	11	1.7	0.034225
1.05	12	1.8	0.027111
1.315	2	1.04	0.22971
1.315	3	1.04	0.230494
1.315	4	1.1	0.204441
1.315	5	1.31	0.123614
1.315	6	1.49	0.073422
1.315	7	1.77	0.026504
1.315	8	1.79	0.028805
1.315	9	1.82	0.031642
1.315	10	1.95	0.030819
1.315	11	1.99	0.036858
1.66	2	1.13	0.193682
1.66	3	1.13	0.196022
1.66	4	1.2	0.17209
1.66	5	1.64	0.052194
1.66	6	1.83	0.037112
1.66	7	1.88	0.04446
1.66	8	1.97	0.053302
1.66	9	1.98	0.068078
Optimal Design: 7 Tubes with 1.315” Diameter			